UNIVERSITY OF CALIFORNIA
RIVERSIDE

New Precision Measurements of the Casimir Force With Improved Techniques

A Dissertation submitted in partial satisfaction
of the requirements for the degree of

Doctor of Philosophy

in

Physics

by

Mingyue Liu

September 2019

Dissertation Committee:

Dr. Umar Mohideen, Chairperson
Dr. Roya Zandi
Dr. Harry W. K. Tom

Copyright by
Mingyue Liu
2019

The Dissertation of Mingyue Liu is approved:

Committee Chairperson

University of California, Riverside

Acknowledgments

First, I would like to thank Prof. Umar Mohideen. He is an excellent physicist and gave me a lot of support for my research. In my Ph.D. study, I have learned many experimental techniques in his group. These skills I acquired will be very useful in my future career. I could not have finished this dissertation without him. It is my honor to be his student. I also would like to thank the committee members, Prof. Harry W.K. Tom and Prof. Roya Zandi, for their suggestions and discussions.

I would like to thank our group members: Jun Xu, Robert Schafer and Shaolong Chen. They gave me assistance to overcome experiment difficulties. I also thank colleagues Fei Tong, Nicholas Yaraghi, Wei Huang, Prof. Christopher Bardeen and Prof. David Kisailus for collaboration in multidisciplinary research.

I would like to thank all my friends at UC Riverside. Tianbai Li, Liankun Zou, Bowen Yang, Hua Wei, Yunqiu Luo, Tiancong Zhu, Xiang Tong and many other friends.

Finally, I would like to thank my family. I could not have been here without their support and love.

The text of this dissertation (or thesis), in part or in full, is a reprint of the materials as it appears in Physical Review B 100(8): 081406, 2019; Journal of Physics: Condensed Matter 31(7): 075102, 2019 and materials submitted to Modern Physics Letters A and Measurement Science and Technology. The Dr. Umar Mohideen listed in those publications directed and supervised the research which forms the basis for this dissertation. The co-author Jun Xu and Robert Schafer provided technique support, Prof. G. L. Klimchitskaya and Prof. V. M. Mostepanenko helped with theoretical comparison, Rrof.

Roya Zandi provided theoretical suggestions, Nicholas Yaraghi and Prof. David Kisailus provided bio-samples for measurements.

This material is based on the work partially supported by the NSF Grant No. PHY-1607749.

To my parents for all their support.

PUBLICATIONS

[1] M. Liu, J. Xu, G. L. Klimchitskaya, V. M. Mostepanenko and U. Mohideen (2019). ”Examining the Casimir puzzle with an upgraded AFM-based technique and advanced surface cleaning.” Physical Review B (rapid communication) 100(8): 081406.

[2] M. Liu, J. Xu, R. Zandi and U. Mohideen (2019). ”Measurement of entropic force from polymers attached to a pyramidal tip.” Journal of Physics: Condensed Matter 31(7): 075102.

[3] M. Liu, N. Yaraghi, J. Xu, D. Kisailus and U. Mohideen (2019). ”Compact fiber optical interferometer technique to measure picometer displacements in biological piezoelectric materials.” Measurement Science and Technology, submitted. (preprint arXiv:1905.10970.)

[4] M. Liu, R. Schafer, J. Xu, and U. Mohideen (2019). ”Elimination of electrostatic forces in precision Casimir force measurements using UV and Ar ion radiation.” Modern Physics Letters A, submitted.

[5] F. Tong, M. Liu, R. O. Al-Kaysi, and C. J. Bardeen (2018) Langmuir 34 (4), 1627-1634

[6] S. Chen, J. Xu, M. Liu, A. L. N. Rao, R. Zandi, S. S. Gill, and U. Mohideen (2019). ”Investigation of HIV-1 Gag binding with RNAs and Lipids using Atomic Force Microscopy.” (preprint arXiv:1905.10923.)

[7] F. Tong, S. Chen, Z. Li, M. Liu, R. O. Al-Kaysi, U. Mohideen, Y. Yin and C. J. Bardeen (2019), ”Crystal-to-Gel Transformation Stimulated by a Solid-State E→Z Photoisomerization.” Angew. Chem., Accepted.

ABSTRACT OF THE DISSERTATION

New Precision Measurements of the Casimir Force With Improved Techniques

by

Mingyue Liu

Doctor of Philosophy, Graduate Program in Physics
University of California, Riverside, September 2019
Dr. Umar Mohideen, Chairperson

The famous Casimir effect was first predicted by Hendrik Casimir in 1948. Two conducting parallel electrically neutral plates placed in vacuum were predicted to have an attractive force in disagreement with classical physics. The Casimir effect is intriguing because the zero-point energy in quantum vacuum is demonstrated by this macroscopic quantum phenomenon. Nowadays, the Casimir effect is still a fascinating research area. We will first discuss the physical foundation of the Casimir effect from the perspective of quantum field theory and the Lifshitz theory for real materials.

In this dissertation, three experimental projects are presented. Current Casimir effect theories with real materials boundaries treat zero-point photon and real photon scattering similarly based on the fluctuation dissipation theorem. Previous experiments below 1 micrometer separation have shown that dissipation has to be ignored for zero-point photon scattering from free electrons in the material. To understand this puzzle, we developed a higher sensitivity frequency shift technique to perform Casimir force measurement in ultra-high vacuum. Using UV radiation and Ar ions bombardment, we eliminated the role of detrimental electrostatic forces to remove ambiguity in the measurements. The cantilever was treated with a special procedure to reduce its spring constant leading to a sixfold improvement in sensitivity. The Casimir force gradient was measured to the largest separation distance of 950 nm. The data agree with theory if the dissipation from free electron scattering is neglected. This was confirmed to a separation of 820 nm at 67 % CL. Previous work had only shown it for a separation of 420 nm. To study the Casimir force to even larger separation, a difference force measurement experiment has been designed to further improve the force sensitivity. The difference in force between Au surface and a vacuum trench is measured. An air bearing spindle is used and measurement systems have been developed. In related work, the entropic Casimir force originating from thermal fluctuation of polymers in solution confined between a pyramidal tip and a flat plate was experimental studied using the AFM. The results have been analyzed and compared to two theoretical models.

Contents

---

[1] This chapter contains materials published in (1) M. Liu, J. Xu, G. L. Klimchitskaya, V. M. Mostepanenko and U. Mohideen (2019). "Examining the Casimir puzzle with an upgraded AFM-based technique and advanced surface cleaning." Physical Review B 100(8): 081406. and (2) M. Liu, R. Schafer, J. Xu, and U. Mohideen (2019). "Elimination of electrostatic forces in precision Casimir force measurements using UV and Ar ion radiation." Modern Physics Letters A, submitted.

---

[2] This chapter contains materials published in: M. Liu, N. Yaraghi, J. Xu, D. Kisailus and U. Mohideen (2019). "Compact fiber optical interferometer technique to measure picometer displacements in biological piezoelectric materials." Measurement Science and Technology, submitted. (preprint arXiv:1905.10970.)

[3] This chapter contains materials published in: M. Liu, J. Xu, R. Zandi and U. Mohideen (2019). "Measurement of entropic force from polymers attached to a pyramidal tip." Journal of Physics: Condensed Matter 31(7): 075102.

List of Figures

List of Tables

Chapter 1

Introduction of Casimir effect

In recent years, the Casimir effect has become a fascinating research area. The attractive Casimir force between two macroscopic bodies in vacuum was proposed theoretically in 1948 [1], and then confirmed experimentally. On one hand, the observable Casimir force helps to understand the quantum nature of vacuum, interactions in condensed matter systems and set improved constraints on exotic forces beyond standard model. On the other hand, the Casimir force causes detrimental stiction in micro-devices in the field of MEMS. Both the significance in fundamental physics and application in technology motivate researchers to study the properties of the force [2, 3]. In the first chapter, we will discuss how the Casimir force originated from quantum fluctuation in vacuum and mathematically demonstrate a simple model for an ideal case as preparation for more complicated theories. In addition, a brief history of Casimir force measurements is given.

1.1 The physical foundation of Casimir effect

The Casimir effect was first predicted by Dutch physicist Hendrik Casimir in 1948. The typical configuration is that of two neutral conducting plates are placed in parallel in vacuum. An attractive force exists between the two plates. In classical physics, there is no electromagnetic interactions between them because they are uncharged. However, from the point of view of quantum field theory, the virtual zero-point photons created from vacuum interacting with the plates lead to an attractive force. Graphically, the wavelengths of electromagnetic waves of virtual photons between the two plates are limited by the separation. The low frequency modes become dominant as the separation increases. Due to the modification to the allowed wave modes, the density of vacuum energy inside parallel plates is decreased compared to free space. Two plates are brought together shown as in Fig. 1.1. The force even exists at absolute zero temperature because of the quantum nature of zero-point virtual photons. The experimentally verified Casimir force is a direct demonstration of zero-point energy of vacuum.

The Casimir effect was discovered through generalization of the van der Waals force [2, 3, 4]. In 1930, the interactions between non-polar molecules were understood by Fritz London's calculation using quantum mechanics. London's theory assumes an instantaneous electromagnetic interaction between induced dipoles of non-polar molecules. The interaction potential changes as the sixth power of the separation. The later experiments by Evert Verwey and Theodoor Overbeek showed the interaction energy between colloid particles decreased faster than the power of six at large separation. H. B. G. Casimir and D. Polder considered retarded interaction where propagation is limited by the finite speed

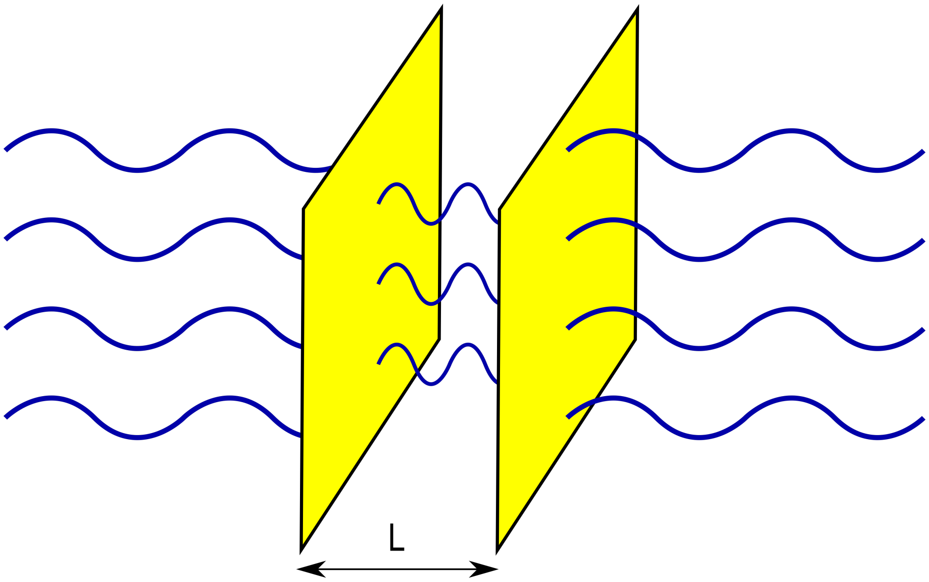

Figure 1.1: Casimir effect: An attractive force acting on two parallel plates in vacuum arises from quantum fluctuation of zero-point photons.

of light. They calculated the particle-wall interaction and particle-particle interaction and explained the faster decrease as r^{-7} at large separation for a two particles system. Inspired by Niels Bohr's suggestion, Casimir developed an improved formalism to calculate interaction between two perfect conducting plates in a two pages paper. The new method assigned half-quanta energy ($\hbar\omega/2$) of vacuum state to every zero-point oscillation in the cavity. Summing over all possible wave modes gives the zero-point energy contribution. The difference in energy between inside cavity and outside space is a finite value. The gradient of zero-point energy suggests the existence of a physically observable attractive force.

The nature of vacuum energy can be simply interpreted by Heisenberg's energy-time uncertainty principle in quantum mechanics.

$$\Delta E \cdot \Delta t \geq \frac{\hbar}{2} \tag{1.1}$$

where ΔE is the uncertainty in the energy and Δt is the uncertainty in time of measurement. This relation implies that a quantum system cannot have a definite energy during a short existence time. The energy density of vacuum background cannot be considered as zero due to the inherent nature of quantum physics. Consider the case of a simple harmonic oscillator in the quantum state, the Hamiltonian operator can be established using creation and annihilation operators:

$$\hat{H} = \frac{\hbar\omega}{2}(a^+a + aa^+) = \hbar\omega(a^+a + \frac{1}{2}) = \hbar\omega(\hat{n} + \frac{1}{2}) \tag{1.2}$$

where ω is the oscillation frequency, $\hat{n}$ is the particle number operator. Number "n" particles occupy quantum state $|n\rangle$. The non-commutative creation and annihilation operators are defined using the following equations:

$$a\,|n\rangle = \sqrt{n}\,|n-1\rangle\,, \quad a^+\,|n\rangle = \sqrt{n+1}\,|n+1\rangle\,, \quad [a, a^+] = 1 \tag{1.3}$$

The expectation value of energy operator under the vacuum state $|0\rangle$ is given by a sum of energies of quantum oscillations over all quantum modes J, which is non-zero:

$$E_0 = \langle 0|\,\hat{H}\,|0\rangle = \frac{\hbar}{2}\sum_J \omega_J \tag{1.4}$$

Because the summation goes over all possible frequencies, the result of the above expression is infinite. But the difference in energy density between the confined space in cavity and outside free space is finite, which is physically measurable. The Casimir pressure is given by taking the derivative of the Casimir energy.

$$P(a) = -\frac{\partial E(a)}{\partial a} = -\frac{\pi^2}{240}\frac{\hbar c}{L^4} \tag{1.5}$$

From the point of view of modern quantum electrodynamics (QED), the zero-point fields exist in the absence of sources. The quantum vacuum can be depicted a sea of appearing and disappearing pairs of virtual particles. Therefore a perfectly empty vacuum in classical concept is actually impossible. Like the Casimir effect, many other experimentally observable phenomena are also proofs of quantum fluctuation. Next, a few quantum effects are introduced by using a physical description rather than a mathematical derivation [4].

One demonstration of the QED vacuum is spontaneous emission. One electron in an atom in an excited state spontaneously decays to a lower energy level by emitting a photon with the difference in energy between the two states. Spontaneous emission is responsible for the process of luminescence. Classical electrodynamics cannot give an answer to the reason behind the emission. The framework of the Schrodinger equation is also incapable of the explanation because its formalism only quantizes energy level but not electromagnetic fields. The transition rate of spontaneous emission is only correctly calculated by considering both QED quantum fluctuation and the effect of radiation reaction. The excited state of an atom is coupled to zero-point oscillations of electromagnetic fields. The vacuum electromagnetic waves induce the atom to make a transition to a lower energy level state. The radiation reaction gives additional contribution to the transition rate [4].

Another case which manifests the quantum vacuum is the Lamb shift. Based on non-relativistic Schrodinger formalism or Dirac formalism without vacuum fluctuation, the states $2S_{1/2}$ or $2P_{1/2}$ should have the same energy level. However, the experiment performed by Willis Lamb and Robert Retherford using Radio-frequency spectroscopy in 1947 found the energy of $2S_{1/2}$ level is about 1Ghz higher than $2P_{1/2}$. The explanation is rooted in quantum electrodynamics using the concept of quantum fluctuation. The emission and re-absorption of the virtual photons by electron are the ultimate cause of the energy split.

The self-interaction of an electron leads to the effective ”smearing charge” of the electron when it moves near the proton of hydrogen atom. In addition, Dirac equation predicted the electron spin g-factor is exactly 2. But the electron-virtual photon interaction gives a rise to an anomalous magnetic dipole moment of the electron. The g-factor is slightly increased due to QED effect, which gives a value of $g = 2.00231930436256(35)$. It was confirmed experimentally with very high precision [4].

Along with many other quantum phenomena, Casimir effect is a manifestation of virtual photons in vacuum and builds a profound concept that vacuum is not empty [4].

1.2 A simple model of Casimir force using a scalar field

In this section, we use a simple method to demonstrate how the Casimir force arises [2, 4, 5]. A scalar field is used to describe zero-point photons, the two polarizations property is treated by considering both positive and negative quantum numbers. The two parallel plates at absolute zero temperature are perfect conductors. No wave penetration needs to be considered. The process of calculation for an ideal case using a scalar field gives a transparent insight to Casimir physics. This ideal case is a preliminary derivation of quantized electromagnetic field confined between perfect metal plates [2].

Starting with 2-dimensional space-time case, a scalar field $\varphi(t, x)$ is defined along x axis in interval $0 < x < L$. It should obey Klein-Gordon equation:

$$\frac{1}{c^2}\frac{\partial^2\varphi(t,x)}{\partial t^2} - \frac{\partial^2\varphi(t,x)}{\partial x^2} + \frac{m^2c^2}{\hbar^2}\varphi(t,x) = 0 \tag{1.6}$$

where the m is the mass of the field. At the boundary, the Dirichlet boundary continuity condition is used:

$$\varphi(t,0) = \varphi(t,L) = 0 \tag{1.7}$$

The orthonormalized solutions along the x axis contains both positive and negative frequencies $\pm\omega_n$.

$$\varphi_n^{(\pm)}(t,x) = (\frac{c}{L\omega_n})^{1/2} e^{\pm i\omega_n t} sin(k_n x) \tag{1.8}$$

$$\omega_n = (\frac{m^2c^4}{\hbar^2} + c^2k_n^2)^{1/2}, \quad k_n = \frac{\pi n}{L}, \quad n = 1, 2, 3, ... \tag{1.9}$$

The quantization of the scalar field is shown here:

$$\varphi(t,x) = \sum_n [\varphi_n^{(+)}(t,x)a_n + \varphi_n^{(-)}(t,x)a_n^+] \tag{1.10}$$

a_n and a_n^+ are annihilation and creation operators. They follow the commutation laws:

$$[a_n, a_{n'}^+] = \delta_{n,n'}, \quad [a_n, a_{n'}] = [a_n^+, a_{n'}^+] = 0 \tag{1.11}$$

The vacuum state is defined by:

$$a_n |0\rangle = 0 \tag{1.12}$$

The 00 component of energy-momentum tensor is the energy density operator. For a scalar field we have:

$$T_{00}^{(0)}(t,x) = \frac{\hbar c}{2}\{\frac{1}{c^2}[\frac{\partial\varphi(t,x)}{\partial t}]^2 + [\frac{\partial\varphi(t,x)}{\partial x}]^2 + \frac{m^2c^2}{\hbar^2}\varphi^2(t,x)\} \tag{1.13}$$

The expectation value of the operator $T_{00}^{(0)}(t,x)$ in the vacuum state $|0\rangle$ is the vacuum energy density, which is infinite.

$$E_0 = \int_0^L \langle 0| T_{00}^{(0)}(t,x) |0\rangle \, dx = \frac{\hbar}{2}\sum_{n=1}^{\infty} \omega_n \tag{1.14}$$

Now the model is extended to 4-dimensional space-time case. We consider two parallel conducting plates spaced by distance L shown as in Fig. 1.1. Two perfectly conducting plates have infinite conductivity at zero absolute temperature. Because EM waves only exist outside of conductors, the boundary condition should obey:

$$\vec{E}_t(t,\vec{r})|_S = \vec{B}_n(t,\vec{r})|_S = 0 \tag{1.15}$$

where $\vec{r}$ is the position vector, "n" and "t" in the subscript denote normal and tangential components respectively. The boundary condition for electromagnetic waves interacting with ideal metals is consistent with Dirichlet boundary condition discussed above. The harmonic oscillator solution can be generalized to 4-dimensional case and applied to two parallel plates. But in directions of x and y, the solutions become continuous. In confined space, we have $\boldsymbol{k} = (k_1, k_2, \pi n/L)$, and the corresponding frequencies are given by:

$$\omega_{k_\perp,n} = c\sqrt{k_\perp^2 + (\frac{\pi n}{L})^2}, \quad k_\perp = (k_x^2 + k_y^2)^{1/2}, \quad n = 0, \pm 1, \pm 2, ... \tag{1.16}$$

Compared to oscillator frequencies of a scalar filed in 2-dimensional space-time, n is expanded to contain negative quantum numbers due to two polarizations of photons, and also set $m = 0$ due to massless photons. The vacuum energy of electromagnetic waves confined between two ideal plates is obtained:

$$E_0(L) = \frac{\hbar}{2}\int_{-\infty}^{\infty}\frac{dk_x}{2\pi}\int_{-\infty}^{\infty}\frac{dk_y}{2\pi}\sum_{n=-\infty}^{\infty}\omega_{k_\perp,n}S \tag{1.17}$$

The above equation can be rewrite into this form:

$$E_0(L) = \frac{\hbar}{2}\int_{0}^{\infty}\frac{k_\perp dk_\perp}{2\pi}(2\sum_{n=0}^{\infty}\omega_{k_\perp,n} - ck_\perp)S \tag{1.18}$$

To perform the regularization for the infinite vacuum energy, we consider the electromagnetic field in free space. The corresponding vacuum energy is obtained using continuous frequencies of free electromagnetic waves.

$$E_{0M}(L) = \hbar a \int_{-\infty}^{\infty} \frac{dk_x}{2\pi} \int_{-\infty}^{\infty} \frac{dk_y}{2\pi} \int_{-\infty}^{\infty} \frac{dk_z}{2\pi} \omega_k S \tag{1.19}$$

$$\omega_k = c\sqrt{k_x^2 + k_y^2 + k_z^2} \tag{1.20}$$

The change of factor 2 is due to two polarizations of photons. We also rearrange the expression as:

$$E_{0M}(L) = \frac{\hbar L}{\pi} \int_0^{\infty} \frac{k_\perp dk_\perp}{2\pi} \int_0^{\infty} dk_z \omega_k S \tag{1.21}$$

A physical way to remove infinity of vacuum energy is provided here. One can subtract vacuum energy of the electromagnetic field confined between the plates from that of a free Minkowski space. The energy density after subtraction is found to be finite:

$$\begin{aligned} E(L) &= \frac{E_0(L)}{S} - \frac{E_{0M}(L)}{S} \\ &= \frac{\pi\hbar c}{L} \int_0^{\infty} \Big(\sum_{n=0}^{\infty} \sqrt{\frac{k_\perp^2 L^2}{\pi^2} + n^2} - \int_0^{\infty} dt \sqrt{\frac{k_\perp^2 L^2}{\pi^2} + t^2} - \frac{Lk_\perp}{2\pi} \Big), \quad t = Lk_z/\pi \end{aligned} \tag{1.22}$$

The calculation uses the Abel-Plana formula. We jump to the final result directly, which is the Casimir energy in the case of electromagnetic waves in vacuum between two ideal conducting plates.

$$E(L) = -\frac{\pi^2}{720} \frac{\hbar c}{L^3} \tag{1.23}$$

The derivative of above equation is the Casimir force in Eq. 1.5.

The theoretical description of Casimir effect for real materials will be demonstrated in the next chapter. The electromagnetic waves penetrate surfaces of real metals within the skin depth due to the finite conductivity. The roughness of metal surfaces needs to be considered. Furthermore, the thermal fluctuation of EM waves also complicates the situation when temperature is non-zero.

1.3 Previous Casimir force measurements

Since Casimir force was theoretically predicted, 70 years have passed. The mysterious Casimir effect attracted a lot of experimental physicists to examine its agreement with theory and study its property. The main experiments are listed below:

In 1958 the first successful measurement of the Casimir Force was performed by M.J. Sparnaay [6]. The attractive force was measured between flat metal plates using a mechanical balance. His measurement was done within range 0.5-5 μm in air. The force sensitivity was 10^{-4} dyne. Due to limitations of the techniques at that time, the systematic errors were about 100% of the measured force. His observation didn't contradict Casimir's theoretical prediction. The obstacles in his measurements pointed out some useful guidelines for later measurements. The roughness of the plates should be reduced. The difference in electric potentials between the two plates needs to be minimized.

In 1968 D. Tabor and R. H. S. Winterton made a direct measurement of surface forces between mica sheets [7]. Their experiment showed the normal van der Waals forces operated for separations less than 10 nm, the retarded van der Waals forces for separations greater than 20 nm. This is a confirmation of the connection between the traditional van der Waals force and the Casimir force.

In 1978 Peter H. G. M. van Blokland and J. Theodoor G. Overbeek showed an unambiguous Casimir force measurement at distances from 132 to 670 nm using Chromium coated surfaces [8]. They improved the spring balance system and took precautions to eliminate electrostatic forces.

In 1997 S. K. Lamoreaux demonstrated the Casimir force in range of 0.6-6 μm using a torsion pendulum [9]. The experiment measured the force between a flat gold plate and a gold-coated spherical lens in vacuum. He reported an agreement with theory at the level of 5%.

In 1998 U. Mohideen and Anushree Roy provided a precision Casimir force measurement [10]. They used an atomic force microscope (AFM) to make precision measurements of the Casimir force from 0.1 to 0.9 μm. An Au coated sphere of diameter 196 μm and a flat plate were used. They considered the finite conductivity, roughness, and temperature corrections. The deviation of 1% between theory and experiment at the closest separation was achieved.

In 2002 G. Bressi, G. Carugno, R. Onofrio, and G. Ruoso measured force gradient in the range of 0.5-3.0 μm using frequency shift technique [11]. The measurement used the Chromium plates and determined the force precision at 15% level.

1.4 An overview of the dissertation

In chapter 2, the Lifshitz theory for real materials will be introduced. We discuss the relationship between the van der Waals force and the Casimir force, and demonstrate the Casimir force for dielectrics at zero temperature and non-zero temperature. For metals, two different models concerning the inclusion the energy dissipation for zero-point photons scattering from conduction electrons are introduced.

In chapter 3, we introduce some improvements that were done for the Casimir force gradient measurements using the frequency shift technique. We used UV light and Ar ion bombardment to clean Au surfaces to largely reduce the detrimental electrostatic effect. A special treatment to the cantilever improved the measurement sensitivity by reducing its spring constant, which allowed extension of our measurement range to distinguish two models discussed in chapter 2.

In Chapter 4, a difference force measurement experiment is introduced. It measures the difference in the Casimir force between Au planar surface and vacuum trench. An air bearing spindle is used in this experiment. It has a potential to achieve much higher sensitivity to measure the Casimir force at larger separation distance.

In chapter 5, an experiment on the entropic Casimir force induced by fluctuating polymers confined between scale free boundaries is introduced. The polymers attached to the apex of a pyramid tip were brought next to a plate. The forces as a function of separation distance was measured. The experimental results were compared with polymer brush model and scale free boundary dependent model.

In the end, the conclusions are made and future experiments are discussed.

Chapter 2

Chapter 2 Lifshitz theory between real materials

In the first chapter, we discussed the zero-point energy of the vacuum state and the Casimir force which results from quantum fluctuations. An ideal Casimir force model was shown for perfectly conductive plates at zero temperature. In this chapter, we discuss the Casimir force for real materials [5]. The Lifshitz formalism provides a path to unify van der Waals force and Casimir force [12]. The calculations using Lifshitz theory for dielectrics at zero temperature and non-zero temperature are introduced. For metals, we present two different theoretical models concerning whether the energy dissipation should be ignored in process of zero-point photons scattering from conduction electrons.

2.1 The relationship between the Casimir force and the van der Waals force

The van der Waals force is a weak and non-directional interaction between atoms, molecules and macroscopic surfaces [13, 14]. Unlike the ionic bond, metallic bond or co-valent bond, it does not contain any strong chemical electronic bond. The van der Waals force theory of interacting atom and molecules was first investigated by German-American physicist Fritz London (1935) [15, 16, 17]. For nonpolar atoms and molecules without permanent multipoles, the random electromagnetic fields induce instantaneous dipole moments. The fluctuations of instantaneous electric fields created by one atom or molecule induces redistribution of electrons in others in the surrounding environment. This intermolecular interaction between multipoles with instantaneously induced fluctuating EM fields is called the London dispersion force.

When we refer to van der Waals forces, the London dispersion force describing induced dipoles of nonpolar atoms or molecules is always included. The following forces are also part of van der Waals force: Debye force that arises from a permanent dipole and an induced dipole; Keesom force to describe electrostatic interaction between permanent charges, dipoles and multipoles; Pauli repulsion is dominant at a few nanometers and prevents the collapse of molecules. A typical interaction energy is shown as in Fig. 2.1 (Copyright: Poszwa https://commons.wikimedia.org/wiki/File:Argon_dimer_potential.pdf, ,,Argon dimer potential", https://creativecommons.org/licenses/by-sa/3.0/legalcode.):

The positive energy indicates a repulsion at close distance due to Pauli exclusion

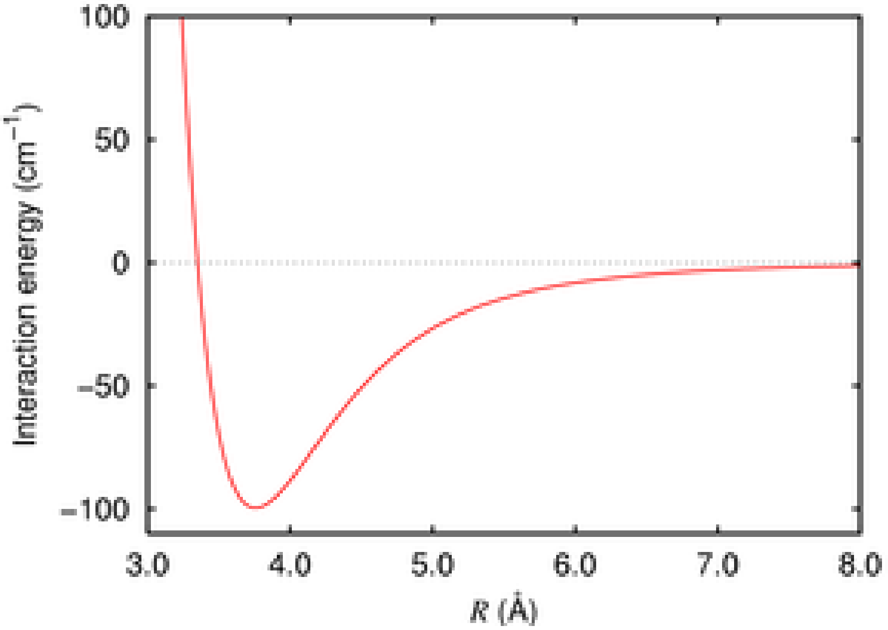

Figure 2.1: Interaction energy between Ar dimers as a function of separation.

principle. The negative part at long distance is the attractive London dispersive force. The total energy can be described using Lennard-Jones potential:

$$V = 4\varepsilon\big[(\frac{\sigma}{r})^{12} - (\frac{\sigma}{r})^{6}\big] \tag{2.1}$$

where ε is the depth of the potential well, σ is the finite distance where the total potential is zero, r is the separation distance between the particles. The first positive r^{-12} term and the second negative r^{-6} term represent Pauli repulsion and London dispersion attraction respectively. The derivative of the potential gives the van der Waals force. The London dispersion force goes as r^{-7} for two particles. In addition, the van der Waals force can be generalized to describe interaction between two surfaces.

The origin of the traditional van der Waals forces is entirely quantum but non-relativistic. The retardation effect between two atoms was first studied by Casimir and Polder, and is called Casimir-Polder force. They considered the relativistic quantum interactions in different cases: interatomic / intermolecular; between an atom / molecule and a surface; between macro-surfaces [18, 19]. Considering the interaction between two surfaces, the non-retarded interaction of the van der Waals force can be generalized to a retarded case. From a microscopic view, the carrier of electromagnetic interaction is the photon. One atom emits a virtual photon from one macroscopic surface. The virtual photon propagates in vacuum medium and reaches the other atom in another object during its lifetime. The correlation of instantaneously induced dipole moments give rise to non-retarded van der Waals force. In fact, the model describing fluctuation of electromagnetic fields can be relativistic if zero-point photons are considered. This retarded case takes place when the virtual photon emitted by the atom cannot reach the other atom during its lifetime if the spacing separation is much larger. The quantized zero-point electromagnetic fields in the vacuum correlate two spatial points where the atoms are situated. This leads to a retarded interaction where its propagation is limited by the speed of light c. The formalism of retarded force includes both quantum mechanics ($\hbar$) and special relativity (c). This interaction is referred to as the retarded van der Waals force or Casimir force [5]. Essentially, the Casimir effect induced by zero-point oscillations of vacuum state is a QED phenomenon, and shares the same origin with the traditional van der Waals force.

The study of retarded force between two points opens a door to unify van der Waals force and Casimir force. The theory for real materials was first given by Lifshitz (1956) [12].

2.2 Casimir force between dielectrics at zero temperature

The Lifshitz theory provides a unified prescription of both the van der Waals force and the Casimir force [20, 5]. It describes the dispersion Casimir force between real planar dielectric materials using optical reflection coefficients in terms of frequency dependent dielectric permittivity. Generally, all the materials can be classified into two groups: dielectrics and metals. The dielectrics have zero conductivity when temperature $T = 0$. For case of $T \neq 0$, dielectrics present non-zero conductivity (extremely small for insulators). In contrast, metals have non-zero conductivity even at $T = 0$ because of free electrons [5]. In this section, we discuss Casimir force between dielectrics at zero temperature. The Lifishitzs theory considers solution of electromagnetic waves in presence of boundary to determine the eigenfrequencies of photons confined between semi-spaces, and then calculates the Casimir energy by integration over all allowed frequencies. Regularization needs to be done to remove divergences. The Casimir pressure is obtained from gradient of the energy [5].

We consider the configuration shown as the Fig. 2.2. Two identical dielectric materials in thermal equilibrium are separated in parallel by vacuum. The gap size is L. The boundary planes are infinitely large and located at $Z = \pm L/2$. We use subscript 1 for the left side dielectric material and 2 for the right side material in the following. In this configuration, the dielectric materials on both sides have the same dielectric permittivity. Therefore, we have:

$$\varepsilon(\omega, \boldsymbol{r}) = \begin{cases} \varepsilon(\omega), |z| \geq L/2, \\ 1, |z| < L/2. \end{cases} \tag{2.2}$$

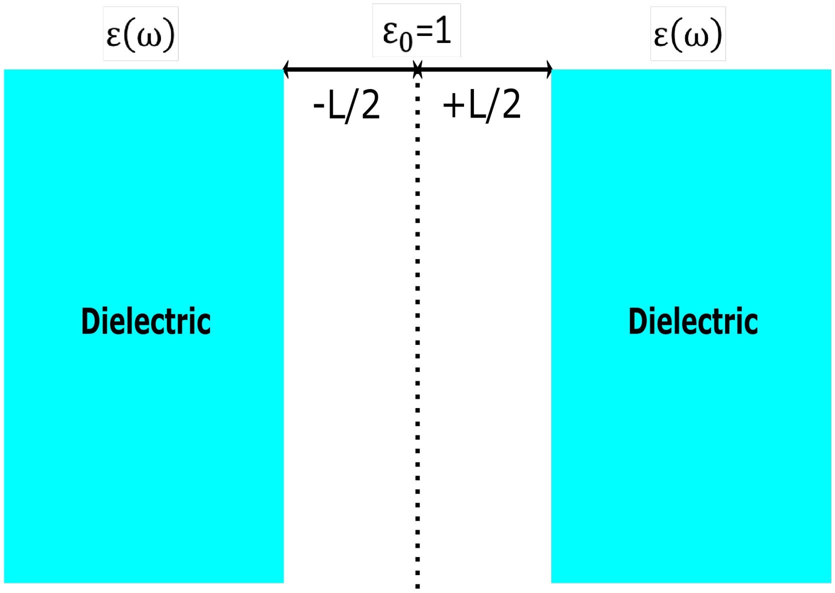

Figure 2.2: The configuration of two dielectric semi-spaces separated by vacuum. The dielectric materials have the same frequency dependent dielectric permittivity. The "z" direction is perpendicular to the boundary plane.

Lifshitz theory assumes random electric and magnetic fields in the dielectrics described by classic electromagnetism. Here, we use the Maxwells equations without charge or current for nonmagnetic materials:

$$\nabla \cdot \boldsymbol{D}(t, \boldsymbol{r}) = 0 \tag{2.3}$$

$$\nabla \times \boldsymbol{E}(t, \boldsymbol{r}) + \frac{1}{c}\frac{\partial \boldsymbol{B}(t, \boldsymbol{r})}{\partial t} = 0 \tag{2.4}$$

$$\nabla \times \boldsymbol{B}(t, \boldsymbol{r}) - \frac{1}{c}\frac{\partial \boldsymbol{D}(t, \boldsymbol{r})}{\partial t} = 0 \tag{2.5}$$

$$\nabla \cdot \boldsymbol{B}(t, \boldsymbol{r}) = 0 \tag{2.6}$$

where $\boldsymbol{D}(t, \boldsymbol{r})$ is the electric displacement, $\boldsymbol{E}(t, \boldsymbol{r})$ is the electric field, $\boldsymbol{B}(t, \boldsymbol{r})$ is the magnetic field. In addition, $\boldsymbol{D}$ and $\boldsymbol{E}$ have the following relations for isotropic dielectrics:

$$\boldsymbol{D}(t, \boldsymbol{r}) = \int_{-\infty}^{t} \varepsilon(t - t', \boldsymbol{r}) \boldsymbol{E}(t', \boldsymbol{r}) dt' \tag{2.7}$$

$$\boldsymbol{D}(\omega, \boldsymbol{r}) = \varepsilon(\omega, \boldsymbol{r}) \boldsymbol{E}(\omega, \boldsymbol{r}) \tag{2.8}$$

The electric and magnetic fields on vacuum-dielectric boundaries should satisfy the continuity conditions:

$$E_{1t}(t, \boldsymbol{r}) = E_{2t}(t, \boldsymbol{r}) \tag{2.9}$$

$$D_{1n}(t, \boldsymbol{r}) = D_{2n}(t, \boldsymbol{r}) \tag{2.10}$$

$$B_{1n}(t, \boldsymbol{r}) = B_{2n}(t, \boldsymbol{r}) \tag{2.11}$$

$$B_{1t}(t, \boldsymbol{r}) = B_{2t}(t, \boldsymbol{r}) \tag{2.12}$$

where the subscripts t and n in above equations refer to tangential component and normal component respectively. Next, we solve the Maxwells equations with appropriate boundary conditions. Consider monochromatic electromagnet fields:

$$\boldsymbol{E}(t, \boldsymbol{r}) = \boldsymbol{E}(\boldsymbol{r}) e^{-i\omega t}, \quad \boldsymbol{B}(t, \boldsymbol{r}) = \boldsymbol{B}(\boldsymbol{r}) e^{-i\omega t} \tag{2.13}$$

Substitute the above expressions into Maxwells equations to obtain the propagation equations inside dielectrics semi-spaces:

$$\nabla^2 \boldsymbol{E}(\boldsymbol{r}) + \varepsilon(\omega) \frac{\omega^2}{c^2} \boldsymbol{E}(\boldsymbol{r}) = 0, \quad \nabla^2 \boldsymbol{B}(\boldsymbol{r}) + \varepsilon(\omega) \frac{\omega^2}{c^2} \boldsymbol{B}(\boldsymbol{r}) = 0 \tag{2.14}$$

In addition, the wave number k and frequency ω of propagating EM waves inside dielectrics follows the relation:

$$k^2 = k_\perp^2 - \varepsilon(\omega) \frac{\omega^2}{c^2} \tag{2.15}$$

where $\boldsymbol{r} = (x, y, z) = (r_\perp, z), k_\perp = (k_x, k_y)$. Following similar procedure, the wave number q of electromagnetic waves in the vacuum gap is given by:

$$q^2 = k_\perp^2 - \frac{\omega^2}{c^2} \tag{2.16}$$

We directly use the energy operator from the second quantization of electromagnetic field here.

$$E = \sum_{\boldsymbol{k}} \sum_{s=1}^{2} \frac{1}{2}\omega(a_{\boldsymbol{k}s}a_{\boldsymbol{k}s}^{+} + a_{\boldsymbol{k}s}^{+}a_{\boldsymbol{k}s}) = \sum_{\boldsymbol{k}} \sum_{s=1}^{2} \omega(N_{\boldsymbol{k}s} + \frac{1}{2}) \tag{2.17}$$

The zero-point energy per unit area of vacuum state at zero temperature is given by:

$$E_0(L) = \frac{\hbar}{2} \sum_{s=1}^{2} \sum_{k} \omega_k = \frac{\hbar}{2} \int_0^\infty \frac{k_\perp dk_\perp}{2\pi} \sum_n (\omega_{k_\perp,n}^{TM} + \omega_{k_\perp,n}^{TE}) \tag{2.18}$$

The summation over frequencies is rewritten as integration over wave numbers. The two polarizations of photon ($s = 1, 2$) correspond to TM (transverse magnetic) and TE (transverse electric) modes in the right hand side of the equation. However, the above result gives an infinite value of vacuum energy density. The finite zero-point energy density should be obtained by subtraction from energy density when spacing L goes to infinity.

$$E(L) = E_0(L) - \lim_{L\to\infty} E_0(L) \tag{2.19}$$

Using all above equations, the calculation is performed on complex plane of ω. We directly give the explicit expression of Casimir energy density obtained by integration along imaginary axis.

$$E(L) = \frac{\hbar}{4\pi^2} \int_0^\infty k_\perp dk_\perp \int_0^\infty d\xi \{ \ln[1 - r_{TM}^2(i\xi, k_\perp)e^{-2Lq}] + \ln[1 - r_{TE}^2(i\xi, k_\perp)e^{-2Lq}] \} \tag{2.20}$$

where variable $\xi = -i\omega$. The reflection coefficients of two different polarizations TE, TM have been used:

$$r_{TM}(i\xi, k_\perp) = \frac{\varepsilon(i\xi)q(i\xi, k_\perp) - k(i\xi, k_\perp)}{\varepsilon(i\xi)q(i\xi, k_\perp) + k(i\xi, k_\perp)}, \quad r_{TE}(i\xi, k_\perp) = \frac{q(i\xi, k_\perp) - k(i\xi, k_\perp)}{q(i\xi, k_\perp) + k(i\xi, k_\perp)} \tag{2.21}$$

Wave number q for EM waves in vacuum gap and wave number k for EM waves in dielectric materials are given by:

$$q^2 = q^2(i\xi, k_\perp) = k_\perp^2 + \frac{\xi^2}{c^2}, \quad k^2 = k^2(i\xi, k_\perp) = k_\perp^2 + \varepsilon(i\xi)\frac{\xi^2}{c^2} \tag{2.22}$$

Note that the Casimir energy can also be expressed in terms of real frequencies. But the representation using imaginary frequencies is more convenient for numerical computation. The Casimir pressure at zero temperature is given by $P = -\partial E_0/\partial L$:

$$P(L) = -\frac{\hbar}{2\pi^2}\int_0^\infty k_\perp dk_\perp \int_0^\infty d\xi q\big\{[r_{TM}^{-2}(i\xi, k_\perp)e^{2Lq} - 1]^{-1} + [r_{TE}^{-2}(i\xi, k_\perp)e^{2Lq} - 1]^{-1}\big\} \tag{2.23}$$

2.3 Casimir force between dielectrics at non-zero temperature

Experimentally, the absolute zero temperature cannot be reached. The discussion and computation for $T > 0$ case are necessary. At non-zero temperature, fluctuation of both zero-point photons and thermal photons contributes to Casimir force [5]. The setup of two semi-places is still the same as described in the above section. The entire system is in thermal equilibrium at temperature T. Following the Matsubara's formalism of thermal quantum field theory, the free energy of a quantum system at non-zero temperature is given by:

$$\mathcal{F} = -k_B T \ln \mathcal{Z} \tag{2.24}$$

where k_B is the Boltzmann constant, and $\mathcal{Z}$ is the Gibbs partition function:

$$\mathcal{Z} = \sum_n e^{-E_n/k_B T} \tag{2.25}$$

where E_n is the energy level at n quantum state.

Here, we directly present the result of electromagnetic Casimir free energy per unit area including both zero-point photons and thermal photons fluctuation without the long derivation.

$$\begin{aligned}\mathcal{F}_0(L,T) = \int_0^\infty \frac{k_\perp dk_\perp}{2\pi} \big\{ \frac{1}{2}\hbar\omega_{k_\perp,0} + k_B T \ln\Big(1 - e^{-\hbar\omega_{k_\perp,0}/k_B T}\Big) + \\ 2\sum_{n=1}^{\infty} \big[\frac{1}{2}\hbar\omega_{k_\perp,n} + k_B T \ln\Big(1 - e^{-\hbar\omega_{k_\perp,n}/k_B T}\Big)\big]\big\}\end{aligned} \tag{2.26}$$

For the $n = 0$ term, there is only one polarization state, and for all n≥1 terms, there are two polarization states because of the nature of photons. The above equation can be reformatted into the below form:

$$\mathcal{F}_0(L,T) = k_B T \int_0^\infty \frac{k_\perp dk_\perp}{2\pi} \big[\ln\big(2sinh\frac{\hbar\omega_{k_\perp,0}}{2k_B T}\big) + 2\sum_{n=1}^{\infty} \ln\big(2sinh\frac{\hbar\omega_{k_\perp,n}}{2k_B T}\big)\big] \tag{2.27}$$

The first term come from $n = 0$ terms in Eq. 2.26 which is independent of separation. Next we only focus on N≥1 terms with physical meaning. The two polarizations corresponds to TE and TM modes with eigenfrequencies of $\omega^{TE}_{k_\perp,n}$ and $\omega^{TM}_{k_\perp,n}$. The Casimir free energy density can be rearranged into this form:

$$\mathcal{F}_0(L,T) = k_B T \int_0^\infty \frac{k_\perp dk_\perp}{2\pi} \sum_{n=1}^{\infty} \big[\ln\big(2sinh\frac{\hbar\omega^{TM}_{k_\perp,n}}{2k_B T}\big) + \ln\big(2sinh\frac{\hbar\omega^{TE}_{k_\perp,n}}{2k_B T}\big)\big] \tag{2.28}$$

The eigenfrequencies of TE and TM modes were obtained using electromagnetism in presence of boundaries in the last section. Note that the above equation is reduced to Eq. 2.18

when T approaches to zero. The result of calculation is directly given as:

$$\mathcal{F}(L,T) = \frac{k_B T}{2\pi} {\sum_{l=0}^{\infty}}' \int_0^{\infty} k_\perp dk_\perp \big\{ \ln[1 - r_{TM}^2(i\xi_l, k_\perp) e^{-2Lq_l}] + \ln[1 - r_{TE}^2(i\xi_l, k_\perp) e^{-2Lq_l}] \big\} \tag{2.29}$$

The prime in the summation represents a 1/2 for $l = 0$ term. The Casimir free energy density is expressed by summing over discrete imaginary frequencies defined as: $\omega_l = i\xi_l$. The Matsubara frequencies ξ_l are fundamental constants in thermal quantum field theory:

$$\xi_l = 2\pi \frac{k_B T}{\hbar} l \tag{2.30}$$

The reflection coefficients at the Matsubara frequencies are:

$$r_{TM}^2(i\xi_l, k_\perp) = \frac{\varepsilon_l q_l - k_l}{\varepsilon_l q_l + k_l}, \quad r_{TE}^2(i\xi_l, k_\perp) = \frac{\varepsilon_l - q_l}{\varepsilon_l + q_l} \tag{2.31}$$

where wave numbers q_l ,$k_\perp$ and frequencies ξ_l have relations:

$$q_l^2 = k_\perp^2 + \frac{\xi_l^2}{c^2}, \quad k_l^2 = k_\perp^2 + \varepsilon_l \frac{\xi_l^2}{c^2}, \quad \varepsilon_l = \varepsilon(i\xi_l) \tag{2.32}$$

Correspondingly, the Casimir pressure at non-zero temperature is obtained by taking the derivative of the Casimir free energy density:

$$P(L,T) = -\frac{k_B T}{\pi} {\sum_{l=0}^{\infty}}' \int_0^{\infty} q_l k_\perp dk_\perp \big\{ [r_{TM}^{-2}(i\xi_l, k_\perp) e^{2Lq_l} - 1]^{-1} + [r_{TE}^{-2}(i\xi_l, k_\perp) e^{2Lq_l} - 1]^{-1} \big\} \tag{2.33}$$

Next, we discuss how to apply Lifshitz theory at non-zero temperature to real dielectric materials. As a central concept of Lifshitz theory, values of dielectric permittivity $\varepsilon(i\xi)$ at all discrete Matsubara frequencies along imaginary axis are needed. The tabulated optical data of dielectric materials provide the complex index of refraction $n(\omega) = n_1(\omega) +$

i$n_2(\omega)$. One can obtain the real and imaginary parts of dielectric permittivity by using real and imaginary part of the optical index of refraction:

$$\mathrm{Re}\varepsilon(\omega) = n_1^2(\omega) - n_2^2(\omega), \quad \mathrm{Im}\varepsilon(\omega) = 2n_1(\omega)n_2(\omega) \tag{2.34}$$

The mathematical Kramers-Kronig relations connect real part and imaginary part of an analytic complex function. We apply the Kramers-Kronig equations to dielectric permittivity, and the following relations are found:

$$\mathrm{Re}\varepsilon(\omega) = 1 + \frac{1}{\pi}P\int_{-\infty}^{\infty}\frac{\mathrm{Im}\varepsilon(\xi)}{\xi-\omega}d\xi, \quad \mathrm{Im}\varepsilon(\omega) = -\frac{1}{\pi}P\int_{-\infty}^{\infty}\frac{\mathrm{Re}\varepsilon(\xi)}{\xi-\omega}d\xi \tag{2.35}$$

where P is the Cauchy principal value. With more calculation, the Kramers-Kronig relation of dielectric permittivity along the imaginary axis is obtained:

$$\varepsilon(i\xi) = 1 + \frac{2}{\pi}\int_{0}^{\infty}\frac{\omega\mathrm{Im}\varepsilon(\xi)}{\xi^2+\omega^2}d\omega \tag{2.36}$$

Considering the above imaginary part $\mathrm{Im}\varepsilon(\xi)$, an analytical form of the dielectric permittivity is given by:

$$\varepsilon(\omega) = 1 + \sum_{j=1}^{K}\frac{g_j}{\omega_j^2 - \omega^2 - i\gamma_j\omega} \tag{2.37}$$

where ω_j is oscillator frequency, g_j is the oscillator strength, and γ is the damping constant and K is the number of oscillators. The K oscillators in the summation describe interactions between photons and core electrons. Therefore, the imaginary part of the above expression is obtained:

$$\mathrm{Im}\varepsilon(\omega) = \sum_{j=1}^{K}\frac{g_j\gamma_j\omega}{(\omega_j^2-\omega^2)^2+\gamma_j^2\omega^2} \tag{2.38}$$

Based on the Kramers-Kronig relation Eq. 2.36, there are two methods to compute dielectric permittivity along the imaginary axis. The first method is to perform numerical integration for Im$\varepsilon(\omega)$ using the tabulated optical data. The second method to calculate the integral is to fit the explicit expression of the imaginary part of $\varepsilon(\omega)$ to the optical data using Eq. 2.38, and then with the fitting parameters obtained the corresponding integration can be performed.

2.4 Casimir force between metals at non-zero temperature

In last section, we discuss the Lifshitz model for dielectrics at zero temperature and non-zero temperature. In this section, we show the theory describing dielectrics can be generalized to metals [5]. The electromagnetic waves penetrate into the surface of real metals within the skin depth. The dielectric response of fluctuating electromagnetic waves to free electrons needs to be described. Because the Casimir effect at non-zero temperature is a more general case, the discussion below is concentrated on metals for $T > 0$.

We use gold as an example. As discussed in the above section, the tabulated data provide values of Im$\varepsilon(\omega)$. Using Kramers-Kronig relation, the dielectric permittivity along the imaginary axis is computable, However, the tabulated optical data is only available for relatively high frequencies ($\omega > 0.125eV$). For lower frequencies, the extrapolation towards zero frequency needs to be performed. Here we demonstrate two models to describe how zero-point electromagnetic waves response to free electrons in metals.

A well-known Drude model is used in the extrapolation to lower frequencies. The Drude dielectric permittivity can be obtained using Maxwells equations by considering the relaxation process of free electrons in metal.

$$\varepsilon_D(\omega) = 1 - \frac{\omega_p^2}{\omega(\omega + i\gamma)} \tag{2.39}$$

where ω_p is characteristic plasma frequency, and $\gamma = \omega_p^2/4\pi\sigma_0$ is the relaxation constant related to dissipation. The σ_0 is the static conductivity of metal. The relaxation constant is related to the energy dispassion when photons interact free electrons. The imaginary part of Drude dielectric permittivity is used for extrapolation in the low frequency range with the plasma frequency $\omega_p = 9.0$ eV and the relaxation parameter $\gamma = 0.035$ eV. The tabulated optical data are used for numerical integration in the high frequency range. Next, the Kramers-Kronig relation is applied to obtain the dielectric permittivity along the imaginary axis. The computed $\varepsilon(i\xi)$ enters into the Lifshitzs formalism to compute Casimir force.

The above discussion using Drude model is based on the configuration that the energy dispassion exists when zero-point photons scatter from conduction electrons in real metal. In other words, the Drude model assume the behavior of virtual photons are the same as real electromagnetic waves in term of dielectric response. However, theoretical study show a violation of the third law of thermodynamics if Drude model is used. To solve this inconsistency, one approach is to ignore the relaxation process but achieve agreement with thermodynamics. A plasma model has been taken into consideration:

$$\varepsilon_p(\omega) = 1 - \frac{\omega_p^2}{\omega^2} \tag{2.40}$$

The term $-\omega_p^2/\omega^2$ represents the interaction between photons and free electrons, where the relaxation property has been ignored. In this approach, the same optical data are extrapolated to lower frequencies by means of the simple plasma model with the same plasma frequency of Au.

The Plasma model has advantages over Drude model. Drude model successfully explains currents related to finite conductivity and Joule heating induced by real electromagnetic fields. However, the Drude model violates the third law of thermodynamics: the Nernst heat theorem. It states that the entropy change in a transformation of a physical system approaches zero when the temperature approaches absolute zero. The plasma model consistent with thermodynamics are more applicable to zero-point photons in Casimir physics.

Chapter 3

Chapter 3 Precision Casimir force measurement using frequency shift technique [1]

A comparison between the measurement data of the most precise experiments and theoretical predictions of the Lifshitz theory revealed a puzzling inconsistency of fundamental significance. It was realized [5, 21, 22] that the theory is in conflict with the data at separations below 1 μm if the real part of the conductivity of materials is taken into account in computations. A good agreement between the theory and the data is regained if one neglects the low-frequency relaxation properties of free charge carriers and the dc conductivity in dielectrics. As a result, there were attempts to explain the Casimir puzzle

---

[1] This chapter contains materials published in (1) M. Liu, J. Xu, G. L. Klimchitskaya, V. M. Mostepanenko and U. Mohideen (2019). "Examining the Casimir puzzle with an upgraded AFM-based technique and advanced surface cleaning." Physical Review B 100(8): 081406. and (2) M. Liu, R. Schafer, J. Xu, and U. Mohideen (2019). "Elimination of electrostatic forces in precision Casimir force measurements using UV and Ar ion radiation." Modern Physics Letters A, submitted.

as the role of some unaccounted background effect, i.e., by an additional force due to surface patches.

In this chapter, we describe measurements of the gradient of the Casimir force between Au-coated surfaces of a sphere and a plate by means of a significantly upgraded dynamic AFM based technique with *in situ* UV and Ar ion cleaned surfaces of the test bodies. The components of the setup reported previously [23] are upgraded by incorporating a UV lamp and an Ar-ion gun. This makes possible the removal of contaminants from all interior surfaces of the vacuum chamber and a significant decrease in the residual potential difference between the test bodies (a factor of 10 compared to Ref. [23]). Furthermore, the force sensitivity was improved by the preparation and use of a cantilever with a smaller (factor of 10) spring constant than in the previous work [23]. As a result, the calibration constant in the present measurements is by an order of magnitude larger than in Ref. [23] leading to smaller (by a factor of 6) systematic error in measuring the gradient of the Casimir force. After a comparison between the measurement data and theory, these improvements allowed clear discrimination between two theoretical approaches mentioned above up to a larger separation distance.

Compared to previous experiments, some improvements have been done. The spring constant was reduced by decreasing the thickness and width through chemical etching in KOH solution. After etching the spring constant decreased by a factor of 2. In addition, the Au coating on the sphere and plate was made using an E-beam evaporator. In contrast to the Au coatings done using thermal evaporator in our previous experiments [23], the roughness here is reduced by a factor of 2 with E-beam evaporators. The use of the combined

UV and Ar ion *in situ* cleaning leads to the reduction of the role of electrostatic forces. In addition the vacuum used during the measurement is reduced from 3×10^{-8} Torr to 5×10^{-9} Torr leading to stable residual surface potentials [23].

3.1 Reduction of spring constant of cantilever and fabrication of sphere attached cantilever

To improve the precision of the measurements, the sensitivity of the cantilevers has to be increased. The most direct way of achieving this is through a decrease of the cantilever spring constant. Specialized cantilevers without the AFM pyramidal tip allow better attachment of spheres and were therefore used. The cantilever spring constant is given by equation below.

$$k = \frac{Ywt^3}{4L^4} \tag{3.1}$$

Where Y is Youngs modulus, t is thickness, L is the length and w is the width of the rectangular cantilevers used. From Eq. 3.1 the spring constant can be most effectively decreased by reducing the thickness and width of the beam.

The first step in cantilever etching process was to rinse the cantilever with buffered HF solution (BOE 6:1) for 1 minute followed by DI water to remove oxide layer. Then, the cantilever was etched with 60% KOH solution at a temperature of 50 °C for 55 seconds. Mild agitation by hand leads to uniform etching. High concentration and high temperature were necessary factors to achieve surface smoothness after etching [24]. The reduction in the thickness and width of the cantilever beam lead to a decrease of the spring constant. The

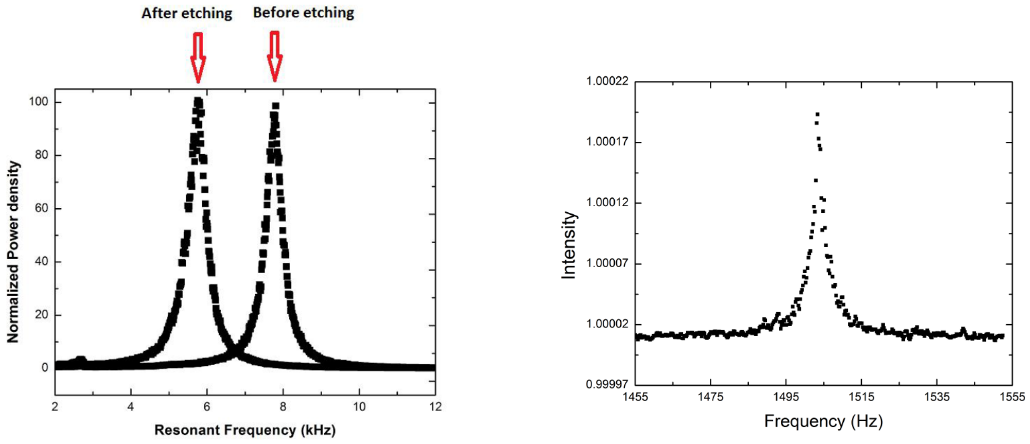

(a) (b)

Figure 3.1: (a): Resonant frequency shift of the cantilever due to decrease of spring constant after etching. (b): After sphere attachment and Au coating, the resonant frequency of sphere attached cantilever is 1503.4 Hz measured using a FFT spectrum analyzer.

spring constant was measured using the thermal oscillation spectrum of the cantilever as discussed in Ref. [25]. After the etching process, the spring constant and resonant frequency reduced from its original values 0.04630 N/m and 7.762 kHz to 0.02156 N/m and 5.743 kHz, respectively, shown as in Fig. 3.1(a). These measurements were made in ambient air and at room temperature.

The next step was the attachment of the sphere to the tip of the cantilever. Hollow glass spheres were prepared as described previously in Ref. [23, 26]. The spheres were baked at 60 °C for 2 hours to remove the volatile components. Then, hollow glass sphere of diameter 86 μm was picked up using a stripped optical fiber and attached to the cantilever. The diameter was roughly estimated using the optical microscope at this step. A very small amount of conductive silver epoxy was applied on the cantilever tip prior to the attachment. The process of attachment was performed under an optical microscope.

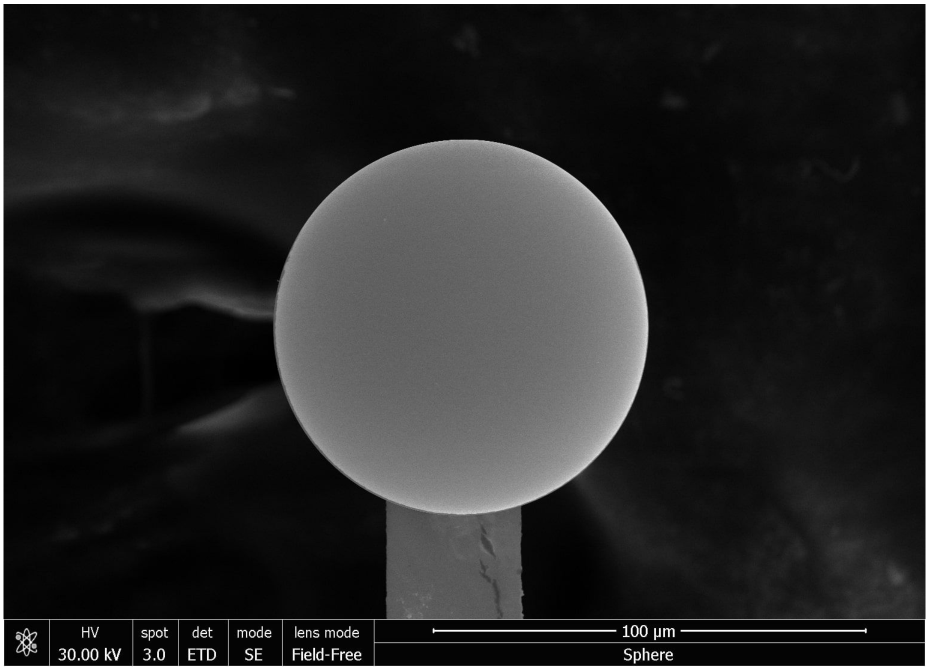

Figure 3.2: The image of sphere-cantilever system taken by scanning electron microscope (NNS450, Nova NANO SEM system, FEI).

Following the attachment of the sphere, Au coating was evaporated on the cantilever and the sphere using a E-beam evaporator at a pressure of 5×10^{-6} Torr. The Au coating speed was 2 Å/sec. To improve the finesse of the Fabry-Perot cavity of the interferometer, the reflective of the top side of the cantilever was increased by coating with 40 nm Au (Too thick a coating decreases the mechanical quality factor Q of the cantilever). The bottom side of the sphere was coated with 130 nm Au. While coating the top side of the cantilever, it was tilted by 40 degrees to guarantee good overlap between the two Au layers overlap leading to a continuous Au film. After the Au coating, the resonant frequency decreased to 1.503 kHz in ultra high vacuum shown as in Fig. 3.1(b). The example SEM image of fabricated sphere attached cantilever is shown as in Fig. 3.2. The image was imported into software "ImageJ" for analysis. The diameter was identified by taking multiple

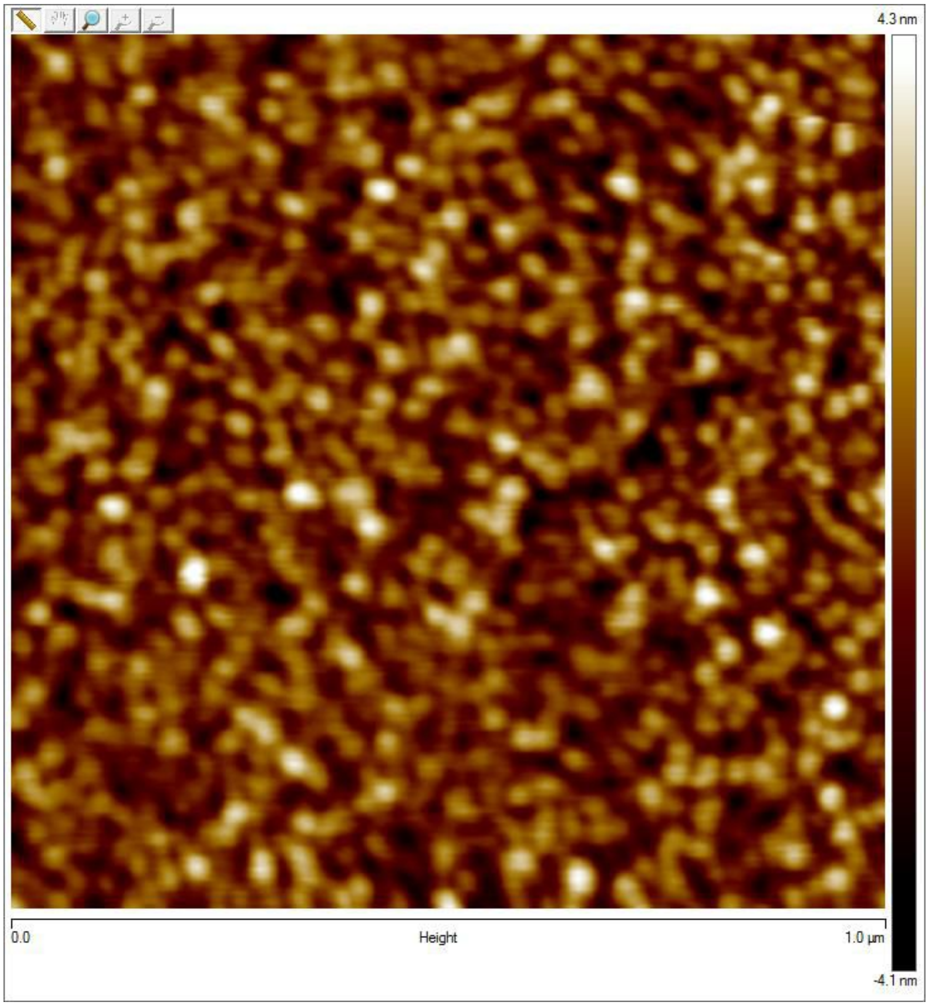

Figure 3.3: The AFM scan of Au surface on the sphere. The scan size was chosen to be as small as 1 μm to reduce the spherical background. The second order background subtraction was used to flatten the surface before measuring RMS roughness. The roughness of 1.13 nm was obtained by averaging multiple values of RMS roughness at different locations. The roughness measurement was done after the experiment.

slices and choosing the longest one. The total error in diameter has three contributions. The systematic error of 75 nm was obtained by comparing the diameter values at the same position but from different orientations of electron beam. The resolution error of 16 nm was given by the highest pixel density of the SEM. The random error of 35 nm was computed using diameter values at different positions. The diameter is determined to be 86892 ± 84 nm.

In contrast to thermal evaporators used previously, the E-beam evaporator leads to smoother surfaces and lower roughness. The RMS roughness on the sphere and the plate, measured after the experiment was completed, is $\delta\mathrm{s} = 1.13$ nm and $\delta\mathrm{p} = 1.08$ nm (compared with $\delta\mathrm{s} = 2.0$ nm and $\delta\mathrm{p} = 1.8$ nm in Ref. [23]). A sample image of Au surface on the sphere measured using AFM is shown as in Fig. 3.3. The decrease in roughness was also achieved by using silicon plates instead of sapphire or fused silica plates used in previous measures. Polished silicon wafers are used in semiconductor manufacturing and thus have much lower roughness.

3.2 Experiment setup

We use a custom built atomic force microscope (AFM) based setup to measure the Casimir force between an Au coated sphere and plate. The schematic of the experiment setup is shown in the Fig. 3.4. The experimental setup was placed inside a stainless steel vacuum chamber (conflat flange 6 way 10 inch cross). An oil free mechanical scroll pump and a turbo pump are connected in series to achieve a pressure down to 10^{-9} Torr. Lower pressures were also achieved by using the ion-pump. The Au sphere is attached to a Si microcantilever. The resonance frequency shift of this cantilever is measured using an optical interferometer and it corresponds to the gradient of the sphere plate force. The Au coated sphere-cantilever system is attached to two block piezoelectric actuators. The cantilever is electrically grounded. The cantilever motion is monitored with a laser optical interferometer. The laser light source has a wavelength of 1550 nm. Single mode 1550 nm fibers are used. An 1cm × 1cm × 500 μm silicon wafer coated with 120 nm Au is used as the plate in the force measurement. Au coated polished silicon wafers are used as the plate as the surface roughness is less than with the Au coated sapphire or fused silica plates used previously. The silicon wafer was HF washed prior to evaporation of the Au coating. The plate is mounted on a piezoelectric tube which is used to precisely control position of the Au plate. The piezoelectric tube is mounted on a XYZ linear translational stage used for coarse approach of the plate to the sphere. The second interferometer using a wavelength of 520 nm is used to measure the movement of the Au coated plate. The Au plate is connected to a function generated which can be used to apply different voltages to the plate.

The use of Ar ion gun for surface cleaning has been reviewed earlier [26]. The Ar ion gun is horizontally installed on left side of the chamber as shown in Fig. 3.4. The Ar ion gun is mounted such that there is a clear line of sight to both the sphere and plate. With horizontal mounting, Ar ions impact the surface at grazing incidence preventing sputtering and deep penetration of the Au surface. A gas reservoir filled high purity (99.99%) Ar gas connected to the chamber is used as the source of the ions.

A Ultra-violet lamp is installed inside vacuum chamber as a new improvement. With the use of UV light the vacuum was improved from 3×10^{-8} to 5×10^{-9} Torr. We

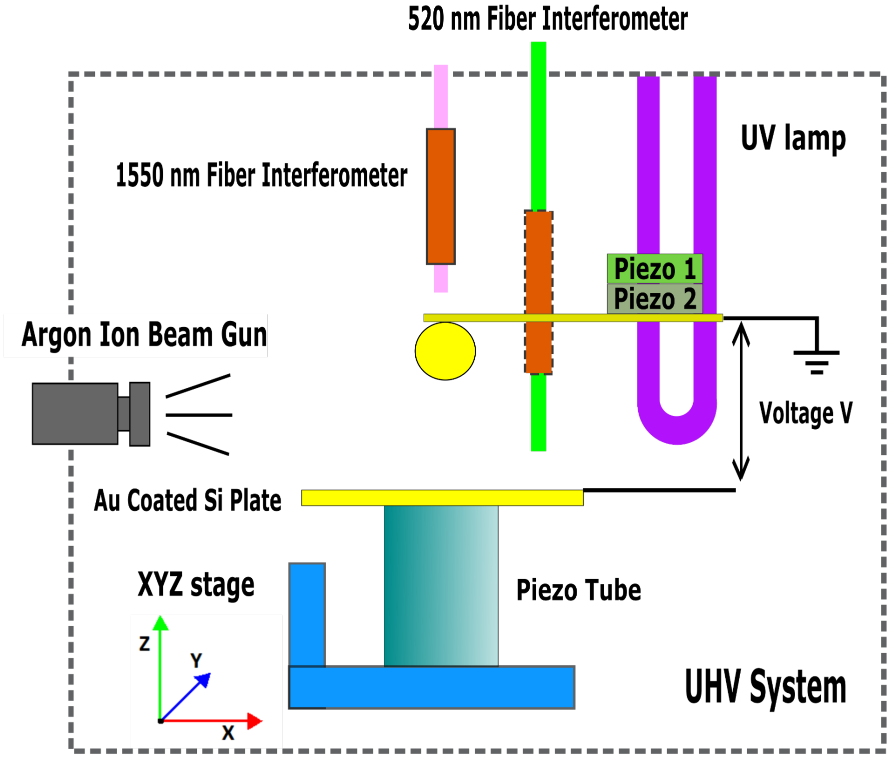

Figure 3.4: Experimental Setup.

used the UV lamp (UVB-100 Water Desorption System, RBD Instruments, Inc.) with dimensions of 10.5” length and 1.3125” diameter. It is installed on the top of the chamber using a 2.75” flange as shown in Fig. 3.4. The lamp uses a hot cathode mercury (Hg) discharge tube as emitter. The emitted wavelengths are a combination of 185 nm (30%) and 254 nm (70%). The radiated power was approximately 5 W of surface area at 254 nm wavelength and 2 W at 185 nm wavelength. The 185 nm wavelength is important because it is absorbed by oxygen, and it thus leads to the generation of ozone. The 254 nm radiation is not absorbed by oxygen and therefore does not lead to ozone production. However, the 254 nm wavelength is absorbed by most hydrocarbons and ozone leading to their ionization and disintegration.

3.3 Vacuum importance and UV cleaning

A good vacuum condition is critical for measurements as the absence of surface contaminants is central to the reduction of the electrostatic force. The experiment setup was placed inside a stainless steel vacuum chamber. A mechanical scroll pump and a turbo pump are connected in series to achieve a pressure down to 10^{-9} Torr. Further reduction in pressure is achieved by using the ion-pump. During force measurements only the ion pump is used so as to keep the background mechanical noise to a minimum. Higher pressures imply the presences of gas phase molecular impurities which would lead to contamination of the Au surfaces causing electrostatic patch effects. These can lead to a residue potential difference (V_0) of the two Au surfaces. The desorption of contaminants from the chamber walls and their deposition on the Au surfaces leads a time dependent V_0. To reduce the drift rate of V_0, an ultra low and stable pressure is necessary to improve the precision of the force measurements. We have measured the drift rate of the V_0 at different chamber pressures. At a pressure of 1×10^{-7} Torr, the V_0 drift rate is around 0.1 mV/min. At lower pressures of 5×10^{-9} Torr, the V_0 drift rate is less than 0.005 mV/min.

In surface physics, contaminant free stable surfaces require the use of an ultra high vacuum. This is traditionally achieved by pumping out the interior as well as organics and water molecules adsorbed on the surface of the experimental chamber. The experimental chamber is cleaned through a baking procedure prior to experiments. The temperature of the chamber is increased to more than 200 °C to desorb all contaminants from the entire chamber which are then pumped out. But this procedure cannot be adopted in our Casimir force measurements as changes in temperature will lead to misalignment of the two interferometers because of thermal expansion. We have found that a combination of *insitu* UV and Ar ion cleaning allows us to achieve ultra high vacuums of 5×10^{-9} Torr resulting in clean sphere plate surfaces with low and stable V_0.

The removal of contamination on the Au sphere-plate surfaces using only the Ar ion gun followed by a Casimir force measurement has been studied in Ref. [26]. The residual potential V_0 was lowered by an order of magnitude by Ar ion cleaning [26] leading to a reduction in the detrimental role of electrostatic forces. In Ar ion gun cleaning the ions are focused to the interacting sphere-plate surface. Therefore the adsorbed contaminants on the experimental chamber walls are not removed. Thus while the Ar ion cleaned Au surfaces have lower V_0, over longer periods of time the desorption of contaminants from the chamber walls leads to the redeposition of contaminant gas molecules on the Au surfaces leading to a change in V_0. However, UV radiation can reflect off inner surfaces of the chamber leading to excellent coverage of the entire chamber. A procedure of combining UV radiation cleaning and Ar ion bombardment has been developed to improve vacuum condition during experiment.

The action of UV light and ozone has been utilized since 1972 as a method of cleaning and removing organic contamination [27, 28]. UV cleaning has now become an effective and established method of removing contaminants from surfaces and is widely used [29]. The properties of Au surfaces after UV irradiation have been particularly studied due to the importance in the semiconductor industry. The current understanding [27] indicates that UV/ozone cleaning is primarily the result of photosensitized oxidation processes. The contaminant molecules are excited and/or dissociated by the absorption of UV light. In addition, atomic oxygen and ozone which are produced when oxygen is dissociated by the absorption of 185 nm UV light. UV based cleaning thus appears to involve the initial oxidation of surface hydrocarbons to species with oxygen functional groups. Following this more volatile species are produced by further oxidation. The contaminants can be removed from the chamber walls as well as the sphere-plate surfaces by the use of UV light. The UV light can also desorb water vapor and decompose oxidative hydrocarbon from chamber wall. During UV irradiation, the partial pressure of oxygen decreased, while that of CO_2 and H_20 increased [30]. These volatile species can then be pumped out of the vacuum chamber.

Extended UV/ozone exposure for long periods results in the formation of Au_2O_3 on the Au surface. This is a weakly bound oxide that decomposes on heating to 150 °C [31]. In Ref. [32] X-ray photoelectron spectroscopy (XPS) was used to determine the parameters for a successful UV/ozone cleaning of gold surfaces at 1×10^{-6} Torr. It was found the cleaning time should be limited to 10 min, and that it is useful for only a few monolayers of hydrocarbon contamination. Thus, for removal of all contamination additional surface cleaning such as with Ar ion beams might be necessary. Even though UV has proven to be very effective in removing water and organic contaminants the removal of inorganic contaminants from surfaces would need additional methods as Ar ion beams.

3.4 UV/Ar cleaning procedure

In our preliminary experimentation on UV cleaning, the vacuum chamber was first pumped down to a pressure of about 9×10^{-9} Torr using the scroll mechanical pump and the turbo pump. The ion pump valve was closed to avoid contaminating the ion pump. The Au Sphere-Au plate separation was kept around 500 μm. For a typical case shown in Fig. 3.5, the residual potential difference V_0 was around -15 mV before the start of cleaning. Next, the UV lamp was turned on for 0.5 sec. The organic and water contaminants were released from all surfaces of the vacuum chamber including the Au sphere and Au plate. The rough measurement of V_0 was performed within 1 min after UV lamp was turned on. Here the mean of two applied plate voltages which lead to the same frequency shift was used as an estimate of V_0. Next, the UV light was tuned on for another 0.5 sec after which the V_0 measurement was again done. This was repeated with 0.5 sec of UV irradiation till the total irradiation time was 55 sec after which the UV radiation was done in 5 sec and 10 sec steps. In Fig. 3.5, the measured sphere-plate potential difference V_0 is shown as a function of integrated UV radiation time. The V_0 is shown to stabilize at around 250 mV after 120 secs of UV irradiation. Typical UV irradiation times of 10 mins were used in our experiments. The increase in the value of V_0 is probably due to the remaining presence of inorganic surface impurities and potential formation of Au_2O_3.

For a typical UV cleaning procedure shown here, the vacuum chamber was first pumped down to pressure of about 9×10^{-9} Torr using the scroll mechanical pump and the turbo pump. The UV lamp was turned on for 10 mins. As previously described the UV light leads to formation of ozone and atomic oxygen which results in the oxidation of

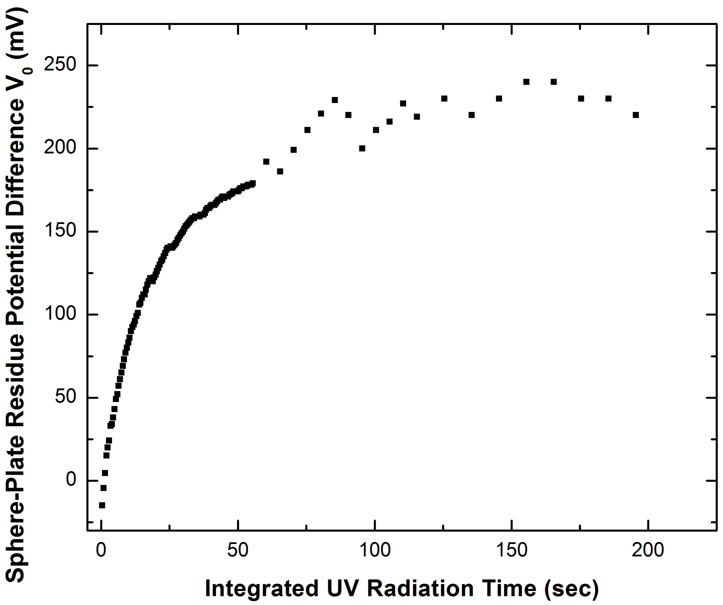

Figure 3.5: The Au sphere-plate residual potential difference V_0 shown as a function of the integrated UV radiation time. The V_0 was found to stabilize after 120 secs of UV radiation.

surface hydrocarbons to species to more volatile species. This process raised the chamber pressure to 8×10^{-7} Torr. During the UV cleaning process, the ion pump valve was closed to avoid contaminating ion pump. The volatile species released by UV light were pumped out by the turbo pump and mechanical pump. A rough measurement of the V_0 was done to study this behavior for a sphere-plate separation of 1 μm. For this case, the residue potential difference V_0 was 49.6 ± 0.3 mV before any cleaning. During and immediately past (up to even 60 mins) the UV treatment measurements were not possible due to the fluctuating interferometer signal. V_0 measurements had to be performed after the signal was stabilized. The V_0 reaches a high value approximately 100-200 mV after the UV lamp was turned off for 60 minutes.

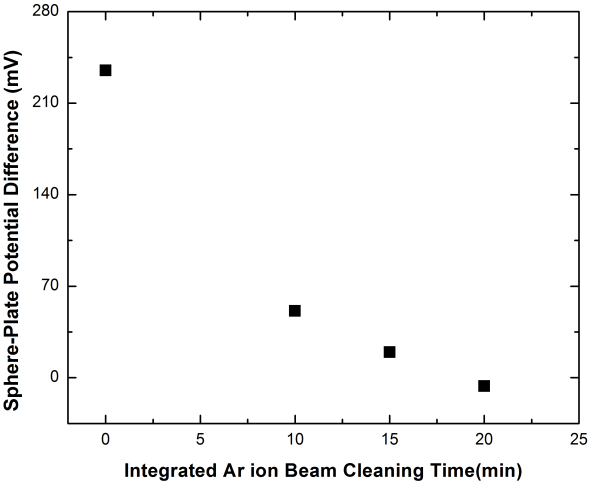

Figure 3.6: The Au sphere-plate residual potential difference as a function of the Ar ion cleaning time.

To remove any addition organic and inorganic contamination and Au oxide on sample surfaces, Ar ion beam bombardment was used after UV cleaning process. For Ar ion cleaning the plate-sphere distance was about 500 μm. During Ar ion cleaning, the ion pump was shut off as well because Ar gas contaminates ion pump electrodes. To initiate the process, the Ar gas was released into the chamber until the pressure reached 1.2×10^{-5} Torr. The turbo pump gate valve was half closed to keep the pressure constant. The Ar ions were accelerated under 500 V electric field. The kinetic energy of Ar ions was high enough to break chemical bonds of organic molecules and Au oxide but low enough to prevent any sputtering of the Au surface. The anode current of 4 micro-Amp was used as flux of ion beam. The filament current was 2.1 Amp. At these conditions, the Ar ion cleaning was done for 5 min steps. After each 5 min cleaning step the turbo pump gate valve was opened the pressure allowed to reach 5×10^{-9} Torr in less than 30 mins. Next the V_0 value was measured. This process was repeated till the V_0 reached nearly zero. In this particular case the measured V_0 after cleaning was 2.0 ± 0.3 mV. The complete Ar ion cleaning time was typically between 20-30 mins.

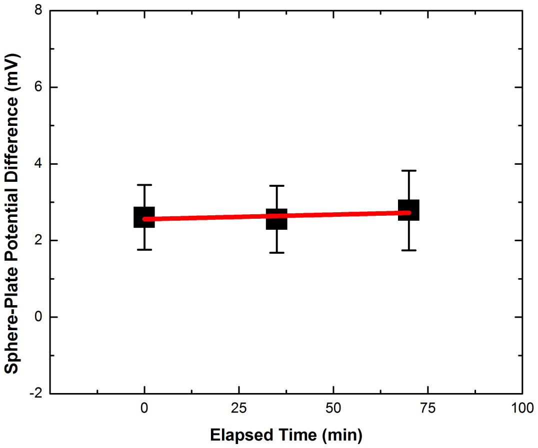

Figure 3.7: The sphere-plate potential difference V_0 for the UV and Ar ion beam cleaned sample is plotted as a function of time.

The advantages of the UV and Ar ion cleaning procedure are the lower vacuum pressures that are achieved and long time stability of V_0. As UV radiation leads to the removal of volatile molecular species adsorbed on the walls of the vacuum chamber, a factor of 10 decrease in the vacuum pressure can usually be achieved. In addition, the cleaner vacuum chamber results in much decreased recontamination rate of the sphere-plate surfaces. After the Ar ion beam cleaning step the sphere-plate potential difference V_0 is near zero and stable for much longer periods of time. In Fig. 3.7 the sphere-plate potential difference V_0 for the UV and Ar ion beam cleaned sample is plotted as a function of time. The vacuum chamber pressure was 5×10^{-9} Torr with both the turbo and ion pump being used. As shown in Fig. 3.7 the V_0 drift rate is 0.002 mV/min. This long time stability of the near zero V_0 allows for unambiguous and stable measurement of the Casimir force.

3.5 Force gradient measurement procedure and analysis

After UV radiation and Ar ion bombardment the samples are clean and ready for the Casimir force measurement. For the case shown here, the V_0 value is determined to be 2 mV using rough measurement. To reduce mechanical noise the ion pump was turned on and the gate valve to the turbo pump was closed and the mechanical pump and the turbo pump were turned off.

The force gradient between the sphere and plate was measured through the resonant frequency shift of the cantilever attached to the sphere. The frequency shift corresponding to the sphere-plate forces was recorded as function of the sphere-plate separation distance. The relative sphere plate separation distance is controlled by application of voltage to the piezoelectric tube supporting the plate as shown in Fig. 3.4. The distance moved by the plate is calibrated using the interference fringe from the 520 nm fiber interferometer. An example of interference fringe is shown as in Fig. 3.8. The below equation converts applied voltage to distance moved by piezo tube. The distance obtained here is relative sphere-plate separation.

$$P_{out} = P_{effective}(1 + \gamma \cos \frac{4\pi}{\lambda}(P_1 V + P_2 V^2 + P_3 V^3 + \dots)) \tag{3.2}$$

where P_{out} is the output signal of the interferometer, $P_{effective}$ is the effective input signal, λ is the wavelength of laser source, γ is the visibility considered as a constant here and

$P_i, i = 1, 2, 3...$ are the piezoelectric coefficients corresponding to the "ith" order of the voltage V.

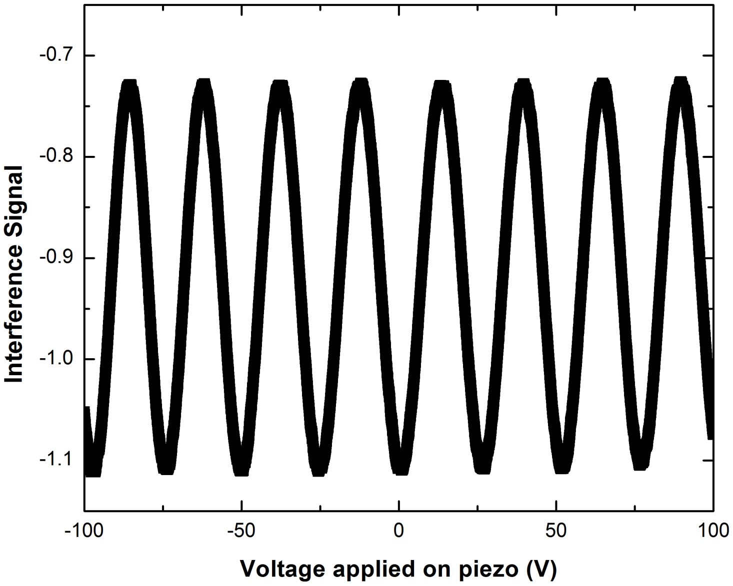

Figure 3.8: The interference signal monitored by a 520 nm fiber interferometer was recorded as function of voltage applied on piezo tube.

After the collection of the frequency shifts as a function of sphere-plate separation distance, we subtracted any small drift in the frequency-shift signal. For this purpose, we used the fact that for separations larger than 2.5 μm the total force between the sphere and plate is below the instrumental sensitivity. At these separations, the noise is far greater than the force gradient signal and in the absence of systematic errors the signal should average to zero. In addition, to take into account any small long term background systematic frequency shifts within the noise coming from the movement of the piezo the sphere-plate separation distance is increased to 50 μm, where the sphere-plate interaction force gradients are well beyond the experimental sensitivity. At this average separation the frequency shift measurement is repeated by moving the plate with the piezo in through the same distance of 2.8 μm with V_0 applied to the plate. After averaging 8 frequency shift measurements the background change in frequency due to the mechanical movement of the plate can be found to be linear at 1.5×10^{-6} Hz/nm. This small background noise signal due to the plate movement is subtracted from all frequency shift signals. In comparison the frequency shift due to the Casimir force at 250 nm is 6.3 Hz.

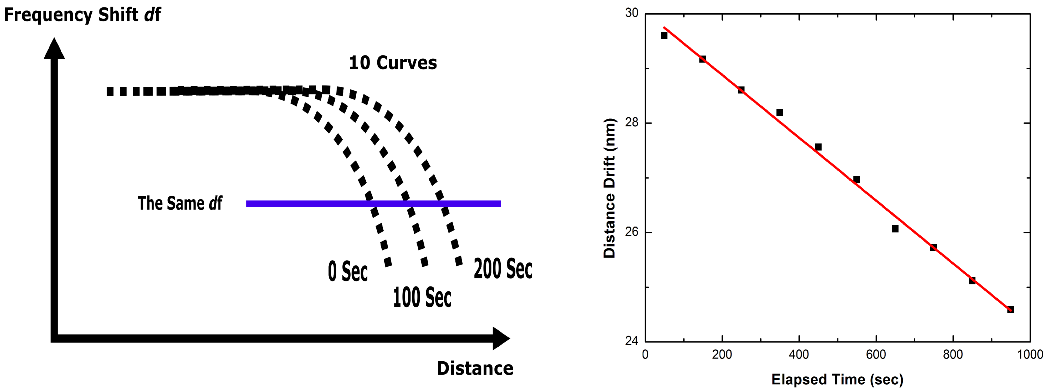

(a)

(b)

Figure 3.9: (a): The curve of frequency shift as function of distance was taken every 100 sec. The same frequency shift corresponds to the same sphere-plate separation. (b): The relationship between distance change and accumulated time was found to be linear. For the case as shown here, the drift rate is -0.00575 nm/sec.

For the force gradient measurement, 11 applied voltages between -49 to +51 mV (in steps of 10 mV) were applied to the plate and the cantilever resonant frequency shift measured as a function of the plate movement. Next, the estimated V_0 of 1 mV was applied to the plate and the frequency shift recorded as a function of the plate separation. This was repeated 10 times to measure the correction due to the drift in sphere-plate separation.

Shown as in Fig. 3.9(a), 10 continuous measurements of frequency shift were repeated as function of the relative sphere-plate separation with the same applied voltage to the plate. The change in position corresponding to one frequency shift is plotted as a function of elapsed time as shown in Fig. 3.9(b). The slope gives the mechanical drift rate of -0.00575 nm/sec. Then, this value was used to correct separation distances in all measurements.

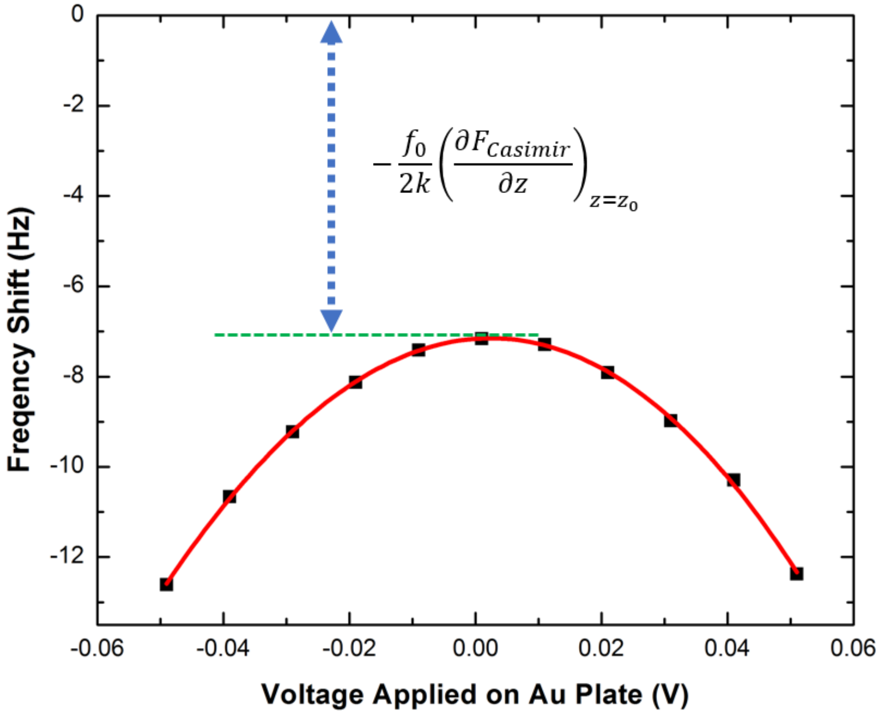

Figure 3.10: The frequency shift has a parabolic response to applied voltage on the plate. The vertical component of the vertex is the frequency shift caused by Casimir force. The horizontal component of the vertex is the V_0 at the present distance.

We use electrostatic force theory to do calibration. The frequency shift has contribution from both the electrostatic force and the Casimir force:

$$\Delta f = -\frac{f_0}{2k}\left(\frac{\partial F_{ele}}{\partial z} + \frac{\partial F_{Cas}}{\partial z}\right)_{z=z_0} = \beta(f_0, k, R, z)\cdot(V - V_0)^2 + \frac{f_0}{2k}\cdot\frac{\partial F_{int}}{\partial z} \tag{3.3}$$

where $\Delta f = f - f_0$ is the frequency shift, f_0 is the resonant frequency (1503.4 Hz) of the cantilever in ultra high vacuum, F_{ele} and F_{Cas} are electrostatic force and Casimir force respectively, k is the spring constant of the cantilever. The parameter β is given by:

$$\beta(f_0, k, R, z) = \frac{\varepsilon_0 f_0}{2k} \sqrt{\frac{1}{z(z+2R)}} \sum_{n=1}^{\infty} \times$$
$$\csc(n\alpha)\{n \coth n\alpha[n \coth n\alpha - \coth \alpha] - \csc^2 \alpha + n^2 \csc^2(n\alpha)\} \quad (3.4)$$

where ε_0 is the dielectric permittivity in vacuum, $\cosh(\alpha) = 1 + z/R$, and R is the sphere radius (43.446 μm) measured using scanning electron microscopy. At a given separation, the frequency shift is proportional to the square of the voltage difference. Therefore, the parameters β and V_0 can be obtained by fitting parabolas and plotted as function of distance.

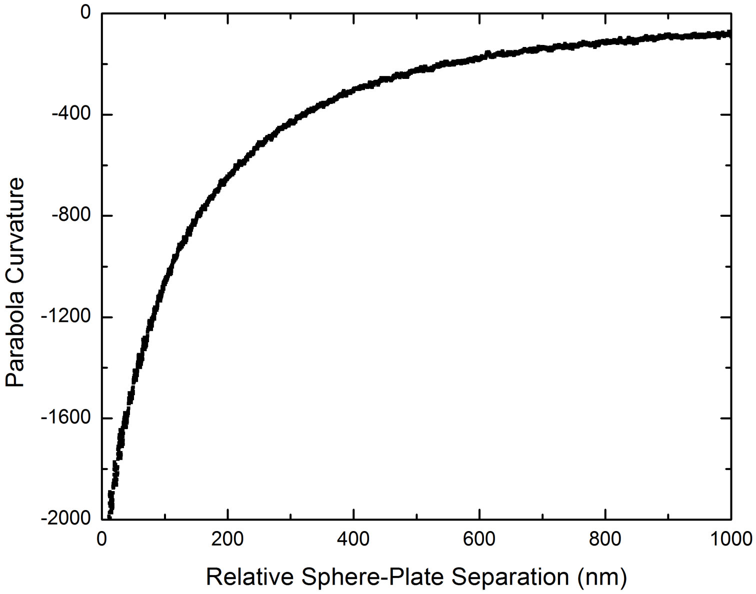

Figure 3.11: The curvature of parabola ($\beta(f_0, k, R, z)$) is plotted as function of relative separation distance.

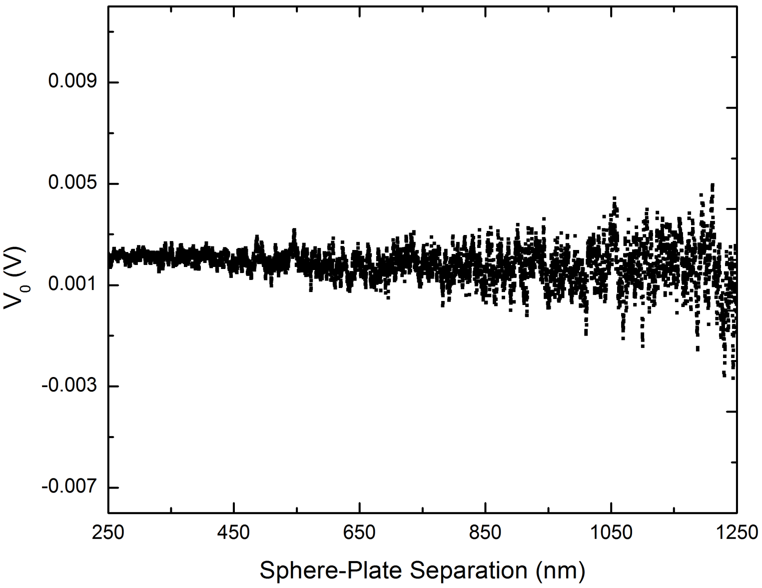

Figure 3.12: The residual potential difference between Au-coated surfaces of a sphere and a plate is shown by dots as a function of separation.

The point of closest sphere-plate separation z_0 has to be added to the relative distance z_{rel} moved by the plate to obtain the absolution separation $z = z_0 + z_{rel}$. Then the best fits of Eq. 3.4 to the measured β is done to obtain the parameters z_0 and $C = f_0/2k$ shown as in Fig. 3.13. From this the force gradient of Casimir force $\partial F_{Cas}/\partial z$ was calculated using Eq. 3.3 and above fitting parameters. Then the best fits of the exact expression for $\beta(f_0, k, R, z)$ to the measured data was done leading to $z_0 = 240.2 \pm 0.6$ nm and $C = (1.030 \pm 0.002) \times 10^5$ s/kg. The z_0 and C are plotted as function of distance shown as in Fig. 3.13(a) and Fig. 3.13(b). V_0 can be found by fitting parabolas and be plotted as functions of distance. The V_0 obtained at each separation are shown in Fig. 3.12 resulting in the mean value $V_0 = 1.93 \pm 0.01$ mV. In previous reports performed with specially selected samples, possessing constant but larger V_0, the gradient of the total measured force was also larger. However, the gradients of the Casimir force obtained in Ref. [23] after a subtraction of electrostatic contributions are in good agreement with the measurement results obtained here at higher precision over the wider separation region.

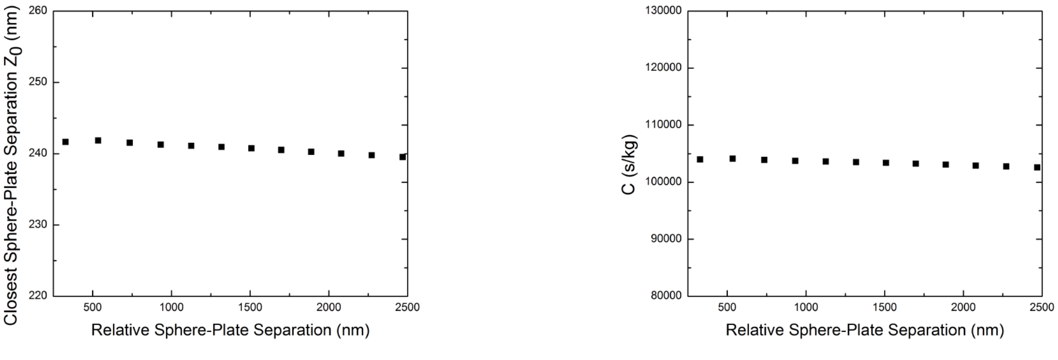

(a) z_0 vs. distance (b) C vs. distance

Figure 3.13: The closest distance z_0 (a) and the parameter C (b) as function of distance is obtained by making a fit between β curve and electrostatic force equation.

After completion of the calibration, the force gradient of the Casimir force was calculated with a step of 1 nm using Eq. 3.3 and the above parameters C, z_0, and V_0. The obtained results are presented in Figs. 3.14 as crosses over different separation regions. The arms of the crosses show the total experimental errors determined at the 67% confidence level (random and systematic errors added in quadrature). In so doing, the systematic error in the measured gradient of the Casimir force is mostly determined by the systematic error in measuring the frequency shift which is equal to 8.8 mHz in this experiment.

The gradient of the Casimir force in the experimental configuration was computed in the framework of the Lifshitz theory taking into account corrections to the proximity force approximation and surface roughness. The thicknesses of the Au coatings on the

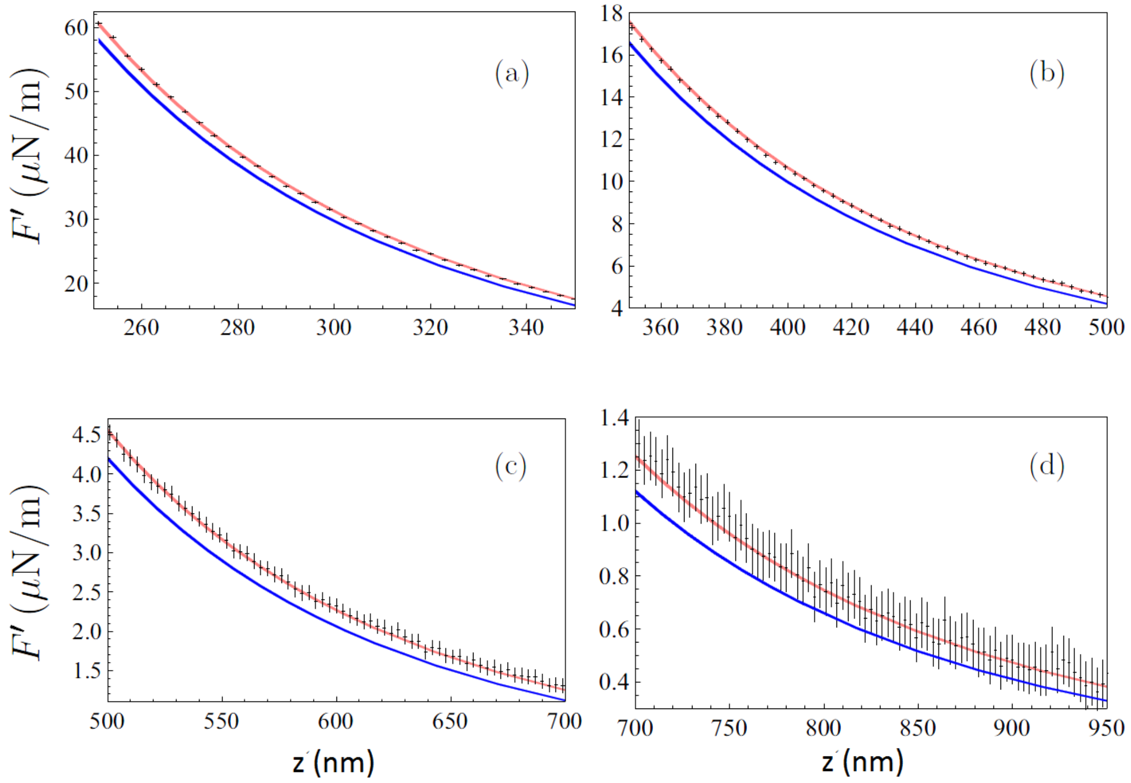

Figure 3.14: The measured gradient of the Casimir force as a function of separation is shown as crosses. The arms of crosses indicate the total experimental errors (for better visualization the measurement results are shown with the step of 3 nm). Theoretical predictions of the Lifshitz theory with neglected and included energy losses of conduction electrons are shown as the upper and lower bands, respectively.

sphere and the plate were 118 ± 1 nm and 120 ± 1 nm, respectively. This is more than sufficient for these coatings to be considered as infinitely thick. As a result, the gradient of the Casimir force is expressed as:

$$F'(z) = -2\pi R[1+\beta(z,R)\frac{z}{R}]\big(1+10\frac{\delta_s^2+\delta_p^2}{z^2}\big)P(z), \qquad (3.5)$$

where $P(a)$ is the Casimir pressure between two Au semispaces and the function β quantifies corrections to the proximity force approximation [33, 34].

Computations have been made at the 20°C which is the experiment temperature.

The values of dielectric permittivity were obtained from the tabulated optical data for Au extrapolated down to zero frequency either by the Drude model taking into account the energy losses of conduction electrons or by the plasma model which neglects these losses [5, 21]. The computational results are shown in Fig. 3.14 by the upper and lower bands computed when using the optical data extrapolated by the plasma and Drude model, respectively. The widths of the bands reflect the theoretical errors which are mostly determined by the inaccuracies in the optical data.

As is seen in Fig. 3.14, the predictions of the Lifshitz theory with the inclusion of energy losses of conduction electrons are excluded by the measurement data up to the separation distance about 820 nm. At the same time, the predictions of the same theory with the energy losses of the conduction electrons neglected are in excellent agreement with the data. The same conclusion, but at separations up to 420 nm was obtained earlier by means of the dynamic AFM [23] and at separations up to 750 nm by means of a micromachined oscillator [5, 21, 35, 36, 37].

3.6 The Casimir force gradient measurement with larger oscillation amplitude of the cantilever

The frequency noise of Phase-Locked Loop (PLL) can be reduced by increasing the cantilever oscillation amplitude. The oscillation amplitude of cantilever was controlled with the AC voltage applied to the piezo driving the cantilever. The oscillation amplitude of cantilever was roughly measured using an interferometer. The resolution error of the PLL was measured using a function generator. A pure sine wave of the same frequency and amplitude as the oscillation of cantilever was input into the PLL from the function generator. The standard deviation of 1000 accumulated data points was used as the resolution error of the frequency shift. The resolution frequency noise was 8.8 mHz for a regular cantilever oscillation amplitude of 10 nm for the previous experiments, while the resolution noise was reduced to 6.2 mHz if the amplitude is increased to 20 nm. The following experiment demonstrates the Casimir force gradient measurement with the larger oscillation amplitude of 20 nm. Additional UV radiation cleaning and Ar ion beam bombardment were not used prior to the measurement. The sphere attached cantilever was the same as the one used in the experiment discussed in the last section. The measurement procedure and data analysis method were the same as that of the previous experiments. The assumption that the force gradient is proportional to the frequency shift is based on the first order approximation in the expansion of the interaction force. The measurement with larger amplitudes requires that the closest separation distance z_0 to be also larger for the approximation to hold. Therefore, the measurement was taken for separation distance at 600 nm - 2000 nm. The results are shown as in Fig. 3.15.

Due to the reduction of frequency noise, the Casimir force at a longer separation distance was measured with less error. The measurements with a larger amplitude agree with the dissipation neglected plasma model and exclude the Drude model with the inclusion of dissipationfor separations up to 1.1 μm at 67 % CL.

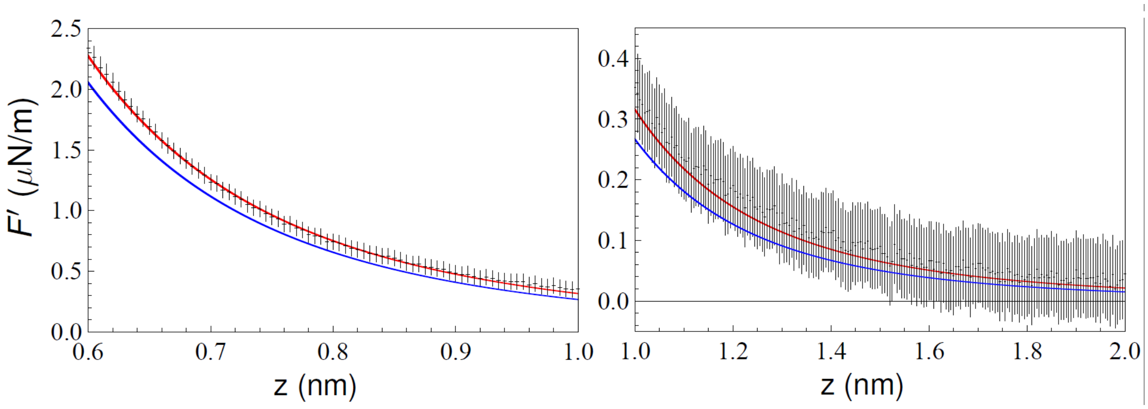

Figure 3.15: The measured gradient of the Casimir force as a function of separation is shown as crosses. The arms of crosses indicate the total experimental errors. Theoretical predictions of the Lifshitz theory with neglected and included energy losses of conduction electrons are shown as the upper and lower bands, respectively

3.7 Summary for experiment using frequency shift technique

To conclude, in this experiment we reconsider the problem which remains a long-standing puzzle. In doing so, special experimental efforts have been taken to avoid any impact of electrostatic patches on the measurement results for the Casimir force. In this experiment, improvement of force sensitivity allowed the measurement of Casimir force gradient at larger separation distance. The model including losses of energy is ruled out at 67% confidence level up to separation distance of 820 nm. The same conclusion was obtained with a higher oscillation amplitude of the cantilever at separation distance up to more than 1 μm. On the theoretical side, due to the long-term efforts of several authors it was shown that the influence of deviations from the proximity force approximation [33, 34], as well as the role of surface roughness [5, 21, 38], does not change the obtained results. Thus, the Casimir puzzle assumes a fundamental importance casting doubts on the basic assumption of quantum statistical physics that a material system responds similarly to electromagnetic fields with nonzero field strength and to fluctuating fields possessing zero field strength and nonzero dispersion. The complete resolution of this problem requires measurements at large separations. The present experiment is a step forward in this direction.

Chapter 4

Chapter 4 Difference Casimir force measurement [1]

In this chapter, a new experiment setup is introduced. In difference force measurement, the difference in the Casimir force between a planar surface and a trench is measured. The background noise is subtracted out. Instead of flat Au coated wafer controlled by a piezoelectric tube, a patterned Au disc with multiple periodical trenches is rotated by an air bearing spindle and the sphere attached cantilever moves in vertical direction. The difference in force between Au surface and vacuum created by deep trenches is measured as function of sphere-spinning disc separation distance. The new method has the potential to achieve a much higher force sensitivity to study Casimir force at larger distance above 1 μm. At the range of a few micrometers, the Casimir force induced by thermal photons fluctuation can be studied [39]. This chapter focuses on design of the experiment system,

---

[1] This chapter contains materials published in: M. Liu, N. Yaraghi, J. Xu, D. Kisailus and U. Mohideen (2019). "Compact fiber optical interferometer technique to measure picometer displacements in biological piezoelectric materials." Measurement Science and Technology, submitted. (preprint arXiv:1905.10970.)

construction of the setup, equipment and preliminary results.

4.1 Motivation to study thermal Casimir force

The previous research improved our understanding of zero-point photons scattering from real materials. Within measured separation range below 1 μm experimental results confirmed that the energy dissipation leading to Joule heating should not be included. But some experiments reported agreement with dissipation included model for larger separation above 1 μm where indirect measurements as the electrostatic force was ten times the Casimir force and was subtracted with fitting parameters. When temperature $T > 0$, the fluctuations come from both zero-point photons and thermal photons. At room temperature T=300 K, the characteristic thermal wavelength $\lambda_T = \hbar c/k_B T = 7.6\ \mu m$. For separations below 1 μm ($<< \lambda_T$), quantum fluctuation is dominated by zero-point photons. If the behavior of thermal photons needs to be experimentally observed, the force measurement should be performed at larger separation distance. The improvement of force sensitivity is necessary to realize such measurements.

Compared to our previous measurements below 1 μm using frequency shift technique, a new method measuring cantilever amplitude is introduced, which uses a spinning patterned wafer controlled by air bearing spindle and which has higher theoretical sensitivity. The periodic pads and trenches are etched along circular annular rings of a silicon disc and coated with Au. The spinning patterned disc is placed below the Au coated sphere shown as in Fig. 4.1. The spindle rotation frequency is much lower than the resonant frequency ω_0 of the cantilever. The disc should be rotated at frequency $\omega = \omega_0/N$, where N

is number of tranches (periods). For case of large value of N, for example $N = 100$, the frequency of background mechanic noise is far from that of the measured signal. The oscillation amplitude of cantilever is measured using interferometer, which will be converted into difference in force between Au surface present and vacuum trench present. In below text, we will estimate possible sensitivity of this technique, which is determined to be 10^{-17}N. This value is precise enough to measure Casimir force at larger separation distance.

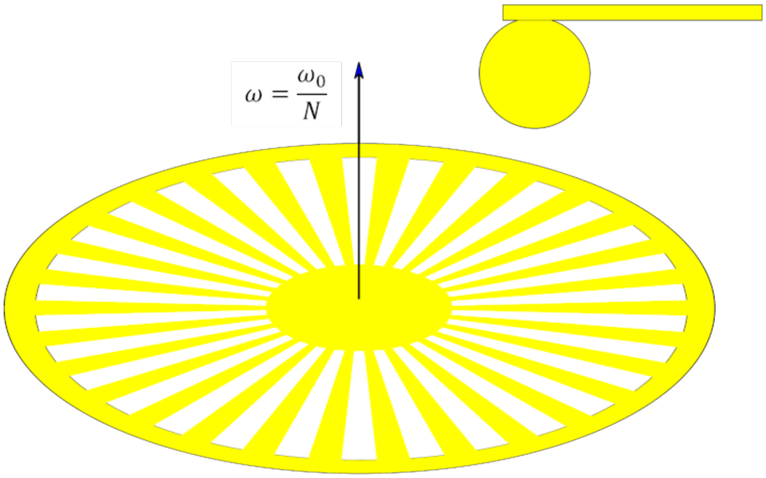

Figure 4.1: A simple schematic of a patterned wafer and the sphere. The Au coated silicon wafer with periodic pads and trenches along a circular ring. In the experiment, multiple circular rings with different diameter are used. The sphere with the cantilever is brought above the spinning wafer. The wafer is rotated at round frequency $\omega = \omega_0/N$, where ω_0 is the resonant frequency of the cantilever, N is the number of periods.

4.2 Measurement principle

The following derivation establishes the connection between differential force and cantilever oscillation amplitude. A preliminary calculation for the ideal case is performed here. Due to the structure of moving periodical trenches, a periodically changing force is considered to oscillate the sphere attached to the cantilever. We assume that the interaction area is much smaller than the trench size. The edge effect is ignored. A step function is used to model the periodical force. When Au surface is right below the sphere, the interaction force is F_{int}. F_{int} is negative because of the attractive force. When a trench is present below the sphere, the interaction force is zero because the depth of the trench is adequate to ignore the force. Therefore, the periodical time dependent force shown as in Fig. 4.2 is $F(t)$ as function of time t.

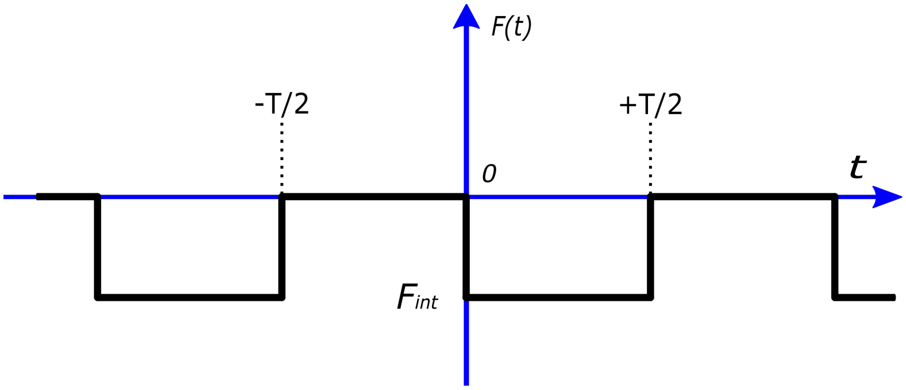

Figure 4.2: The interaction force is a step wave function with period T and amplitude $|F_{int}|$.

$$F(t) = F(t+T) = \begin{cases} F_{int}, & mT < t < (m+1/2)T \\ 0, & (m-1/2)T < t < mT \end{cases} \tag{4.1}$$

where $m = 0, \pm1, \pm2\ldots$ and T is the period. Experimentally, the period can be determined using the spinning frequency ω and number of trenches in one circle N. Therefore, we have relation:

$$T = \frac{2\pi}{\omega N} \tag{4.2}$$

Because the force is a step wave with period T, one can expand a periodical function using Fourier serials:

$$F(t) = \sum_{n=-\infty}^{n=+\infty} F_n e^{i\frac{2\pi n}{T}t}, \quad F_n = \frac{1}{T}\int_{-T/2}^{T/2} F(t) e^{-i\frac{2\pi n}{T}t} dt \tag{4.3}$$

where n is integer and F_n is the Fourier coefficient for component with frequency $2\pi n/T$. The F_n is calculated by integration in one period. Using the expression of $F(t)$, explicit Fourier coefficients are obtained in term of constant F_{int}:

$$F_n = \begin{cases} \frac{F_{int}}{2}, & \text{n} = 0 \\ \frac{2F_{int}}{\pi n}, & \text{n} = 1, 3\ldots \\ 0, & \text{n} = 2, 4\ldots \end{cases} \tag{4.4}$$

Only the zero term and the odd terms exist. The zero term component corresponds to the average force leading to bending of cantilever. The odd terms represent force components that drive the oscillation of the cantilever.

Now let us consider the cantilever oscillating in the presence of an external interaction force $F(t)$. The cantilever has the following properties: the quality factor Q, the resonant frequency ω_0, effective mass m and spring constant k. The instant position of the cantilever is z. The equilibrium position without interaction force is z_0. The differential equation of oscillation is presented as:

$$mz'' + \frac{m\omega_0}{Q} z' + k(z - z_0) = F(t) \tag{4.5}$$

Let $x = z - z_0$ and make Fourier expansion for periodic force $F(t)$, the equation is rewritten as:

$$mx'' + \frac{m\omega_0}{Q} x' + kx = \sum_{n=0}^{n=+\infty} F_n e^{inN\omega t} \tag{4.6}$$

The general solution can adopt this form:

$$x = \sum_{n=0}^{n=+\infty} A_n e^{i(nN\omega t + \varphi_n)} \tag{4.7}$$

where A_n is the oscillation amplitude of frequency $N\omega$ component, and φ_n is the corresponding phase shift. By putting the general solution into the oscillation equation and comparing terms in a series expansion, below equation is obtained:

$$A_n(k - m\omega^2 n^2 N^2 + i\frac{nNm\omega_0\omega}{Q}) = F_n e^{-i\varphi_n} \tag{4.8}$$

The solutions of partial amplitude A_n and phase shift φ_n can be found:

$$A_n = \frac{\frac{F_n}{m\omega_0^2}}{\sqrt{[(\frac{nN\omega}{\omega_0})^2 - 1]^2 + (\frac{nN\omega}{\omega_0 Q})^2}} \tag{4.9}$$

$$\tan\varphi_n = \frac{\frac{nN\omega}{\omega_0}}{[(\frac{nN\omega}{\omega_0})^2 - 1]Q} \tag{4.10}$$

For a general case of F_n, resonance takes place when spindle spinning frequency ω satisfies the following condition:

$$\omega = \frac{\omega_0}{nN}, \quad \varphi_n = \frac{\pi}{2} \tag{4.11}$$

The corresponding amplitude is:

$$A_n(resonance) = Q\frac{F_n}{m\omega_0^2} = Q\frac{F_n}{k} \tag{4.12}$$

The second equality sign is obtained using the additional equation $k = m\omega_0$. If we consider the periodic force in the form of a step wave and use Eq. 4.4, the resonance amplitude is obtained to be:

$$A_n(resonance) = Q\frac{2F_{int}}{\pi k n}, \quad n = 1, 3, \ldots \tag{4.13}$$

Note that the amplitudes for even terms are zero. Especially, for the $n = 0$ term, the bending of the cantilever is given below.

$$A_0(bending) = \frac{F_{int}}{2k}, \quad n = 0 \tag{4.14}$$

This is considered negligible.

4.3 Experimental setup

In this experiment, we still keep use the setup of an Au coated sphere attached to a cantilever. The patterned disc is rotated below the sphere. The periodic structure on the disc causes a change in interaction forces. The difference interaction force is measured as function of the sphere-disc separation. We use the interferometer based technique to measure the cantilever vibration amplitude and convert it to a differential force. The separation distance is obtained using a second interferometer. To reduce mechanical noise, the spinning disc is mounted on the top of an air bearing spindle. The main body of the spindle motor is operated in air, while the disc needs to spin in vacuum. A special structure was designed. It contains a skirt and a circular groove matching each other using vacuum compatible oil as sealant. To achieve above goals, a vacuum chamber equipped with air bearing spindle has been built. In addition, mechanical stages system, optical interferometers system, electronics system and software have been developed.

In this experiment, fabrication process of the cantilever and sphere is the same as in previous experiment. The tipless silicon cantilever is used. The cantilever is rinsed with HF solution to remove oxide layer. Then the cantilever is etched using hot 60% KOH solution. The spring constant of the cantilever is reduced. The hollow glass sphere of diameter 100 μm is attached to the cantilever using conductive silver epoxy. The bottom of the sphere is coated with 130 nm Au using E-beam evaporator. The topside coating of 40 nm Au is used for reflection. After above process, the resonant frequency of the sphere attached cantilever lies between 1 kHz and 2 kHz. The estimated quality factor is about 500. The details of entire process is discussed in the last chapter.

4.3.1 Fabrication of the patterned disc

For the fabrication of a disc with circular periodic trenches, the technique of photolithography with a photomask is used. The photomask is 0.007" Fuji film with guaranteed minimum feature size of 10μm (Outputcity, Inc). Eight patterns with different geometric parameters are designed and printed on the same 6" × 6" film. Eight patterns are located upper side of the mask with negative polarity (data area is clear, field area is dark), and the same patterns are repeated on the lower side with positive polarity (field area is clear, data area is dark). Each pattern has a circular periodic structure. The outer diameter is less than 1 cm. One pattern is shown in Fig. 4.3 as example. The array of eight patterns on both polarities is shown in Fig. 4.4.

The following procedure of photolithography is performed in a cleanroom environment. A 1 cm × 1 cm silicon wafer is prepared. The wafer is rinsed using acetone, DI water and IPA. Photoresist S1813 is uniformly coated on the silicon wafer by spinning it at speed of 4000 rpm for 45 sec. Then, the wafer is baked at a temperature of 115 °C for 60 sec. Karl Suss Mask Aligner (Model MA-6) with resolution of 1 μm is employed to perform photolithography. The photomask is placed above the photoresist coated wafer with suit-

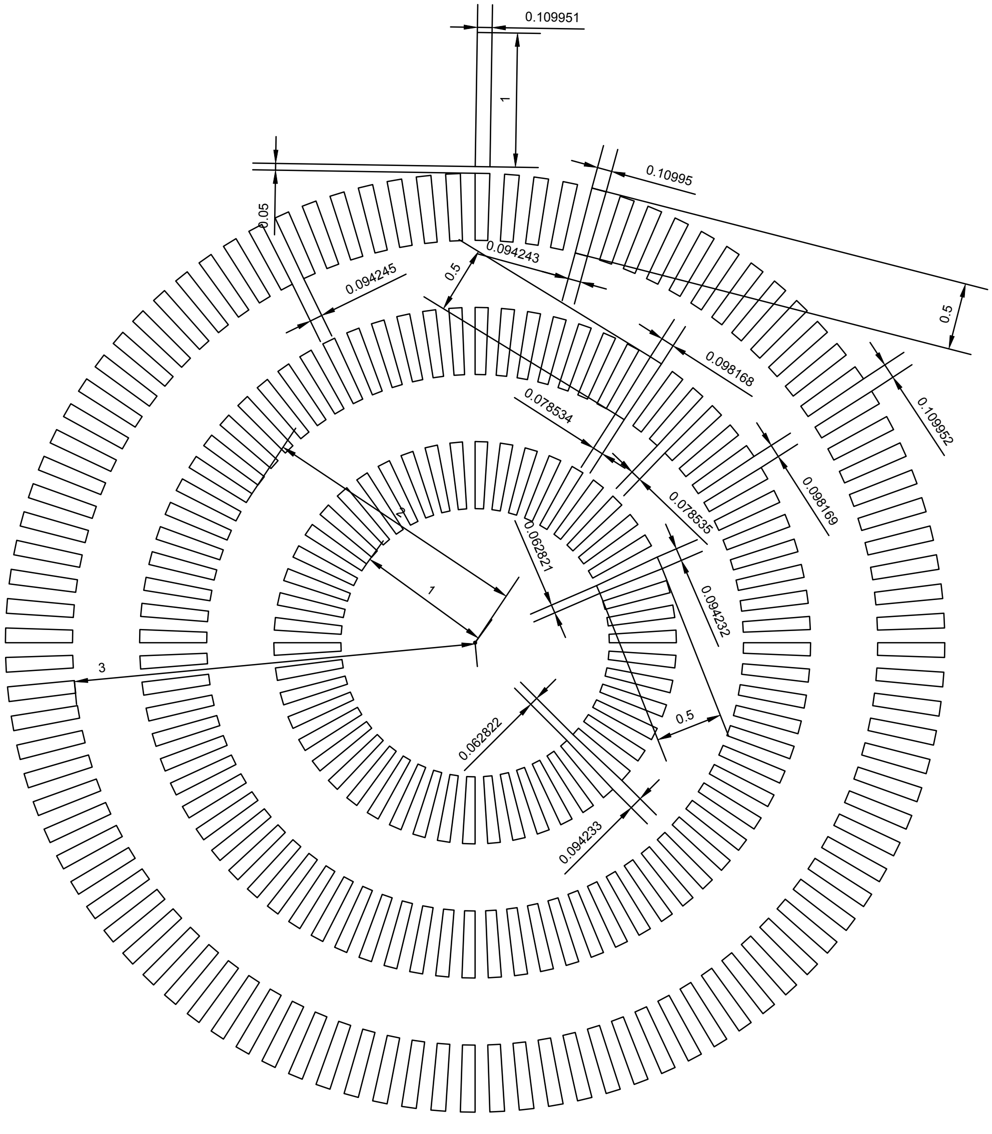

Figure 4.3: One sample pattern is shown here. The dimensions in mm are labelled in the figure. Three trench rings with different diameter have been designed. There are 90, 60 and 30 trenches on outer, middle and inner ring respectively. The outer diameter of the largest ring is 7 mm. The design of small diameters can reduce mechanical vibration caused by rotational wobble.

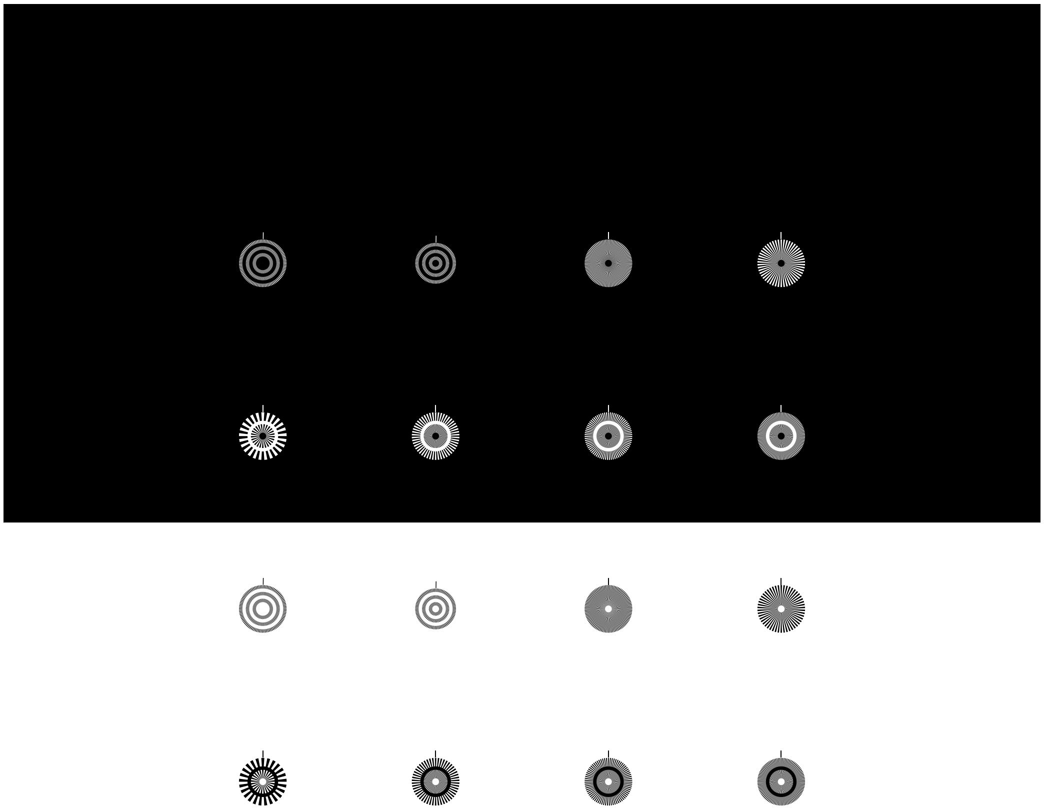

Figure 4.4: The eight different patterns are displayed in the top half side as negative polarity, and they are also repeated in the lower half side as positive polarity. The design of extra patterns gives more options to fabricate the disc.

able alignment. A negative polarity pattern is chosen while using S1813 (the pattern shown in Fig. 4.3). The contact mode is used here. Then, the aligner exposes the photoresist through the photomask with ultraviolet light. After 7.5 sec exposure, the wafer is rinsed using a developer solution (MF-319) for 60 sec. Exposed area of S1813 photoresist coating is removed. The wafer is then dried by compressed nitrogen gas.

The next step is to etch the silicon wafer with patterned photoresist coating to obtain trenches. The Silicon Trench Etch system (Oxford Cobra Plasmalab Model 100) is employed. An inductively coupled plasma (ICP) source delivers a high density of reactive species to the substrate in low pressure vacuum. The equipment is operated under chiller mode at temperature of 20 °C. The recipe that consists of SF_6 and C_4F_8 is used to etch silicon. At etching rate of 2.0 μm/min, etching process needs 85 steps in total corresponding to about 15 mins etching time. The exposed silicon without protection of photoresist is reacted with the plasma. After the wafer is taken out of the chamber, it is washed with acetone to remove all photoresist. A silicon wafer with patterned trenches is made. Next, the wafer is coated with 130 nm Au using E-beam evaporator. The depth of etched trenches is measured to be 60 μm using a profilometer (Veeco, Dektak 8). The fabricated wafer is ready to transfer into the experiment chamber.

4.3.2 Sphere-cantilever positioning system

The experimental setup inside the vacuum chamber is shown in Fig. 4.5. In vacuum, it can control the position of the cantilever. The sphere can be moved above the designated position of trenches, and also control the approach to the spinning disc.

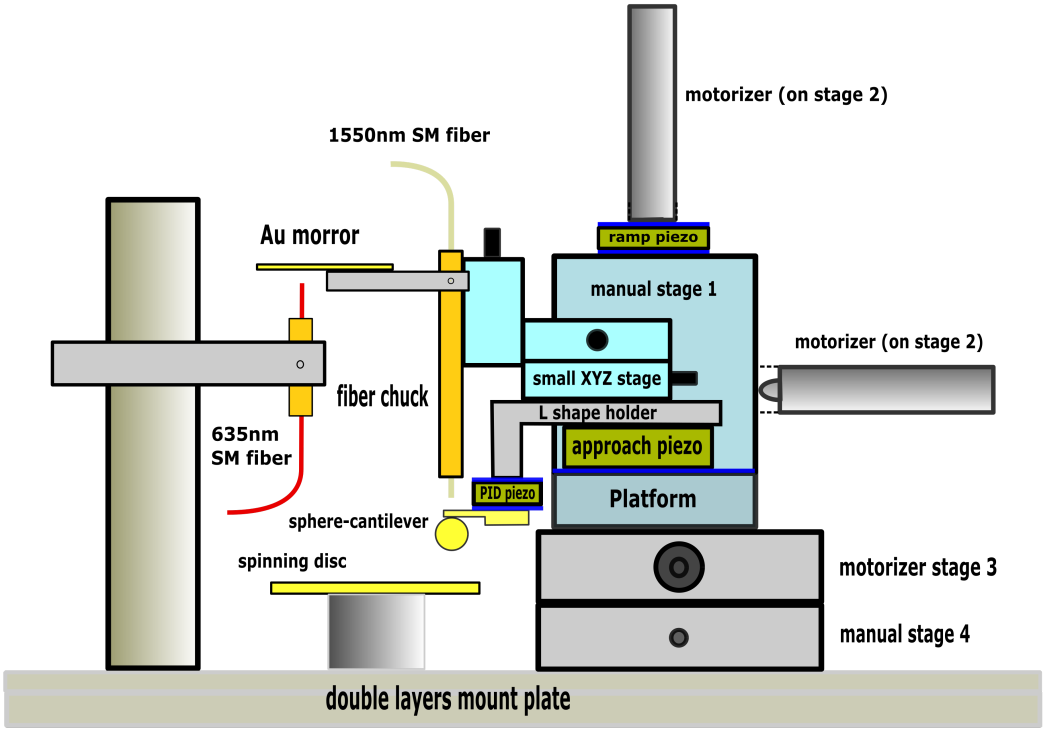

Figure 4.5: The setup to position the sphere attached cantilever in vacuum. The translation stage 2 and the triangle holder is hidden behind manual stage 1. The motorizer stage 3 and manual stage 4 are located below the platform.

The cantilever with sphere is glued to the bottom of a piece of copper plate of dimension 10 mm × 5 mm × 1 mm using conductive silver epoxy. The copper plate is connected to a function generator to apply voltage to the cantilever. The copper plate is attached to the bottom of a block PTZ piezo with a piece of glass plate inserted between them. The piezo block is designed to precisely control the position of the cantilever using PID feedback loop. This PID piezo block is covered by two pieces of glass plate of the same dimension of 5 mm × 3 mm × 1.5 mm for electric isolation. In this multilayers stack, the copper plate, the glass plate, the PID piezo block and the second glass plate are placed in sequence from bottom to top. They are mounted on top of each other using vacuum Torr

Seal. The stack is attached at the terminal of the vertical leg of a L-shape holder using Torr Seal. Above the horizontal part of the L-shape holder, a small 3-directional (XYZ) linear translation stage of dimensions 1”×1.25”×1.5” is mounted using a screw. A fiber chuck is fixed on the front face of the small XYZ stage using Torr Seal and a small bolt. A 1550 nm single mode fiber passes down the fiber chuck. The position of the fiber can be manipulated using the small XYZ stage. The end of the fiber points at the topside of the cantilever. The cantilever is suspended at the lowest point of the setup described above as shown in Fig. 4.5. In addition, an Au coated mirror is bounded to the fiber chuck for distance measurement (discussed later). Under the horizontal part of the L-shape holder, another piezo block of dimensions of 20 mm × 20 mm × 3 mm is placed. This bigger piezo block is used to assist the approach of cantilever-sphere to the disc. The components discussed above (the cantilever, the fiber chuck, the small XYZ stage, L-shape holder, etc.) are all supported by the approach piezo. The approach piezo is situated on an aluminum platform. The top surface of the platform is covered by a glass plate for isolating the approach piezo from aluminum. Besides supporting the L-shape cantilever holder, the aluminum platform is also attached to and controlled by a positioning system including 4 translation stages.

There are two sets of 2-directional and two sets of 1-directional linear translation stages. The one connected to the aluminum platform is labelled as stage 1. It is operated using 2 manually controlled screws in vertical and horizontal (left-right) directions. This stage is designed for manually manipulating the cantilever before pumping down. Stage 2 has the same translation directions as stage 1, but it is driven using two electric motorized stage (860A, Newport) instead of manual screws. When the motorized positioner is applied with a suitable voltage, it can drive the platform with everything mounted on it to move in vacuum. The operation of the motorized stage will be discussed later as part of the electronics system. These two stages are connected back-to-back using a metal connector. The front side of stage 1 is connected to the platform discussed in the last paragraph. The backside of stage 2 is attached to a triangle shaped aluminum holder of 4.5" height × 2.75" width × 2.75" length. Below the triangle holder, there are two 1 directional translation stages, labelled as stage 3 and 4. A manually controlled screw and a motorizer are equipped for stage 3 and stage 4, respectively. Two stages are positioned on top of each other, and horizontally transports other stages to move forward and backward together. All connections between the triangle holder, stage 3 and stage 4 use screws. To sum up, the stage system including four stages have 3 manual screws used before pumping down and 3 motorized positioners working in vacuum to serve all movement in the XYZ directions.

Previously, an Au coated mirror is mentioned. The mirror is directly connected to the fiber chuck so that the Au mirror, fiber chuck, 1550 nm SM fiber and the cantilever move together. Using PID feedback loop, the gap between 1550 nm fiber end and the cantilever is maintained fixed: the Q-point corresponding to maximum signal. Thus, the distance that the cantilever-sphere travels is precisely the same as Au mirror movement. The position of the Au mirror is monitored by a 635 nm fiber interferometer. The 635 nm fiber is held by another fiber chuck-holder system depicted on the left side of Fig. 4.5. The fiber is designed to monitor the bottom side of the Au mirror because of convenience of operation (The Au mirror faces down). Controlling the cavity length between 635 nm fiber end and Au mirror can be performed using a screw installed on top of the holder.

The whole arrangement above is mounted on an aluminum optical breadboard (Thorlabs, Inc). The coating of the plate is not vacuum compatible. It is removed by rinsing it in hot KOH solution, then sonicating it in dilute sulfuric acid. The breadboard is bolted onto a heavy stainless steel plate with the same dimensions of 12” × 12” × 0.5”. The increase in mass improves the stability of the entire setup against mechanical noise from environment.

4.3.3 Vacuum system and spindle installation

The measurement setup is placed in a vacuum bell jar (PYREX, 6886). The volume of the bell jar is 49.2 liters. The bell jar is placed on a flat stainless base plate. An elastomer gasket with L-shaped cross section is used to fill the gap between bottom of bell jar and the base plate. Silicone vacuum grease (Dow Corning) is applied to the gasket as sealant. The vacuum system is shown as in Fig. 4.6. The base plate has two open holes, one for all feedthroughs and pumping pipeline, the other for the spindle. The chamber is equipped with the following feedthroughs and devices:

- An Ion gauge (MDC gauge, SRS IGC 100 controller) for pressure measurement.
- a 25 pin ribbon cable feedthrough for all electronic wires.
- A 1550 SM fiber feedthrough for the interferometer monitoring cantilever. To build the feedthrough, a hole of diameter 1 mm is opened at the center of 2.75” CF flange. The plastic jacket inside the hole of is removed before the fiber is inserted through it. The hole with the fiber passing through is filled with vacuum epoxy resin (Torr Seal).

- A 635 SM fiber feedthrough for interferometer monitoring the Au mirror. The method building it is the same as the steps described above for the 1550nm interferometer.

The pumping pipeline contains the items below connected using stainless steel vacuum hoses in the following sequence:

- A vacuum gate valve.
- A sand box as damping isolator placed ahead of pumps, with vacuum hose buried inside.
- A molecular turbo (V70, Varian).
- A scroll mechanic pump (SH100, Varian) with a thermal gauge (DST531, Duniway Stockroom Corp.).

A typical operation of the pumping process is given here. After one week of pumping down, the pressure of the chamber can be stabilized at 10^{-6} torr.

1. Open the valve, turn on the scroll pump for 1 hour.
2. After the pressure reading of the thermal gauge is below 100 mTorr, turn on the turbo pump for a few hours.
3. Turn on ion gauge. The reading will be stabilized in 20 mins.

The air bearing spindle is obtained from KLA tencor, Inc. It uses 90 psi nitrogen gas as non contact bearing instead of traditional steel balls bearing. The 6 cm diameter spindle rotor on the top floats about 7 μm when it spins. The gas bearing achieves a non-repeatable run-out at nanometers level due to absence of friction. The rotor is driven by an AC motor controlled by a MCS controller (LA2000). The communication between the controller and computer uses a RS232 serial 9-pin null modem Cable. The software is used to control the spindle rotation speeds and direction. The challenge is how to rotate a disc in vacuum with an air bearing spindle. Some special design processes have been developed to accomplish this.

Here, we introduce the mounting structure of the installed air bearing spindle. Shown as in Fig. 4.6, the spindle is installed using the left hole on the base plate. The hole is welded to a stainless steel tubing of 1.5” inner diameter and 4.7” length. The other side of the tube is a 2.75” CF flange. Because of the 5.5” flange on the spindle, a 2.75” CF flange to 5.5” spindle flange adapter is used. An O-ring with inner diameter of 5 inch and thickness of 1/8 inch is placed between the adapter and the spindle flange. The O-ring provides flexibility to position the spindle by tightening screws. The height of the adapter is 1.625”. An empty space of 3.25” diameter and 1.125” depth is designed to accommodate the floating rotor. A 15.6 cm long shaft with a 6 cm diameter mounting disc is used to extend the shaft. The mounting disc is fixed on the top of the spindle rotor using bolts. This O-ring of diameter 40 mm and 2 mm thickness is inserted between the mounting disc and the spindle rotor. It can allow us to adjust the height and perpendicularity of the shaft by tightening bolts to compress the elastic O-ting. The top of the shaft is connected to a 1.2 cm diameter skirt. A special structure is designed here to realize two functions: the skirt can be rotated, while the vacuum is maintained. The vacuum seal consists of the following parts:

- The skirt at the top in vacuum. The skirt has a circular ridge with diameter of 11

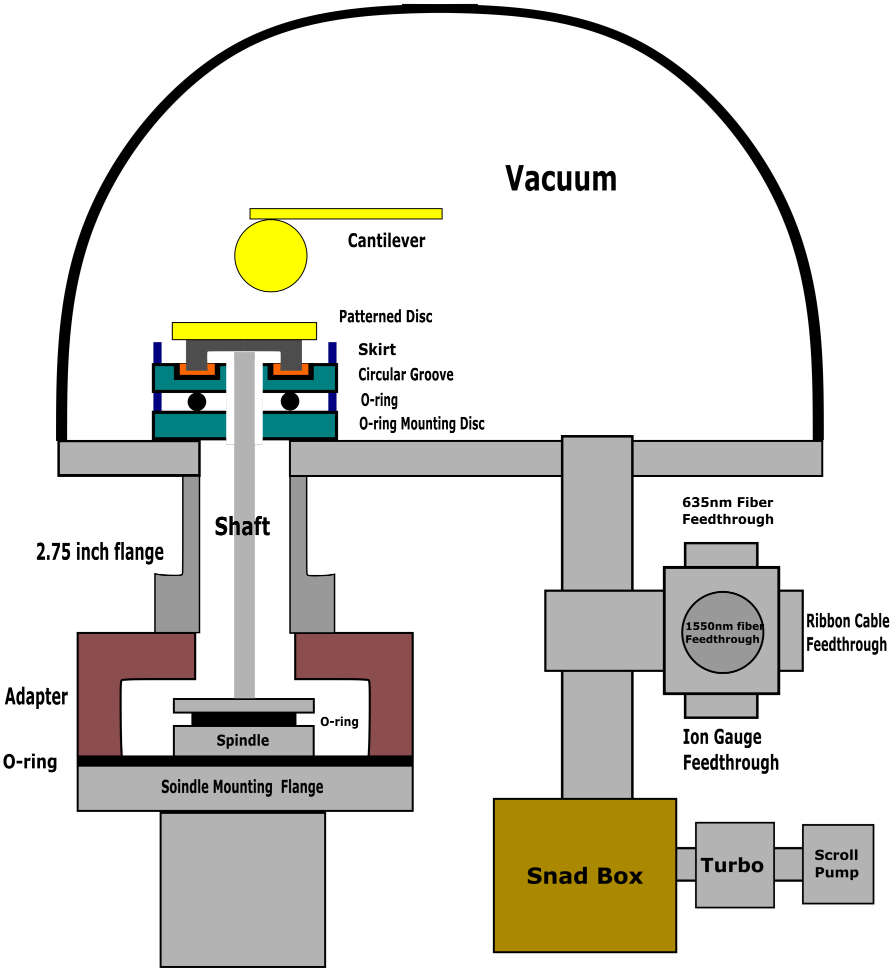

Figure 4.6: The vacuum system is equipped with an air bearing spindle. All feedthroughs are installed on a six way cross with 2.75" CF flanges. The sand box and two pumps are connected in series.

mm and thickness 0.5 mm on its bottom side. A bolt is used to attach the skirt to the top of shaft. The Torr Seal needs to cover the bolt after installation and alignments are done.

- A disc with a circular groove, a center hole and 4 through holes. The groove has diameter of 11 mm and depth of 0.2 mm. The hole has diameter of 7.4 mm at the center. The circular ridge on the skirt matches and inserts into the groove. Vacuum grease is applied inside the groove. The spindle shaft passes through the center hole. Four blots pass through the holes.
- A 9/16" inner diameter × 3/32 thickness O-ring.
- The lower disc with a 7.4 mm diameter center hole, 4 threaded holes, and O-ring groove carved on its top. Four screws are used to compress the O-ring by pushing down the above disc. The O-ring seal gives us flexibility to adjust the position of the groove matching the skirt, and also prevents air from entering the chamber. The diameter of this disc is 4.4 cm. It is large enough to block the hole on vacuum base plate. The edge of the disc is sealed by Torr Seal.

The above 4 parts are installed from top to bottom. The alignment needs to be done carefully using screws and O-rings. The skirt spins in the vacuum. The structure containing the grease filled circular groove and O-rings compressed by screws maintains a good vacuum. All position adjustment and alignment can be done using the flexibility given by O-rings placed in joints.

4.3.4 Optical interferometer system

Two optical fiber interferometers are used. The schematic is shown in Fig. 4.7.

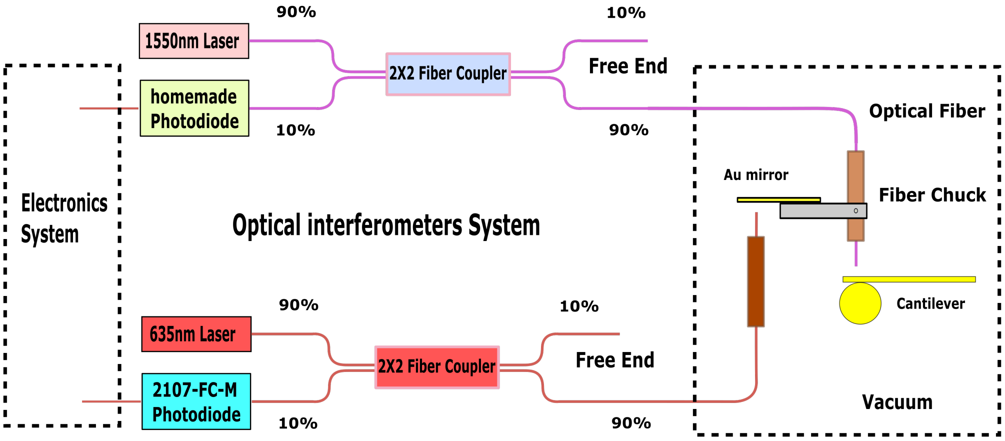

Figure 4.7: The 1550 nm fiber interferometer is used to monitor oscillation of the cantilever. The 635 nm fiber interferometer is used to monitor the movement of the Au mirror.

One interferometer is used to measure the cantilever oscillation amplitude at high resolution. The silicon cantilever has very little absorption at infrared wavelength. To avoid heating the cantilever, a diode laser source with emission wavelength of 1550 nm is used (Laser Diode: LD-56567, Diode Mount: ILX Lightwave LDM4980, Controller: ILX Lightwave LDC-3724). The output power used is 0.5 mW. The output connector of the laser source is coupled to a 2 × 2 fused fiber coupler with a split ratio 90:10 (Thorlabs, Inc.). The 90% input fiber of the coupler is connected to the laser source. The 90% output fiber is connected to another 1550 nm single mode fiber (1550BHP, Thorlabs) using a FC/AFC connector. The additional fiber elongates the light travelling path to transmit into the chamber. The fiber feedthrough fabrication is discussed previously. The end of the fiber is cleaved and brought close to the cantilever. The position is controlled by a fiber chuck and a small XYZ translation stage described before. The cleaved end surface of the fiber and the topside of the cantilever form an optical cavity. The cavity length is about 50μm. The interference signal reflected from the cantilever transfers back to the fiber coupler. The 10% input fiber of the coupler is connected to a custom built photodiode receiver. The photodiode collects optical signal from the cantilever and converts it to an electric voltage. The principle of interferometry and the method of amplitude measurement will be discussed in the next section.

The second interferometer is designed to monitor movement of the cantilever. To measure a few micrometers travelling distance, a shorter wavelength of 635 nm is selected. This interferometer uses a pigtailed Fabry-Perot benchtop laser (S1FC635, Thorlabs) as the light source. The laser has output power of 0.1 mW. The 2×2 coupler and the fiber connections are similar to that of the first interferometer discussed above. The 90% output fiber of the coupler is extended using an additional single mode fiber (SM600, Thorlabs). The signal is received by a photodiode (2107-FC-M, Newport Co.).

4.3.5 Electronics system and software system

In this section, the electronics system and software system used are discussed. The block diagram of electronic equipment is shown as Fig. 4.8.

As discussed previously, the separation between the cantilever and cleaved 1550 nm fiber end should be positioned at the Q-point, which is the midpoint between interference maximum and minimum. At the Q-point, the signal is maximized to obtain the best sensitivity. To maintain the Q-point position, a proportional-integral-derivative (PID)

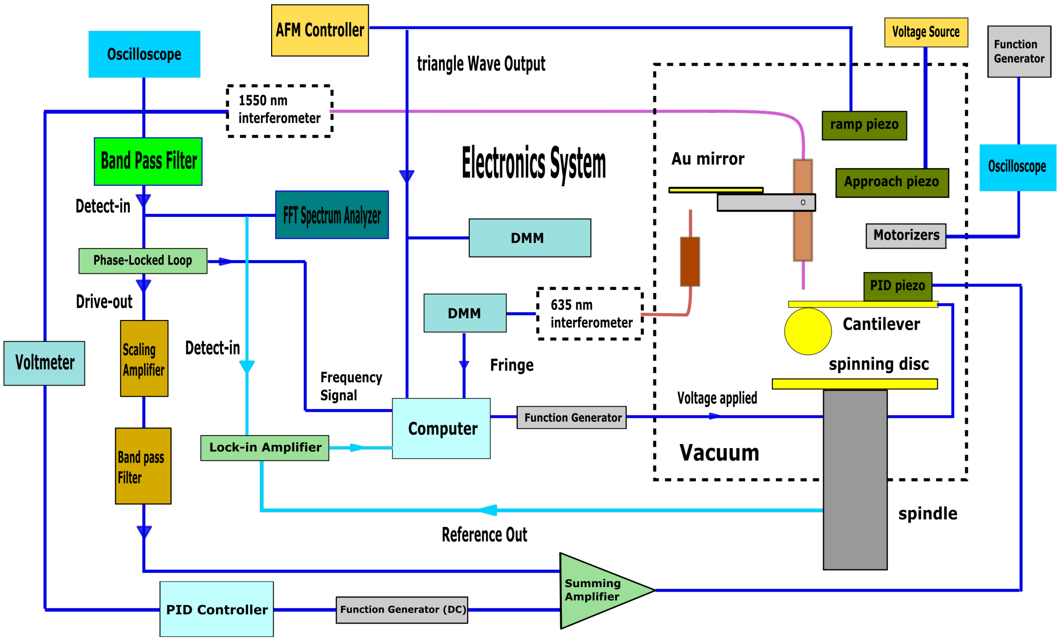

Figure 4.8: The block diagram of electronic apparatuses. Two interferometers shrink as two blocks here.

feedback loop is used to control the gap between the cantilever and the fiber end. To achieve this, a high resolution voltmeter (34420A, 7-1/2 digit nano voltmeter, Agilent) measures the voltage signal from the photodiode of 1550 nm interferometer. A function generator (33120A, Agilent) applies voltage to the PID piezo block attached above the cantilever. The range provided by the function generator is only from -10 V to +10 V. For the PID, a high voltage operational amplifier is used (APEX-PA341DW). A voltage source (HP6205C) supplies voltages from -50 V to +50 V. The amplifier has 2 inputs. One input linearly amplifies a DC signal with a gain of 4.6. The other input amplifies an AC signal with gain of 1.0. The gains are determined with resistors in the electric box. The output is the summation of amplified DC and AC signal. The PID voltage signal from function generator goes in as the DC input. After amplification, the DC component of the output has voltage range from

-46 V to + 46 V (The AC signal will be discussed later). Considering the piezo constant is about 15 nm/V, the PID piezo block can move more than 1.3 μm with the voltage applied. The voltmeter and function generator are controlled by a computer via GPIB bus lines. A Labview program controls the voltage applied to the PID piezo to maintain the voltmeter signal from interferometer as a constant position corresponding to the Q-point. To locate the Q-point, a triangle waveform with peak-peak amplitude of 90 V and frequency of 0.1 Hz is applied to the PID piezo. One can observe the interference sinusoidal signal to locate the Q-point using the second Labview software program. Then, the signal corresponding to Q-point is acquired. The signal value is taken as the setpoint for the PID loop. The PID feedback loop needs to be turned on immediately after the Q-point is located in case of any drift of the Q-point.

To exam the consistency with the previous technique, a frequency shift module is also used. The phase-locked loop (Nanosurf EasyPLL Plus) is used. The PLL can keep track of the change in resonate frequency of the cantilever due to the interaction force by maintaining a phase difference between drive-out signal and detect-in signal at 90°. The drive-out signal voltage is applied to the PID piezo to oscillate the cantilever using the summing amplifier discussed above. The drive-out signal with 10-20 mv peak-peak amplitude goes into the AC input of the amplifier. So the summing amplifier output consists of both DC component from the PID controlled function generator and AC component from the PLL drive-out signal. To obtained low noise driving signal with suitable amplitude, the AC drive-out signal passes through scaling amplifier (SIM983, SRS), analog high pass filter (SIM965, SRS) and analog low pass filter (SIM965, SRS) before going into the summing amplifier. These devices are embedded in a modular mainframe (SIM900, SRS). The detect-in signal received from the photodiode of 1550 nm interferometer needs a preliminary filter. A band pass filter (SR650, SRS) is installed to amplify the photodiode signal and reduce its noise before sending it to the PLL detect-in port. In addition, after passing through the band pass filter, the interferometer signal is also received by a FFT spectrum analyzer (SR760, SRS). the thermal peak of the cantilever is monitored on its display.

In the amplitude detection method, a lock-in amplifier (SR830, SRS) will replace the Phase-locked loop (PLL). Instead of applying AC drive-out signal to the PID piezo using the summing amplifier, the drive is provided by the spinning patterned wafer. The Lock-in amplifier measures the amplitude of 1550 nm interferometer signal with an external reference from the spindle controller.

The coarse approach in vacuum is performed using three motorized positioners. Motorized positioners are powered by a function generator (33220A, Agilent). There are two modes to control the motorized positioners: DC voltage mode and pulse wave mode. When a DC voltage higher than 3.5 V is applied to a motorizer, it drives the stage to move continuously. A higher voltage corresponds to a faster moving speed. The direction of movement is determined by the sign of the voltage. But one hardly controls the precise position by applying a constant voltage. To easily control the motorized positioner, especially when the sphere approaches to the disc, a pulse wave voltage can drive a motorizer to work as a step motor. If a pulse wave of amplitude of 4 V and width of 50 msec is applied to the motorized positioner, a motorized positioner has a maximum range of 1-2 μm (Tested using the vertical direction motorizer on stage 2). The following parameters are typically used:

Frequency = 100 mHz, High Level = 0V, Low Level = -4V, Width = 9.950 Sec, Edge = 5.0 ns. The waveform is observed in an oscilloscope (Tektronix, TDS430A) to avoid wrong voltage output. This method is used to control cantilever position for the coarse approach before measurements in vacuum. The movement of the sphere can be observed using a telescope camera (Electrophysics, WAT-902) and a color video monitor (Panasonic, 1995).

The fine approach is done using a piezo block: the approach piezo is located below L-shape cantilever holder. This piezo is not suitable for controlling the movement of cantilever while taking force measurement. Some preliminary tests show its non-uniform expansion causes rotational motion besides vertical translation motion. Furthermore, additional mechanic strain causes the deformation of the L-shape cantilever holder leading to unwanted position change of the cantilever. But this piezo block gives the option to do a precise approach before force measurement. One can apply voltage in the range of 0-100 V to the approach piezo using a voltage source (228A, Keithley). Large voltages near 100 V is applied to lift the cantilever up before performing the coarse approach. After the motorizer brings the sphere to a reasonably close position, one can continue to lower the sphere by manually reducing the voltage slowly.

To avoid the problems of the approach piezo discussed above, the ramp piezo is installed below the vertical manual screw of the translation stage 1, and covered by glass plates on its top and bottom for electric isolation. This piezo block is used to move the cantilever up and down periodically with a frequency of 0.01 Hz while measuring the force as a function of distance. The AFM controller (Nanoscope V) with signal access module (Digital Instrument) provides the high voltage outputs. Following instruction from the manufacture, the working voltage of the piezo used has a limited range of 0-150 V. To protect the piezo from large applied voltages, the voltage signal is displayed on a DMM (HP3455A). In addition, the applied voltage is also recorded using another DMM (34401A, Agilent) during experiments. This DMM also uses GPIB bus line to send data to the computer for analysis. For all devices using GPIB bus lines, their GPIB lines are connected to the same GPIB-USB-HS interface adapter communicating with the computer.

While the ramp piezo is working during measurement, the sphere attached cantilever moves along with the Au mirror bound to the fiber chuck. The movement is monitored using the 635 nm interferometer. The signal from the photodiode of this interferometer are interference sinusoidal fringes which are used for distance measurement. It is recorded by a DMM (34410A, Agilent). The DMM transfers its digital signal to computer via an USB cable.

The voltage applied to the sphere is provided by a function generator (33220A, Agilent). The computer sends commends to control the applied voltage via an USB cable.

The main Labview program is in charge of the force measurement experiments. It has the following functions: (1) Read data from the Lock-in amplifier (SR830, SRS) to record the amplitude signal from the cantilever. (2) Read ramp voltage from the DMM (34401A, Agilent). The ramp voltage is supplied by the AFM controller and applied to the ramp piezo. (3) Read interference fringe signal from the DMMs (34410A, Agilent). The signals obtained from these two DMM are used for the distance calibration. (4) Control the function generator (33220A, Agilent) to apply specific voltages to the sphere. The first three read-in functions are three sub-programs placed in one while loop. So reading of all three signals executes at the same time. The sampling rate is determined by either the device with the longest integration time or the setting of a ”Delay Timer” in Labview. The voltage output is triggered by reading ramp voltage. 21 voltages are applied to the sphere during one loop.

Finally, a 12 BNC ports to 25 pin ribbon cable adapter is built to establish communication between devices inside the chamber and the electronic equipment system outside. The BNC ports are assigned as the following: three channels for motorizers in all XYZ directions, one PID piezo voltage channel, one approach piezo voltage channel, one ramp piezo voltage channel and one channel for the voltage applied to the sphere. Additional ports give more options for future upgrade. All channels connect their grounds to the shell of the metal box. All electronic signals are conveyed into the chamber through a 25 pins ribbon cable. A feedthrough installed on a flange serves to connect between wires in the vacuum and the outside ribbon cable.

To sum up, the above electronics system with Labview software fulfills all required functions including motorizer controlled coarse approach, piezo controlled fine approach, observation of approach, Q-point control, reading and sending signals, voltage supply, and signal amplification, etc.

4.4 Amplitude measurement technique using test samples

A technique based on fiber interferometry has been developed to measure subpicometer oscillation amplitudes [40, 41, 42, 43, 44, 45, 46, 47, 48, 49, 50, 51, 52, 53, 54, 55]. We applied this technique to measure the piezoelectric constants of bio-samples from inter-molt dactyl clubs obtained from the mantis shrimp [56, 57, 58]. The same technique is applied to measurement of cantilever oscillation amplitude as well. The application shown here is a demonstration of the amplitude measurement sensitivity. The force sensitivity can be estimated from the amplitude sensitivity, spring constant of the cantilever and its quality factor Q. This non-contact technique can measure displacements better than 0.5 picometer for piezoelectric samples subjected to large electric fields. The piezoelectric constants of the bio-samples were calculated from the optical interference fringes and determined to be about 0.4 pm/V.

4.4.1 Interferometer setup

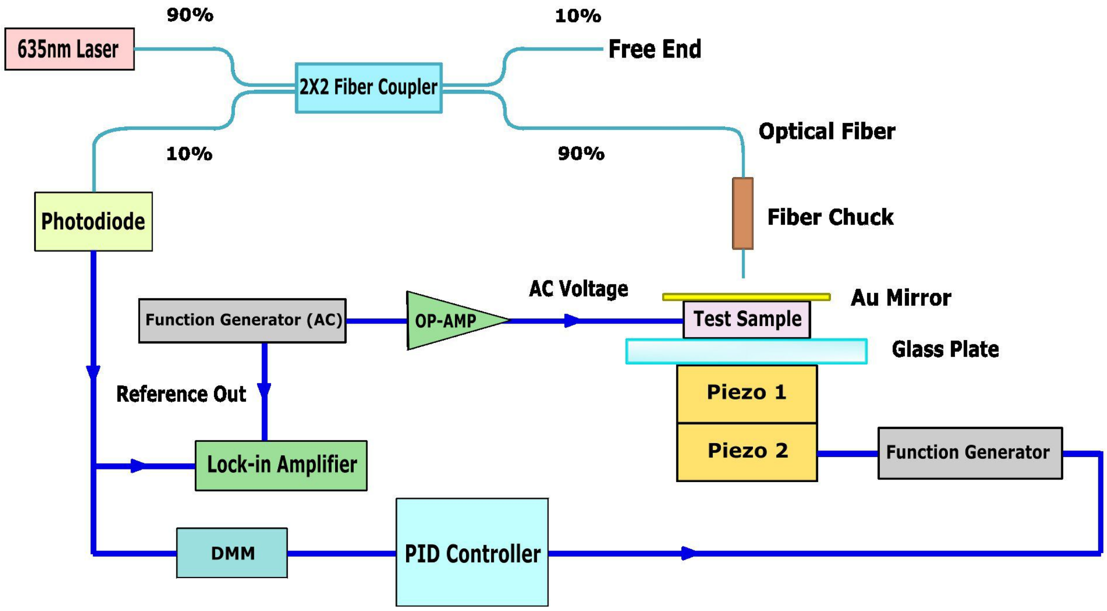

Figure 4.9: Schematic of the optical interferometer technique developed for the measurement of the very small piezoelectric strains. The specific components are labeled in the figure. Piezo 1 is used only for calibration purposes. Piezo 2 is used to maintain the cavity length at the Q-point.

Towards the goal of measuring picometer displacements necessary for investigating the piezoelectric coefficients of small and thin biological samples, a fiber optical based interferometer was developed. The measurement principle is based on optical interferometry. A schematic of the experimental setup is shown in Fig. 4.9. A pigtailed Fabry-Perot Benchtop Laser Source (S1FC635, Thorlabs, Inc., USA) with an emission wavelength of 635 nm and output power of 0.05 mW was used as the light source. The output of the laser source was coupled to a single mode 2 × 2 fused fiber optic coupler with a split ratio 90:10 (Thorlabs, Inc., USA). The 90 percent end of the output fiber was cleaved to expose a clean perpendicular face. This forms one end of the interferometer cavity as shown in Fig. 4.10. The second surface of the Fabry-Perot interferometer is an Au coated silicon plate. The Au coating was made on the polished side of a 1 cm × 1 cm silicon wafer of 500 μm thickness. The cleaved end of the optical fiber and the Au mirror formed the two surfaces of a low finesse optical cavity. The biological sample to be investigated was attached to the bottom of the silicon plate using epoxy and its preparation is described later. The output light of the interferometer was collected and transmitted through the same fiber and was detected by a photodiode (2107-FC-M, Newport Co., USA) as shown in Fig. 4.9. This output light of the interferometer at the photodiode can be expressed as:

$$I_{out} = (\vec{E_1} + \vec{E_2})^* \cdot (\vec{E_1} + \vec{E_2}) \tag{4.15}$$

where $\vec{E_1}$ and $\vec{E_2}$ represent electric fields of reflected beams from the cleaved fiber end and the Au mirror respectively. This can be rewritten in terms of the corresponding light intensities involved and the cavity length d as:

$$I_{out} = I_{effective}[1 + V \cos\left(\frac{4\pi n d}{\lambda}\right)] \tag{4.16}$$

where $I_{effective} = I_{input}(R_1 + \alpha(d)R_2)$ and the visibility $V = 2\sqrt{R_1 R_2 \alpha(d)}/(R_1 + \alpha(d)R_2)$. Here I_{input} is the input intensity into the cleaved end of the fiber, R_1, R_2 are power reflection coefficients of the cleaved fiber end and the Au mirror, $\alpha(d)$ is the attenuation coefficient of the optical intensity due to the divergence of the light beam from the fiber, n is index of refraction of air, and $\lambda =$ 635 nm is the wavelength of the red laser. $I_{effective}$ and visibility V can be considered independent of d when the changes in the interferometer cavity length are small.

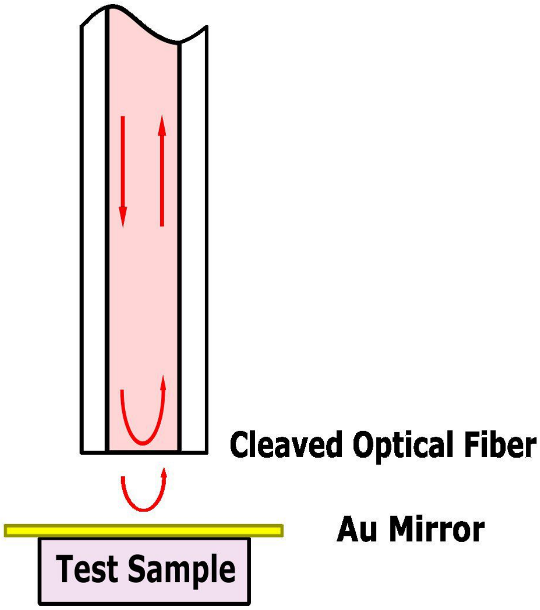

Figure 4.10: Schematic of the optical cavity formed by the cleaved end of fiber and the Au coated silicon plate (mirror). The paths of the light beams are shown with arrows.

A polished biological sample of size 5 mm × 3 mm and thickness 0.5 mm was used. To facilitate the application of voltages to the biological sample, the top and bottom surfaces were made conductive with Ag epoxy (MG chemicals, USA). This prepared sample was then attached to the bottom of the Au coated silicon mirror as shown in Fig. 4.9.

To allow for control and modulation of the interferometer cavity length, a special arrangement of two Lead Zirconate Titanate (PZT) piezo blocks (Thorlabs, Inc., USA) of size 0.3 cm × 0.3 cm × 0.2 cm were used. In order to electrically isolate the sample from the piezo blocks beneath, a glass plate with 1 mm thickness was inserted between them. The two piezo blocks were mounted below the glass plate as shown in Fig. 4.9. A non-conductive cyanoacrylate epoxy was used to attach the glass plate as well as the piezo blocks. The whole experimental setup was built on an optical table to provide the necessary isolation from mechanical vibrations.

4.4.2 Measurement procedure and results

As a demonstration of the instrument development, a report of the piezoelectric coefficient d_{33} of a biological sample is presented below. The test samples used were prepared as described above from fresh inter-molt dactyl clubs obtained from mantis shrimps. The biological sample piezoelectric coefficient was determined by comparing to the independently calibrated PZT piezo 1. First the interferometer signal was optimized by bringing the optical fiber within 20 μm of the Au mirror using a linear translation stage. The calibration of piezo 1 was completed as follows. A 0.1 Hz triangular wave with an amplitude of 10 V was applied to piezo 1. This applied voltage value was sufficient to generate more than 300 nm displacement of the Au mirror. The interferogram shown in Fig. 4.11 was generated using the triangular wave. The peaks correspond to constructive interference maxima and the valleys to destructive interference minima. The interference output is sinusoidal due to the low finesse of the cavity which in turn results from the use of the cleaved end of the optical fiber as one surface. The interferogram is fit to Eq. 4.16 using $d = \alpha V$ where α is the expansion coefficient and V is the voltage applied to the piezo 1. The mean value found for the α of piezo 1 from the fit was 19.2 nm/V.

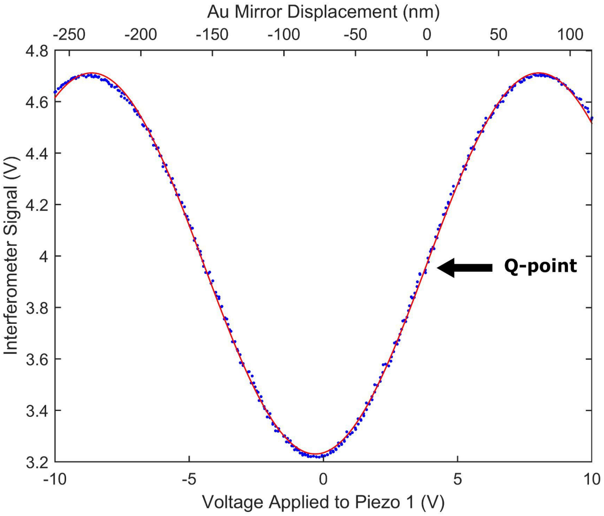

Figure 4.11: The interferometer output signal is a sinusoidal function of the distance moved by the Au mirror using piezo 1. The red solid line is the best fit with equation of I_{out} using $d = \alpha V$ to determine the expansion coefficient α of piezo 1. This α is used to get the displacement of piezo 1 shown in the top axis. The signal has linear response at the Q-point as shown in the figure.

To maximize the sensitivity of the interferometer to very small changes in the cavity length, the Au mirror needs to be positioned such that the cavity length corresponds to the midpoint between an interference maxima and minima, hereafter referred to as the Q-point. In the experimental setup in Fig. 4.9, piezo 2 is used to maintain the cavity length at the Q-point using applied voltages. To find the Q-point, a 0.1 Hz triangular voltage waveform with an amplitude of 10 V was applied to piezo 2. An interference pattern similar to Fig. 4.11 was generated. The piezo 2 position and applied voltage corresponding to the Q-point can be identified. Once the Q-point was located, the corresponding DC voltage was applied to piezo 2 to bring the optical cavity to the appropriate length. A

PID (proportional-integral-derivative) feedback system with a response frequency of 1 Hz was used on the piezo 2 voltage to keep the cavity length at the Q-point. The use of the PID feedback compensated any effects of mechanical drift in the components that form the optical cavity. Around the Q-point, the output intensity I_{out} has a linear response to small change in the cavity length d.

The sensitivity was improved with phase sensitive detection using a lock-in amplifier. When sinusoidal oscillating voltages were applied to the biological sample, the associated oscillating piezo extension in turn leads to an oscillating optical cavity length d. The corresponding oscillation in the interference signal was detected by the photodiode and its output was measured using a lock-in amplifier. As the fiber-plate separation was maintained at the Q-point, the oscillating optical signal generated was linearly proportional to the mechanical vibration of the biological piezoelectric sample. The same signal generator applying the sinusoidal voltage signal to the biological sample was used as the reference for the lock-in amplifier. For the particular measurements of the piezoelectric coefficient d_{33} of the biological sample reported here, a sinusoidal voltage at 500 Hz and an amplitude of 35 V was first applied using a function generator. The amplitude of the function generator was amplified using an operational amplifier. Considering the extremely low piezoelectric coefficient of the biological sample, large voltages were necessary to get measurable signals. The output amplitude of the lock-in amplifier was recorded. The experiment was repeated 5 times and the average recorded lock-in amplitude is shown in Fig. 4.12 as a solid square. The error bar is too small to be displayed in the figure. The measurement was repeated for different voltage amplitudes of 70 V, 105 V, 130 V, 140 V and the average recorded values are shown in Fig. 4.12. To eliminate ambiguities from stray electrostatic fields interacting with the fiber and leading to its displacement, the voltage connections to the two electrodes were interchanged and the experiment repeated. There was no change in the response of the biological sample to this interchange.

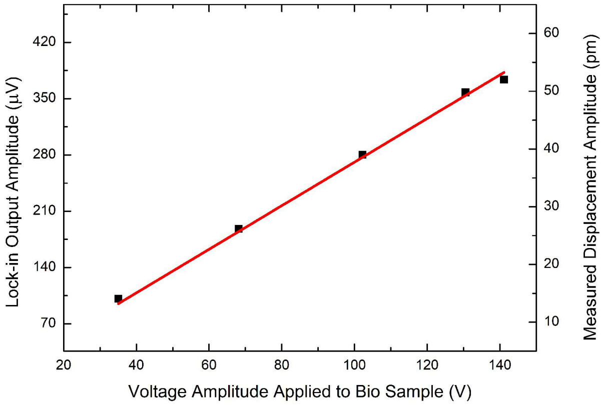

Figure 4.12: The lock-in amplitudes shown for the different voltage amplitudes applied to the biological piezoelectric sample. The data points are average of 5 measurements. The lock-in amplitude is converted to the corresponding displacement shown on the right axis using the calibrated piezo 1 data from the next figure below. The slope of the best fit line leads to the piezoelectric coefficient $d_{33} = 0.377$ pm/V at 500 Hz.

The output of the lock-in amplifier was calibrated using the earlier determined expansion coefficient α of piezo 1 using the interferometer. Here, the biological sample surfaces were electrically grounded. The cavity length was maintained at the same Q-point as before. Next, sinusoidal voltages with the frequency of 500 Hz and an amplitude of 4 mV was applied to piezo 1 using the same function generator. The amplitude output signal of the lock-in amplifier was recorded. Again, 5 measurements were taken and the average value is shown in Fig. 4.13 as a solid square. The measurements were repeated with 500 Hz signals of 6.0 mV, 8.0 mV, 10.0 mV applied to piezo 1. The recorded lock-in average amplitude values are shown in Fig. 4.13 for these applied voltage amplitudes. The error bars are also too small to be displayed in the figure. Using the interferometer calibrated piezoelectric coefficient of 19.2 nm/V determined earlier, the voltage value in the bottom axis can be converted to the corresponding expansion of the piezo 1 which is shown along the top axis in Fig. 4.13. A best fit straight line is fit to the data and the lock-in output signal per unit expansion of piezo 1 is determined to be 7.19 ± 0.03 mV/nm.

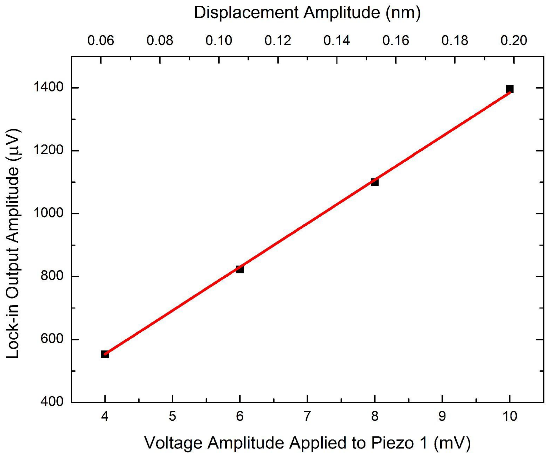

Figure 4.13: Calibration of the lock-in amplitude output using the calibrated expansion of piezo 1. The measured lock-in amplitudes for the various sinusoidal voltage amplitudes applied to piezo 1 are shown as solid squares. The top axis is the corresponding expansion amplitude obtained from the calibrated α of piezo 1. This measurement was taken at a frequency of 500 Hz.

The above calibrated value of the lock-in output amplitude can be used with that found in Fig. 4.12 to get the piezoelectric strain oscillation of the biological sample to the applied voltages. The value of the lock-in output in the left axis of Fig. 4.12 is converted to an expansion in nanometer using the above calibration and is shown on the right axis of Fig. 4.12. The slope of the best fit line is the d_{33} piezoelectric coefficient of the biological sample and is found to be 377 ± 4 fm/V. The experiments were repeated for different sinusoidal frequencies of 1.0 kHz, 1.5 kHz and 2.0 kHz. The corresponding piezoelectric coefficients obtained for the biological sample are shown in table 1. The experiment was repeated using a second biological sample prepared using the same procedure.

Frequency (kHz)	Bio-Sample 1 (pm/V)	Bio-Sample 2 (pm/V)	Glass (pm/V)
0.5	0.337	0.468	0.039
1.0	0.401	0.329	0.025
1.5	0.439	0.299	0.045
2.0	0.408	0.356	0.024

Table 4.1: Piezoelectric coefficients of the biological samples. Column 1 has the frequencies of the applied voltages; column 2 and 3 are piezoelectric coefficients of the two biological samples measured. Column 4 reports the values for glass which is a non-piezoelectric material and is thus a measure of the background noise in the setup.

To estimate the background noise additional tests were performed. The biological piezoelectric sample was replaced by a glass sample of similar thickness and the noise background of the setup was measured. For this, a 1 × 1 cm piece of polished silicate glass was used. Since glass is centrosymmetric, it has zero piezoelectric response. It does have a second order size change under an applied electric field due to electrostriction, which is extremely small and of the order of 10-20 nm/V^2 [59]. Thus, any measured displacement signal on application of the voltage to the glass plate is the background noise. Fig. 4.14 is a demonstration of the background noise signal measured as a function of the amplitude of the applied voltage. This observed background noise signal is probably due to thermally induced mechanical strains in the electrodes from the current flow during to the application of voltages. From the error bars in Fig. 4.14, the displacement sensitivity of the interferometer is shown to be 0.5 picometer for the frequencies used. The bandwidth used in all measurements is 530 Hz from the time constant setting of the lock-in amplifier used. Based on the noise level of the interferometer setup is 20 fm/Hz$^{0.5}$.

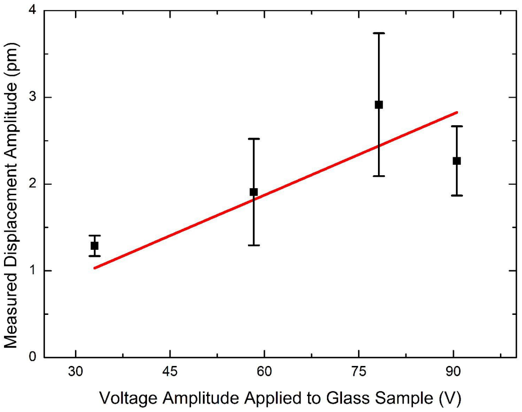

Figure 4.14: Displacement amplitude of the glass sample plotted as a function of the applied voltage at 500 Hz.

4.4.3 Summary for measurements using test samples

An optical interferometric system using phase sensitive detection was developed that can enable the non-contact measurement of very small piezoelectric strains in small samples. The experimental platform is versatile and can be used for measuring the piezoelectric coefficients of very thin samples with weak piezoelectric responses under large electric fields. We used the experimental setup to measure the piezoelectric coefficients of small and thin biological samples from the dactyl clubs of mantis shrimps. The noise and displacement sensitivity of the interferometer is shown to be 20 fm/Hz$^{0.5}$ and 0.5 picometer respectively. A non-piezoelectric material such as glass was used to measure the background noise in the system. The technique developed is simple and robust and will find other uses in non-invasive measurements of micro actuators and miniature or thin film piezoelectric samples as it exhibits high sensitivity and displacement resolution over a wide range of frequency.

4.4.4 Force sensitivity for measurement using cantilever

In Casimir force measurement, the gap between the topside of the cantilever and the end of 1550 nm fiber is maintained at the Q-point. The same Lock-in amplifier is used to detect the oscillation signal from the cantilever. The signal in voltage will be converted into mechanic amplitude.

Using the amplitude resolution of A_{min}=0.5 pm given by the experiment introduced above, one can roughly estimate the force sensitivity. If the mechanic noise background is ignored (assuming that the spindle is rotated at much lower frequency than the cantilever resonant frequency), the minimum detectable force is given by $F_{min} \approx A_{min} * k/Q$ based on Eq. 4.13 if measuring the fundamental harmonic n=1. We assume the spring constant of an etched cantilever $k = 0.01$ N/m, its quality factor $Q = 500$. Therefore $F_{min} \approx 10^{-17}$ N. This force sensitivity is high enough to observe thermal Casimir force at larger separation distance.

Chapter 5

Chapter 5 A generalized Casimir force: Entropic force induced by fluctuation of polymers between scale-free boundaries [1]

The well known QED Casimir force originates from quantum fluctuation of the electromagnetic waves confined between two parallel plates. It can be attractive or repulsive depending on boundary geometry. [60] The concept of fluctuation induced forces can be generalized to thermal fluctuation in other fields such as critical Casimir forces in colloidal suspensions [61], fluctuation induced thinning of superfluid films [62] and interac-

---

[1] This chapter contains materials published in: M. Liu, J. Xu, R. Zandi and U. Mohideen (2019). "Measurement of entropic force from polymers attached to a pyramidal tip." Journal of Physics: Condensed Matter 31(7): 075102.

tions between rods on membranes [63]. Analogous to the vacuum Casimir force, a boundary dependent entropic force from fluctuation of confined polymers between well defined boundaries is demonstrated here. Polymers attached to the apex of a pyramidal tip approach a flat plate. The confinement of polymers leads to a repulsive force. The measurement was performed in liquid using an AFM. The results were analyzed using two different theoretical models.

5.1 Motivation to study boundary dependent entropic force

The boundary shape dependence of the entropic force from polymers has been theoretically discussed [64, 65, 66]. In particular, the entropic force from the confinement of a single or a few polymers attached to a cone tip and a flat plate has been shown to be readily calculable and displays interesting boundary separation distance dependencies [64, 65]. For a single polymer attached to a conical tip and confined by a flat plate, the only relevant scale is the tip-plate separation distance h, for h less than the polymer radius of gyration R_g. One can then expect that the partition function of the system to have a scaling form: $Z(h) \sim (h/R_g)$ with an exponent that depends on the solvent condition. To calculate the force, the derivative of $Log|Z(h)|$ with respect to h needs to be done. This gives rise to an entropic force that goes inversely as h [64, 65]. On the other hand, if the tip radius is of finite size, then during compression by the plate the tethered polymer system might undergo escape transitions [67, 68, 69, 70, 71]. Here, for small compression polymers remain confined between the two surfaces, but with increasing force, some of the monomers escape from the confinement between the two surfaces leading to interesting transitions [72, 73, 74, 75, 76, 77, 78, 79, 80]. In the absence of boundary, the compression of polymers confined between two infinite flat plates has been well studied and is given by the Alexander-de Gennes theory [81, 82, 83, 84, 85]. Here, the polymer chains confined to a decreasing volume between the plates produce a monotonically increasing force.

Due to the sensitivity of the atomic force microscope (AFM), small forces induced by even a lone or a few polymers can be detected and measured [86, 87, 88, 89, 90, 91]. This makes the measurement of the entropic force resulting from the confinement of a single polymer feasible [92]. An experimental approach to measure the entropic force of polymers attached to the apex of pyramidal cone interacting with a flat plate was designed. A sharp pyramidal tip was chosen as one boundary and a hydrophobic flat plate as the second surface for confinement of polymers. A special technique was developed to attach a well-defined Au patch to the apex of the pyramidal tip AFM cantilever. This Au patch was then used for the specific local attachment of the polymers. This technique can be used to measure entropic force originating from the thermal fluctuation of polymers with piconewton force sensitivity using the AFM in a fluid environment. The measured force as a function of the distance between the pyramidal tip and a hydrophobic plate was compared to the above model of polymer-mediated entropic force between scale-free objects and the Alexander-de Gennes theory for a polymer brush.

5.2 Experimental setup and AFM cantilever fabrication

To study the boundary dependence of the entropic force from polymers confined between two surfaces, the polymers need to be attached to a unique well characterized shape.

The AFM used for the force measurement was the MultiMode Nanoscope IIIA, Bruker Corporation. It was placed on an optical table to reduce the effects of ambient mechanical noise. A pyramidal cone boundary was chosen as one surface and a flat hydrophobic plate as the second surface. A few polymers need to be attached to the apex of the pyramidal cone. In order to have a nanoscale pyramid as well as allow piconewton force sensing ability, a 210 μm rectangular silicon AFM cantilever with a pyramidal tip (MSNL-10 obtained from Bruker Corporation) was employed. The polymers used were thiolated Poly ethylene glycol (PEG-thiol) with molecular weight 20,000 Da and 40,000 Da (obtained from Sigma-Aldrich Co.). According to the manufacturer the index of polydispersity (M_w/M_n) of the PEG-thiol polymers used is less than 1.2. The thiolated polymers were attached to an Au patch at the apex of the pyramid. The gold patch with well-defined geometry was first affixed to the pyramid apex prior to the polymer attachment. Then, the polymers were specifically tethered to the Au patch at the pyramidal apex by thiol-Au bonds [93, 94, 95].

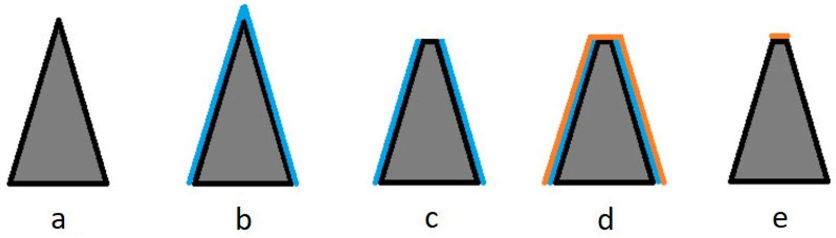

Figure 5.1: Technique to attach a Au patch to the apex of a pyramidal AFM tip. (a): A bare pyramidal AFM tip. (b): Coat 25 nm Al over the entire pyramid. (c): Abrade the apex on a sapphire surface using contact mode AFM. (d): Follow by coating 5 nm Cr and 20 nm Au on the tip. (e): Rinse the tip with 35% KOH solution to remove the bare Al on the sides of the pyramid leaving only the Au patch on apex.

The first step was the attachment of the Au patch to the apex of the pyramidal tip of the cantilever. The procedure for making the Au patch on the apex is shown schematically in Fig. 5.1. First, the cantilever was cleaned using a UV Ozone cleaner (spectrolinker XL-1500 obtained from Spectronics Corporation). Then, an e-beam evaporator was used to coat the pyramidal side of the cantilever with 25 nm of Al as shown in Fig. 5.1(b). Next, the Al coating at the apex of the pyramidal tip was removed by abrasion. For this the AFM was operated in contact imaging mode. A hard sapphire surface (Mohs hardness of 9) was used as the imaging surface. The continued scanning of the sapphire surface led to the abrasion of the Al. The extent of the abrasion on the pyramid apex was checked periodically using a scanning electron microscope (SEM). The Al layer on the top was abraded after 3-5 hours of scanning as schematically shown in Fig. 5.1(c). Following the abrasion, the entire tip was coated with 5 nm of Cr followed by 20 nm of Au as shown in Fig. 5.1(d). Here, Cr was used to promote the adhesion of Au to the exposed Si at the pyramidal apex. Next, the Al coating below the Au was selectively removed by wet chemical etching in 35% KOH solution. An etching time of 15 minutes was found sufficient to remove the Al. Mild agitation of the etching solution was helpful to enhance the etching rate. The etching of the Al also led to the removal of the Au layer over the Al, leaving only the Au over the pyramid apex as schematically shown in Fig. 5.1(e). After the etching, the cantilever was washed in water followed by acetone and ethanol. It was crucial to control the etching time as extended etching would lead to the removal of the Au patch on the pyramid apex. The Au patch on the apex of the pyramidal tip was inspected using the SEM, as shown in Fig. 5.2. The area of the Au patch was measured using the SEM to be $(3.7 \pm 0.5) \times 10^4\ nm^2$. The error of the size corresponds to the uncertainty in identifying the exact location of the edge of the Au patch. Note that the size of the Au patch can be controlling by varying abrasion time. The above technique can be used to reproducibly attach Au patches to the tip with a 20%-30% probability.

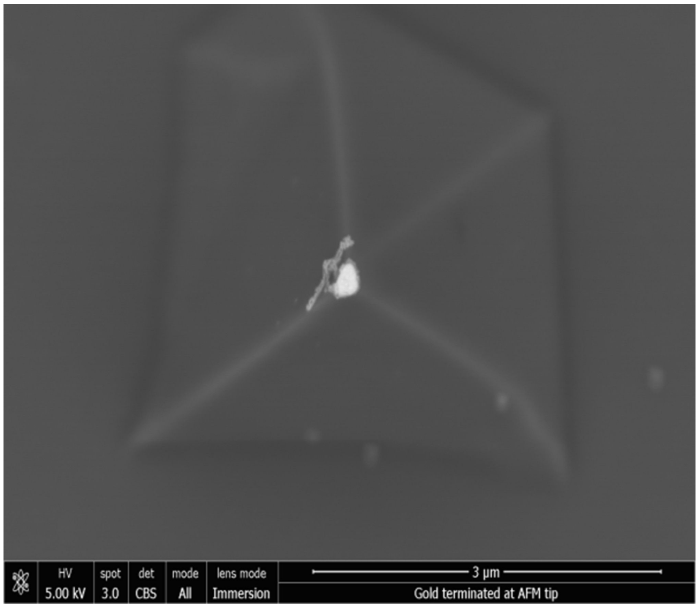

Figure 5.2: SEM of the bright Au patch at the pyramid apex observed using a Concentric Backscattered Detector. The size of the Au patch was confirmed to the same within experimental error before and after the polymer force measurements.

After the Au patch was successfully fabricated on the pyramid apex, a thiolated polymer (PEG-thiol) was covalently attached to it. Only one end of the polymer chain is thiolated. The thiol-SH head groups attach to the Au surface through the strong S-Au bond. The polymer chains were grafted to the surface only at one end [93, 94, 95]. The surface was cleaned off organics with 4 hours UV/Ozone cleaning prior to the polymer attachment [96, 97, 98]. PEG polymers of two different molecular weights of 20,000 Da and 40,000 Da were used. A 1 mM solution of the polymer PEG-thiol in ethanol was prepared. The solution was maintained at a temperature of 45°C. To attach the polymer to the Au patch, the cleaned cantilever tip with the Au patch was immersed into the PEG-thiol solution for 12 hours. After this the cantilever was rinsed in ethanol and DI water.

Following the attachment of the polymer, the cantilever was loaded into the AFM for the measurement of the entropic force. The force measurements were performed in a liquid environment using a fluid cell. The fluid cell was filled with 100 mM NaCl solution. The solution was degassed in vacuum to eliminate all entrapped air. The NaCl ions allows for the screening of electrostatic forces from any uncompensated charges on the plate or the Au patch. The Debye length, a measure of electrostatic screening length, is about 1nm for 100 mM NaCl solution. The electrostatic forces should be weak and negligible at distance much larger than Debye length.

The entropic forces were measured between the polymer coated pyramid apex and a flat surface. As the PEG polymer is hydrophilic [99], a hydrophobic planar surface was used as the second boundary. The use of the hydrophobic plate avoids the large attractive adhesive forces resulting from the use of hydrophilic surfaces [100]. Force measurements were performed using a Fluorinated Ethylene Propylene (FEP) film. The contact angle was measured to be 108°. As roughness would be an important parameter in the boundary dependence, the root mean square roughness of the FEP film surface was measured to be 1.2 nm with the AFM at the end of the experiment. To make the force measurement, the FEP film was mounted on the AFM sample stage on top of the piezo tube which allows control of the apex-FEP plate distance. The FEP plate was moved towards the cantilever tip using the piezo. The movement of the piezo in response to the applied voltage is calibrated using optical interferometry to be 8.57 nm/V [101]. The results of the force measurements made are discussed below.

5.3 Data analysis and comparison with two theoretical models

The entropic force from polymers confined between the apex of the conical pyramid and the hydrophobic flat plate was next measured. MW 20,000 Da PEG polymer was used in the first series of measurements. These polymers were attached to the Au patch at the apex of the pyramid as discussed above. The standard AFM force detection methodology was applied [102, 103, 104]. The reflected signal from the top of the cantilever was detected with a split photodiode. A force on the apex led to bending of the cantilever resulting in a deflection of the reflected light. To measure the entropic force as a function of apex-plate distance, the plate was moved continuously towards the apex using the piezo, and the cantilever deflection which corresponds to the force on the cantilever tip, was recorded every 0.7 nm moved by the plate. A typical cantilever deflection measured as a function of distance is shown in Fig. 5.3. This is usually referred to as the approach curve. As illustrated, at large separation distances between 30-50 nm, the cantilever deflection is below the resolution limit and can be set to zero. The oscillations are noise from scattered laser light entering the split photodiode. However, the scattered light from the approaching FEP plate causes a small nonzero slope as a function of distance. To correct for this, a straight line is fit to the deflection data between 30-50 nm and the corresponding scattered light signal is subtracted from the data. At distances below 30 nm the cantilever deflection due to the total force acting on the cantilever can be observed. The net force is the sum of the attractive van der Waals force and the repulsive entropic force. Note that the adhesion forces and potential electrostatic forces can be neglected due to use of the hydrophobic surface and the salt solution respectively. At very small tip-plate separation distances the van der Waals force overwhelms all others and the tip jumps into contact with the plate. The point of contact, which is the vertex in Fig. 5.3, is designated as zero separation distance. The contact point is determined to be precision of 0.2 nm better than the step size of 0.7 nm by linear extrapolation of the two neighboring points on the left and the right [103]. As the plate is a hard surface, any further upward movement of the plate after contact causes the cantilever tip to be pushed up by the plate leading to the linear signal seen in Fig. 5.3. The slope m of this linear signal can be used to find the deflection of the cantilever, as $\Delta Z = \Delta S \times m$, where ΔZ is the cantilever deflection in nm, ΔS is the change of deflection signal in volts. The cantilever deflection can be converted to a force F on the cantilever tip using Hookes law: $F = k \times \Delta Z$, where k is the cantilever spring constant. The spring constant of the cantilever $k = 42 \pm 1$ pN/nm was measured using its thermal spectrum [92]. The spring constant was confirmed to be the same before and after force measurements. The total measured force in Fig. 5.3 for the distance range from 50 nm to contact is negative implying a net attractive force. While the entropic force of the polymer is repulsive, the attractive van der Waals force between the Au patch on the apex and the plate has to be subtracted. Note that adhesive forces between polymers and the plate are eliminated through use of a hydrophobic plate and long range electrostatic forces through use of the 100 mM NaCl solution. At the molecular level there are no long range adhesive forces between the hydrophilic polymer and hydrophobic surface. Hydration and cavitation

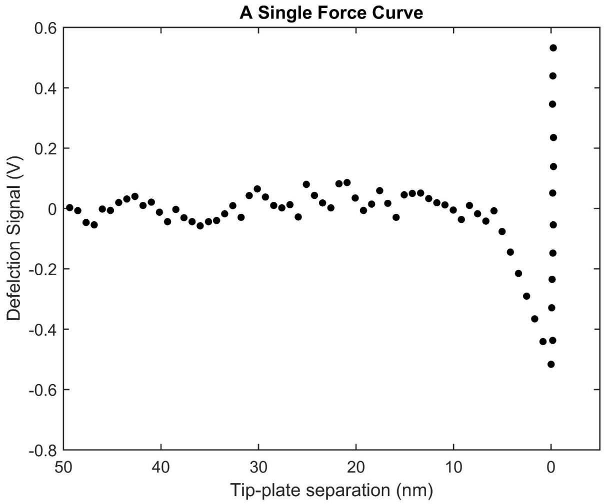

Figure 5.3: A typical cantilever deflection measured for the MW 20,000 Da polymers confined between the pyramidal apex and flat plate as a function of the tip-plate separation distance. The tip and plate come into contact at separation '0'.

forces act at distances of 1.5 nm and below, a distance range not considered in this work [105]. The average of 300 total force measurements from the confinement of the polymers between the pyramid apex and the FEP plate as a function of separation distance is shown in Fig. 5.4 as green dots. To understand the baseline van der Waals force from the bare Au patch, the same force measurements were done prior to attachment of the polymer. In this case the average measured force corresponds to the attractive van der Waals force between Au patch on the pyramid apex and the FEP plate, and is shown as red dots in Fig. 5.4. To obtain the repulsive entropic force from the confinement of the polymers in Fig. 5.4, the van der Waals force of the bare Au patch and FEP plate shown in red was subtracted from that of the total force with the polymer attached shown in green. The subtracted force is shown as black dots in Fig. 5.4. All error bars in Fig. 5.4 correspond to the standard errors for the 300 measurements. The entropic repulsion is observed to start at approximately

15 ± 3 nm separation and reach about 100 pN at a separation of 3 nm. The decrease in the repulsive force below 3 nm is possibly due to the roughness of the FEP surface. Valleys on the FEP surface confine polymer arms and reduce the repulsive entropic force. In addition, the van der Waals force between polymers and rough FEP plate below 3 nm may also lead to a decrease in the total force. These two effects cannot be subtracted or accounted for with the subtraction of the interaction of bare Au patch with the FEP plate. Thus, data points below 3 nm were not used in analysis.

Polymer-mediated entropic forces between scale-free objects have been studied in Ref. [65]. In the idealized model, polymers are attached to the apex of a cone, and fluctuate between the boundary of the cone and an infinite plate. The repulsive force due to loss of entropy as the cone tip with polymers approaches a plate is given by:

$$F = A\frac{k_B T}{h} \tag{5.1}$$

where h is the separation. The force amplitude A can be expressed as:

$$\frac{f(A)}{f} = \frac{7}{8} + [\frac{3}{\pi} - 0.80 - \frac{11}{12\pi}(f-1)]\,\Theta^{1/4} \tag{5.2}$$

where is cone angle, f is the number of arms. If only the first order approximation of Eq. 5.2 is considered, the amplitude $A(f)$ is the same as the number of arms f of the polymer. The Eq. 5.1 can be rewritten as:

$$F \approx f\frac{k_B T}{h} \tag{5.3}$$

The subtracted force curve shown in Fig. 5.4 was best fit with Eq. 5.3 for the distance range from 3-14 nm, keeping the Flory length $R_f = 14$ nm as the effective length of tethered polymers [106]. This theoretically estimated size of one polymer coil is given by the equation

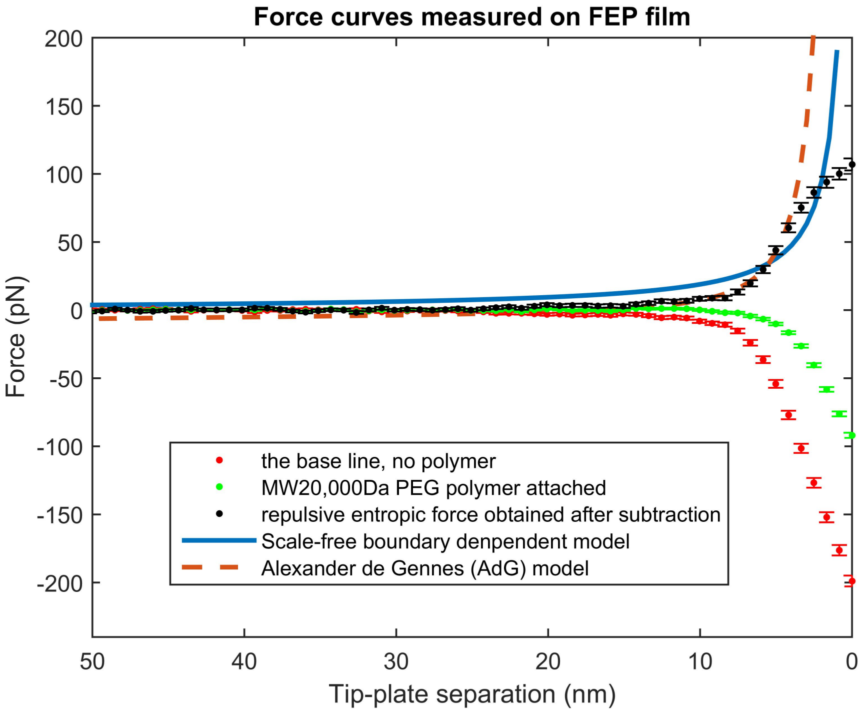

Figure 5.4: All force distance curves are an average of 300 force curves. The pyramid apex with bare Au patch-plate van der Waals force as a function of separation distance is shown by the red dots. The total interaction force (van der Waals+entropic force) with MW 20,000 Da polymer attached to the Au patch on the pyramid apex is shown as green dots. The force curve shown by black dots is the difference of the above two and corresponds to the net entropic force from the polymers as a function of tip-plate separation distance. Best fit lines are obtained for the scale-free model of polymer-mediated entropic forces between a cone tip and an infinite plate (cyan solid line) and the Alexander-de Gennes Theory (orange dashed line) for a brush polymer.

$R_f = a \times N^{0.6}$, where a is the monomer size and N is the degree of polymerization. The best fit ($R^2 = 0.83$) is shown as the cyan solid line in Fig. 5.4. The resulting parameter f was found to be 46. Within the approximation of this model, it implies that around 46 polymer chains are involved in the entropic confinement interaction between the pyramid apex and the FEP plate.

A comparison to the measurements of the Alexanderde Gennes (AdG) theory

[81, 82, 107, 108] for the entropic force for a polymer brush confined between two plates was also attempted. In the AdG model, the entropic pressure between a polymer covered plate and a bare plate can be described as:

$$P(h) = \frac{k_B T}{2s^3}\left[(\frac{L}{h})^{9/4} - (\frac{h}{L})^{3/4}\right] \approx \frac{50 k_B T}{s^3} exp(-\frac{2\pi h}{L}), \quad (0.2 < h/L < 0.9) \tag{5.4}$$

where h is the distance between two surfaces, L is the effective thickness of the polymer brush, and s is the spacing between two adjacent grafting sites and T is the absolute temperature. While this model is most appropriate for polymers between two plates, it might serve as a good approximation at very small separation distances between the Au patch and the FEP plate. As the same fluid cell cantilever holder was used for both apex abrasion (during the Au patch fabrication) as well as the force measurement, the tilt angle of the cantilever kept the same. The Au patch should be parallel to the plate surface. For comparison to the measured force the pressure in Eq. 5.4 is multiplied by the area of the Au patch $3.7 \times 10^4\ nm^2$. In Fig. 5.4, the best fit to the average measured repulsive force curve from 5-12 nm which matches the applicability region of the model $0.2 < h/L < 0.9$ is provided. The best fit ($R^2 = 0.97$) shown as the orange dashed line leads to an effective brush thickness L = 17 nm and polymer spacing s = 30 nm. As can be observed from Fig. 5.4, the effective thickness of 17 nm obtained from the best fit to the measured force is consistent with that estimated distance where the measured force exceeds zero value. The Flory radius of a PEG-thiol polymer chain with MW 20,000 Da is calculated as R_f = 14 nm, which is also consistent with the thickness L = 17 nm above from the fit to the AdG model. The conformation of tethered polymers on the surface depends on the distance between grafting sites. In the case of low grafting density, the polymer chains are disposed as mushrooms in a good solvent, where each polymer chain is isolated from neighbors and occupies a half sphere with radius consistent with the Flory length. Since the estimated spacing s is approximately twice the thickness L from the curve fit, one may conclude that the semi-spheres formed by polymer chains are adjacent to each other. Even though Eq. 5.4 tends to describe a polymer brush for high grafting density, the best fit curve still is a surprisingly good matches to our experimental data at very short separations. This might be because the conformation of polymers lie in a boundary regime between a brush and mushroom configuration. The AdG model is still applicable to our case. The effective area occupied by one single polymer is $s^2 = 900\ nm^2$. Thus, one can estimate the presence of 41 polymers on the apex for an Au patch of area $3.7 \times 10^4\ nm^2$. This number is of the same magnitude of 46 polymers obtained from the fit to the scale-free model.

To further understand the variation with polymer length, more experiments were performed using PEG with MW 40,000 Da. The primary motivation was to check if the entropic confinement force with longer polymers would approach the predictions of the scale-free model. The experiments were repeated with the same Au patch on the apex of the pyramidal AFM tip used in the experiments described above. To attach these longer polymers, the previously attached shorter polymers had to be removed while keeping the Au patch intact. The removal of the short polymers on the Au patch was accomplished using 4 hours of UV ozone cleaning. After this the cantilever was rinsed with alcohol followed by acetone and DI water. The complete removal of previous tethered polymers was confirmed by measuring force-distance curves. The longer MW 40,000 Da polymer was also attached using the thiol bonds on one end. The fluid cell was cleaned by rinsing with DI water, followed by acetone and finally ethanol and the cantilever with the longer polymers loaded. The entropic force measurements were repeated exactly the same as described earlier for the short MW 20,000 Da polymer shown as green dots in Fig. 5.5. The same subtraction of the van der Waals force from the bare Au patch was performed. The repulsive entropic force from the average of 300 measurements using the MW 40,000 Da polymer is shown as black dots in Fig. 5.5. Again, the error bars are the standard errors in the force measurements at each separation distance. Comparing the results between the short and the long polymers, the latter is found to lead to much larger forces. For example, in the case of the short polymer the measured forces at 10 nm and 5 nm were 8 ± 1 pN and 44 ± 3 pN, respectively. In contrast, the forces at the same separation distances for the long polymer were 9 ± 1 pN and 58 ± 3 pN, respectively, consistent with expectations of an increase in force corresponding to an increase in the number of monomers.

The measured forces with the long MW 40,000 Da polymer were compared to the scale-free model as well as the AdG theory. For comparison to the scale-free theory, a best fit ($R^2 = 0.76$) to the experimental data from 3 nm to 22 nm using equation (3) is shown as the cyan solid line in Fig. 5.5. The best fit value for f = 58 was found. This effectively means that 58 polymers were attached to the Au patch. The experimentally measured force values were also fit to the AdG theory ($R^2 = 0.97$) using Eq. 5.4 and are shown as the orange dashed line in Fig. 5.5. The best fit parameters lead to an effective brush thickness $L = 21$ nm and polymer spacing $s = 33$ nm. As can be observed from Fig. 5.5, the effective thickness obtained from the curve fit is again consistent with the estimated Flory length $R_f = 22$ nm for the MW 40,000 Da PEG polymer. The AdG theory is in

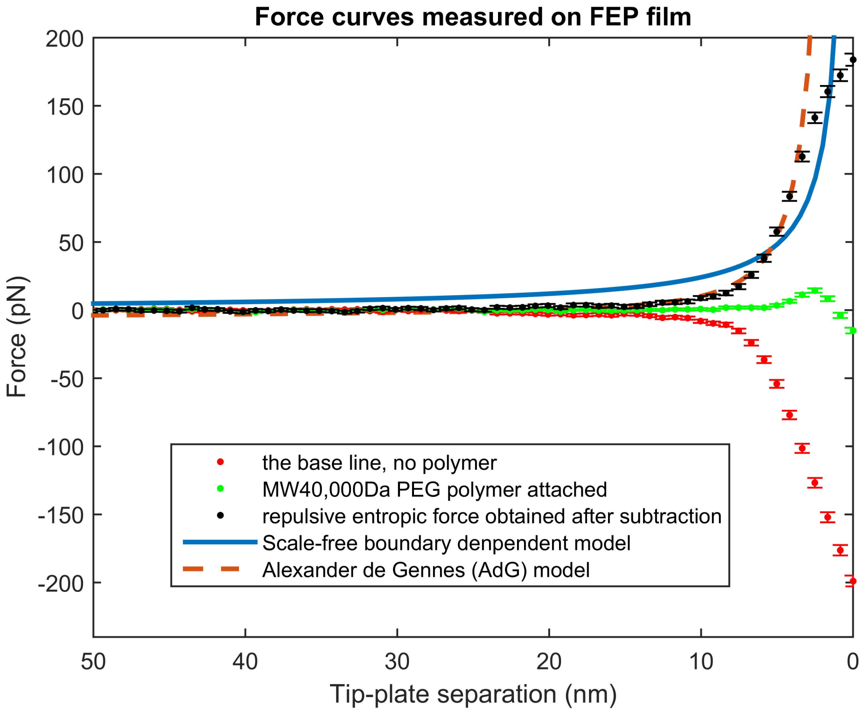

Figure 5.5: All force distance curves are an average of 300 force curves. The pyramid apex with bare Au patch-plate van der Waals force as a function of separation distance is shown by the red dots. The total interaction force (van der Waals+entropic force) with MW 40,000 Da polymer attached to the Au patch on the pyramid apex is shown as green dots. The force curve shown by black dots is the difference of the above two and corresponds to the net entropic force from the polymers as a function of tip-plate separation distance. Best fit lines are obtained for the scale-free model of polymer-mediated entropic forces between a cone tip and an infinite plate (cyan solid line) and the Alexanderde Gennes Theory (orange dashed line) for a brush polymer.

better agreement with the experimental data than that of the scale-free theory even for the longer polymer. Thus, for the size of the Au patch used on the apex of the pyramid and the tip-plate distances investigated, the polymer brush is still the better model for the entropic confinement forces measured. However, it should be noted that the AdG theory has 2 free parameters compared to the only one in the scale-free theory.

5.4 Summary for entropic force induced by polymers fluctuation

In conclusion, to demonstrate the boundary shape dependent entropic force from confined polymers, a reproducible method for attaching a few polymers to the apex of a pyramidal cone shaped AFM cantilever tip was developed. The entropic force between the tip and a flat hydrophobic plate of FEP was measured with an AFM using a fluid cell. The use of the hydrophobic plate eliminated adhesive forces between the hydrophilic polymers and the plate boundary. A salt solution was used to make the long range electrostatic forces negligible. Two sizes of PEG polymers MW 20,000 Da and MW 40,000 Da were used in the investigation. The polymer chains were covalently attached to the Au patch at the pyramid apex using thiol bonds at one end. The same Au patch was used with both the short and long polymers. The bare Au patch was used to measure the background van der Waals force between the patch and the FEP plate which was subtracted from the measured total force. The measured entropic confinement forces were compared to a recent scale-free theory for a few polymers attached to the apex of a cone and to the AdG theory for a polymer brush confined between flat plates. For the Au patch used and the separation distances measured, better agreement was found for the AdG theory of polymer brush. Future experiments with longer polymers which cause increased forces at larger distances will allow an improved study of the boundary shape dependencies of the confinement entropic force from polymers.

Chapter 6

Conclusions and future work

First, an upgraded custom built AFM based technique with higher sensitivity was developed to investigate puzzles in the quantum electrodynamic Casimir effect. Using combination of UV radiation and Ar ion beam bombardment, the residual potential difference V_0 between two Au surfaces were reduced to a near zero. It was also a distance independent value proving that the sphere and plate surfaces were equipotentials. The potentials also have a very low drift rate. This allow us to eliminate the rule of detrimental electrostatic patch effect in Casimir force measurements. In addition, the use of a much softer cantilever enhanced the sensitivity in the force gradient measurement and allowed a much larger measurement range up to 950 nm. Our experimental results agree with the predictions of Lifshitz theory when energy losses of free electrons in the metal are neglected within the measured range. On the contrary, the predictions using the same theory with inclusion of dissipation of free electrons are excluded at separation distance up to 820 nm at confidence level of 67%. The same conclusion given by the previous work only distinguished the two different models at the separation distance up to 420 nm using original dynamic AFM technique, and up to 750 nm using a micromachined oscillator. The reported experiment is currently the measurement to the largest separation distance.

To achieve higher precision to study Casimir force at even larger separation distance, a new technique has been designed and fabricated. The new idea requires measurement of the difference Casimir force between an Au surface and vacuum created by a deep trench. This design allows to explore Casimir force above 1 μm with much higher precision. The periodic structure of Au pads and trenches on the patterned disc is rotated below the Au sphere. The rotation will average out the effect of electric patches on Au surfaces. To achieve extreme stable rotation of the disc, an air bearing spindle is used. The cantilever manipulation system, vacuum system, optical system, electronics system and software have been built for the project. In an associated experiment we measured the piezoelectric coefficients of bio-samples using the optical system and demonstrated high displacement resolution. The future work will focus on this project and measure the Casimir force at larger separation distance.

To study the entropic Casimir force from thermal fluctuations of polymers between scale free boundaries, we attached polymers to a pyramidal AFM tip. The attached polymers were pushed against a hydrophobic surface of a FEP film. The repulsive force was measured as a function of separation distance using an AFM with a fluid cell. Two different sizes of polymer were used to explore the boundary dependence of the entropic force. The experimental results were compared to two different models. For the length of the polymers studied, better agreement with the brush model than the scale-free boundary dependent force model was found. In future experiments, longer polymers (MW $>$ 40,000 Da) will be used to study the boundary dependencies of the entropic Casimir force from the confined fluctuating polymers.

Bibliography

[1] H.B.G. Casimir. On the attraction between two perfectly conducting plates. *Proceedings Akadamie van Wetenschappen Amsterdam*, 51:793–795, 1948.

[2] V. M. Mostepanenko and N. N. Trunov. *The Casimir effect and its applications.* Oxford University Press, 1997.

[3] Kimball A Milton. *The Casimir effect: physical manifestations of zero-point energy.* World Scientific, 2001.

[4] Peter W Milonni. *The quantum vacuum: an introduction to quantum electrodynamics.* Academic press, 2013.

[5] M. Bordag, G. L. Klimchitskaya, U. Mohideen, and V. M. Mostepanenko. *Advances in the Casimir Effect.* International Series of Monographs on Physics. Oxford Univesity Press, Oxford, 2015.

[6] M. J. Sparnaay. Measurements of attractive forces between flat plates. *Physica*, 24(6):751–764, 1958.

[7] D. Tabor and R. H. S. Winterton. Surface forces: direct measurement of normal and retarded van der Waals forces. *Nature*, 219(5159):1120–1121, 1968.

[8] Peter H. G. M. van Blokland and J. Theodoor G. Overbeek. Van der Waals forces between objects covered with a chromium layer. *Journal of the Chemical Society, Faraday Transactions 1: Physical Chemistry in Condensed Phases*, 74(0):2637–2651, 1978.

[9] S. K. Lamoreaux. Demonstration of the Casimir force in the 0.6 to 6μm range. *Physical Review Letters*, 78(1):5–8, 1997.

[10] U. Mohideen and Anushree Roy. Precision measurement of the Casimir force from 0.1 to 0.9μm. *Physical Review Letters*, 81(21):4549–4552, 1998.

[11] G. Bressi, G. Carugno, R. Onofrio, and G. Ruoso. Measurement of the Casimir force between parallel metallic surfaces. *Physical Review Letters*, 88(4):041804, 2002.

[12] E. M. Lifshitz. The theory of molecular attractive forces between solids. *Soviet Physics JETP*, 2:73–83, 1956.

[13] V Adrian Parsegian. *Van der Waals forces: a handbook for biologists, chemists, engineers, and physicists*. Cambridge University Press, 2005.

[14] I. E. Dzyaloshinskii, E. M. Lifshitz, and L. P. Pitaevskii. The general theory of van der Waals forces. *Advances in Physics*, 10(38):165–209, 1961.

[15] R. Eisenschitz and F. London. ber das Verhltnis der van der Waalsschen Krfte zu den homopolaren Bindungskrften. *Zeitschrift fr Physik*, 60(7):491–527, 1930.

[16] F. London. Zur theorie und systematik der molekularkrfte. *Zeitschrift fr Physik*, 63(3):245–279, 1930.

[17] F. London. The general theory of molecular forces. *Transactions of the Faraday Society*, 33(0):8b–26, 1937.

[18] H. B. G. Casimir and D. Polder. Influence of retardation on the London-van der Waals forces. *Nature*, 158(4022):787–788, 1946.

[19] H. B. G. Casimir and D. Polder. The influence of retardation on the London-van der Waals forces. *Physical Review*, 73(4):360–372, 1948.

[20] M. Bordag, U. Mohideen, and V. M. Mostepanenko. New developments in the Casimir effect. *Physics Reports*, 353(1):1–205, 2001.

[21] G. L. Klimchitskaya, U. Mohideen, and V. M. Mostepanenko. The Casimir force between real materials: Experiment and theory. *Reviews of Modern Physics*, 81(4):1827–1885, 2009.

[22] L. M. Woods, D. A. R. Dalvit, A. Tkatchenko, P. Rodriguez-Lopez, A. W. Rodriguez, and R. Podgornik. Materials perspective on Casimir and van der Waals interactions. *Reviews of Modern Physics*, 88(4):48, 2016.

[23] C.-C. Chang, A. A. Banishev, R. Castillo-Garza, G. L. Klimchitskaya, V. M. Mostepanenko, , and U. Mohideen. Gradient of the Casimir force between au surfaces of a sphere and a plate measured using an atomic force microscope in a frequency-shift technique. *Physical Review B*, 85(16):165443, 2012.

[24] E. D. Palik, O. J. Glembocki, I. Heard, P. S. Burno, and L. Tenerz. Etching roughness for (100) silicon surfaces in aqueous KOH. *Journal of Applied Physics*, 70(6):3291–3300, 1991.

[25] E.-L. Florin, M. Rief, H. Lehmann, M. Ludwig, C. Dornmair, V. T. Moy, and H. E. Gaub. Sensing specific molecular interactions with the atomic force microscope. *Biosensors and Bioelectronics*, 10:6, 1995.

[26] Jun Xu, G. L. Klimchitskaya, V. M. Mostepanenko, and U. Mohideen. Reducing detrimental electrostatic effects in Casimir-force measurements and Casimir-force-based microdevices. *Physical Review A*, 97(3):7, 2018.

[27] John R. Vig. UV/ozone cleaning of surfaces. *Journal of Vacuum Science & Technology A*, 3:8, 1985.

[28] N. S. McIntyre, R. D. Davidson, T. L. Walzak, R. Williston, M. Westcott, and A. Pekarsky. Uses of ultraviolet/ozone for hydrocarbon removal: Applications to surfaces of complex composition or geometry. *Journal of Vacuum Science & Technology A*, 9:5, 1991.

[29] S. R. Koebley, R. A. Outlaw, and R. R. Dellwo. Degassing a vacuum system with in-situ UV radiation. *Journal of vacuum Science & Technology A*, 30:3, 2012.

[30] R. R. Sowell, R. E. Cuthrell, D. M. Mattox, and R. D. Bland. Surface cleaning by ultraviolet radiation. *Journal of Vacuum Science & Technology*, 11:2, 1974.

[31] A. Krozer and M. Rodahl. X-ray photoemission spectroscopy study of UV/ozone oxidation of Au under ultra high vacuum conditions. *Journal of Vacuum Science & Technology A*, 15:6, 1997.

[32] D. E. King. Oxidation of gold by ultraviolet light and ozone at 25 °C. *Journal of Vacuum Science & Technology A*, 13:7, 1995.

[33] G. Bimonte. Going beyond PFA: A precise formula for the sphere-plate Casimir force. *Europhysics Letters*, 118(2), 2017.

[34] M. Hartmann, G. L. Ingold, and P. A. M. Neto. Plasma versus Drude modeling of the Casimir force: Beyond the proximity force approximation. *Physical Review Letters*, 119(4):6, 2017.

[35] G. Bimonte, D. Lopez, and R. S. Decca. Isoelectronic determination of the thermal Casimir force. *Physical Review B*, 93(18):15, 2016.

[36] R. S. Decca, D. Lopez, E. Fischbach, G. L. Klimchitskaya, D. E. Krause, and V. M. Mostepanenko. Tests of new physics from precise measurements of the Casimir pressure between two gold-coated plates. *Physical Review D*, 75(7):4, 2007.

[37] R. S. Decca, D. Lopez, E. Fischbach, G. L. Klimchitskaya, D. E. Krause, and V. M. Mostepanenko. Novel constraints on light elementary particles and extra-dimensional physics from the Casimir effect. *European Physical Journal C*, 51(4):963–975, 2007.

[38] W. Broer, G. Palasantzas, J. Knoester, and V. B. Svetovoy. Roughness correction to the Casimir force at short separations: Contact distance and extreme value statistics. *Physical Review B*, 85(15):13, 2012.

[39] A. O. Sushkov, W. J. Kim, D. A. R. Dalvit, and S. K. Lamoreaux. Observation of the thermal Casimir force. *Nature Physics*, 7:230, 2011.

[40] Parameswaran Hariharan. *Basics of interferometry*. Elsevier, 2010.

[41] D. Rugar, H. J. Mamin, and P. Guethner. Improved fiber-optic interferometer for atomic force microscopy. *Applied Physics Letters*, 55(25):2588–2590, 1989.

[42] B. K. Nowakowski, D. T. Smith, and S. T. Smith. Highly compact fiber fabry-perot interferometer: A new instrument design. *Review of Scientific Instruments*, 87(11):115102, 2016.

[43] D. T. Smith, J. R. Pratt, and L. P. Howard. A fiber-optic interferometer with sub-picometer resolution for dc and low-frequency displacement measurement. *Review of Scientific Instruments*, 80(3):035105, 2009.

[44] Shuming Yang and Zhang Guofeng. A review of interferometry for geometric measurement. *Measurement Science and Technology*, 29(10):102001, 2018.

[45] Klaus Thurner, Pierre-Franois Braun, and Khaled Karrai. Absolute distance sensing by two laser optical interferometry. *Review of Scientific Instruments*, 84(11):115002, 2013.

[46] A. A. Arends, T. M. Germain, J. F. Owens, and S. A. Putnam. Simultaneous reflectometry and interferometry for measuring thin-film thickness and curvature. *Review of Scientific Instruments*, 89(5):055117, 2018.

[47] Bruno Zappone, Weichao Zheng, and Susan Perkin. Multiple-beam optical interferometry of anisotropic soft materials nanoconfined with the surface force apparatus. *Review of Scientific Instruments*, 89(8):085112, 2018.

[48] S. Petuchowski, T. Giallorenzi, and S. Sheem. A sensitive fiber-optic fabry-perot interferometer. *IEEE Journal of Quantum Electronics*, 17(11):2168–2170, 1981.

[49] T. Yoshino, K. Kurosawa, K. Itoh, and T. Ose. Fiber-optic fabry-perot interferometer and its sensor applications. *IEEE Transactions on Microwave Theory and Techniques*, 30(10):1612–1621, 1982.

[50] D. Hunger, T Steinmetz, Y Colombe, C Deutsch, T W Hnsch, and J Reichel. A fiber fabryperot cavity with high finesse. *New Journal of Physics*, 12(6):065038, 2010.

[51] C. Rembe, L. Kadner, and M. Giesen. Approaching attometer laser vibrometry. *Review of Scientific Instruments*, 87(10):102503, 2016.

[52] Christian Rembe. There is plenty of room at the bottom to approach sub-femtometer vibrometry. *AIP Conference Proceedings*, 1457(1):78–87, 2012.

[53] J. R. Fernandes, F. A. de S, J. L. Santos, and E. Joanni. Optical fiber interferometer for measuring the d33 coefficient of piezoelectric thin films with compensation of substrate bending. *Review of Scientific Instruments*, 73(5):2073–2078, 2002.

[54] Q. M. Zhang, W. Y. Pan, and L. E. Cross. Laser interferometer for the study of piezoelectric and electrostrictive strains. *Journal of Applied Physics*, 63(8):2492–2496, 1988.

[55] M. Ohki and T. Shiosaki. Measurement and evaluation of piezoelectric vibration using fiber optic interferometer. In *IEEE 1991 Ultrasonics Symposium,*, pages 615–620 vol.1, Dec 1991.

[56] James C. Weaver, Garrett W. Milliron, Ali Miserez, Kenneth Evans-Lutterodt, Steven Herrera, Isaias Gallana, William J. Mershon, Brook Swanson, Pablo Zavattieri, Elaine DiMasi, and David Kisailus. The stomatopod dactyl club: A formidable damage-tolerant biological hammer. *Science*, 336(6086):1275, 2012.

[57] Nicholas A. Yaraghi, Lessa Grunenfelder, Nobphadon Suksangpanya, Nicolas Guarin, Steven Herrera, Garrett Milliron, Pablo Zavattieri, Leigh Sheppard, Richard Wuhrer, and David Kisailus. Elemental and phase analysis of the stomatopod dactyl club by x-ray mapping. *Microscopy and Microanalysis*, 21(S3):2007–2008, 2015.

[58] Nicholas A. Yaraghi, Nicols Guarn-Zapata, Lessa K. Grunenfelder, Eric Hintsala, Sanjit Bhowmick, Jon M. Hiller, Mark Betts, Edward L. Principe, Jae-Young Jung, Leigh Sheppard, Richard Wuhrer, Joanna McKittrick, Pablo D. Zavattieri, and David Kisailus. Biocomposites: A sinusoidally architected helicoidal biocomposite. *Advanced Materials*, 28(32):6769–6769, 2016.

[59] Y. Sun, W. W. Cao, and L. E. Cross. Electrostriction effect in glass. *Materials Letters*, 4(8):329–336, 1986.

[60] Michael Levin, Alexander P. McCauley, Alejandro W. Rodriguez, M. T. Homer Reid, and Steven G. Johnson. Casimir repulsion between metallic objects in vacuum. *Physical Review Letters*, 105(9):090403, 2010.

[61] F. Schlesener, A. Hanke, and S. Dietrich. Critical Casimir forces in colloidal suspensions. *Journal of Statistical Physics*, 110(3):981–1013, 2003.

[62] R. Garcia and M. H. W. Chan. Critical fluctuation-induced thinning of ^{4}He films near the superfluid transition. *Physical Review Letters*, 83(6):1187–1190, 1999.

[63] R. Golestanian, M. Goulian, and M. Kardar. Fluctuation-induced interactions between rods on membranes and interfaces. *Europhysics Letters (EPL)*, 33(3):241–246, 1996.

[64] Mohammad F. Maghrebi, Yacov Kantor, and Mehran Kardar. Polymer-mediated entropic forces between scale-free objects. *Physical Review E*, 86(6):061801, 2012.

[65] Mohammad F. Maghrebi, Yacov Kantor, and Mehran Kardar. Entropic force of polymers on a cone tip. *EPL (Europhysics Letters)*, 96(6):66002, 2011.

[66] Roy Bubis, Yacov Kantor, and Mehran Kardar. Configurations of polymers attached to probes. *EPL (Europhysics Letters)*, 88(4):48001, 2009.

[67] J. Ennis, E. M. Sevick, and D. R. M. Williams. Compression of a polymer chain by a small obstacle: The effect of fluctuations on the escape transition. *Physical Review E*, 60(6):6906–6918, 1999.

[68] M. C. Guffond, D. R. M. Williams, and E. M. Sevick. End-tethered polymer chains under AFM tips: Compression and escape in theta solvents. *Langmuir*, 13(21):5691–5696, 1997.

[69] A. Milchev, V. Yamakov, and K. Binder. Escape transition of a compressed polymer mushroom under good solvent conditions. *EPL (Europhysics Letters)*, 47(6):675, 1999.

[70] G. Subramanian, D. R. M. Williams, and P. A. Pincus. Escape transitions and force laws for compressed polymer mushrooms. *EPL (Europhysics Letters)*, 29(4):285, 1995.

[71] Jorge Jimenez and Raj Rajagopalan. Interaction between a grafted polymer chain and an AFM tip: Scaling laws, forces, and evidence of conformational transition. *Langmuir*, 14(10):2598–2601, 1998.

[72] Ronald Dickman and Pearl E. Anderson. Force between grafted polymer brushes. *The Journal of Chemical Physics*, 99(4):3112–3118, 1993.

[73] Hillary J. Taunton, Chris Toprakcioglu, Lewis J. Fetters, and Jacob Klein. Forces between surfaces bearing terminally anchored polymer chains in good solvents. *Nature*, 332(6166):712–714, 1988.

[74] Georges Hadziioannou, Sanjay Patel, Steve Granick, and Matthew Tirrell. Forces between surfaces of block copolymers adsorbed on mica. *Journal of the American Chemical Society*, 108(11):2869–2876, 1986.

[75] Hillary J. Taunton, Chris Toprakcioglu, Lewis J. Fetters, and Jacob Klein. Interactions between surfaces bearing end-adsorbed chains in a good solvent. *Macromolecules*, 23(2):571–580, 1990.

[76] K. Binder and A. Milchev. Polymer brushes on flat and curved surfaces: How computer simulations can help to test theories and to interpret experiments. *Journal of Polymer Science Part B: Polymer Physics*, 50(22):1515–1555, 2012.

[77] Michael Murat and Gary S. Grest. Molecular dynamics simulations of the force between a polymer brush and an AFM tip. *Macromolecules*, 29(25):8282–8284, 1996.

[78] Igal Szleifer. Statistical thermodynamics of polymers near surfaces. *Current Opinion in Colloid & Interface Science*, 1(3):416–423, 1996.

[79] Ali Dhinojwala and Steve Granick. Surface forces in the tapping mode: solvent permeability and hydrodynamic thickness of adsorbed polymer brushes. *Macromolecules*, 30(4):1079–1085, 1997.

[80] Jacob N. Israelachvili and Haakan Wennerstroem. Entropic forces between amphiphilic surfaces in liquids. *The Journal of Physical Chemistry*, 96(2):520–531, 1992.

[81] Pierre-Gilles de Gennes. *Scaling concepts in polymer physics*. Cornell university press, 1979.

[82] P. G. de Gennes. Polymers at an interface; a simplified view. *Advances in Colloid and Interface Science*, 27(3):189–209, 1987.

[83] S. T. Milner, T. A. Witten, and M. E. Cates. Theory of the grafted polymer brush. *Macromolecules*, 21(8):2610–2619, 1988.

[84] P. G. de Gennes. Conformations of polymers attached to an interface. *Macromolecules*, 13(5):1069–1075, 1980.

[85] Sonia Jorge and Antonio Rey. Conformational properties of flexible polymer chains in highly confined environments. *The Journal of Chemical Physics*, 106(13):5720–5730, 1997.

[86] Tommie W. Kelley, Phillip A. Schorr, Kristin D. Johnson, Matthew Tirrell, and C. Daniel Frisbie. Direct force measurements at polymer brush surfaces by atomic force microscopy. *Macromolecules*, 31(13):4297–4300, 1998.

[87] Dzina Kleshchanok, Remco Tuinier, and Peter R. Lang. Direct measurements of polymer-induced forces. *Journal of Physics: Condensed Matter*, 20(7):073101, 2008.

[88] Hans-Jrgen Butt, Brunero Cappella, and Michael Kappl. Force measurements with the atomic force microscope: Technique, interpretation and applications. *Surface Science Reports*, 59(1):1–152, 2005.

[89] Xiao Yang, Harry A. Scott, Finny Monickaraj, Jun Xu, Soroush Ardekani, Carolina F. Nitta, Andrea Cabrera, Paul G. McGuire, Umar Mohideen, Arup Das, and Kaustabh Ghosh. Basement membrane stiffening promotes retinal endothelial activation associated with diabetes. *The FASEB Journal*, 30(2):601–611, 2015.

[90] Andrea P. Cabrera, Arun Bhaskaran, Jun Xu, Xiao Yang, Harry A. Scott, Umar Mohideen, and Kaustabh Ghosh. Senescence increases choroidal endothelial stiffness and susceptibility to complement injury: Implications for choriocapillaris loss in AMD. *Investigative Ophthalmology & Visual Science*, 57(14):5910–5918, 2016.

[91] Ijeoma M. Nnebe and James W. Schneider. A tapping-mode AFM study of the compression of grafted poly(ethylene glycol) chains. *Macromolecules*, 39(10):3616–3621, 2006.

[92] E. L. Florin, M. Rief, H. Lehmann, M. Ludwig, C. Dornmair, V. T. Moy, and H. E. Gaub. Sensing specific molecular interactions with the atomic force microscope. *Biosensors and Bioelectronics*, 10(9):895–901, 1995.

[93] J. Christopher Love, Lara A. Estroff, Jennah K. Kriebel, Ralph G. Nuzzo, and George M. Whitesides. Self-assembled monolayers of thiolates on metals as a form of nanotechnology. *Chemical Reviews*, 105(4):1103–1170, 2005.

[94] Q. Jin, J. A. Rodriguez, C. Z. Li, Y. Darici, and N. J. Tao. Self-assembly of aromatic thiols on Au(111). *Surface Science*, 425(1):101–111, 1999.

[95] Henrik Grnbeck, Alessandro Curioni, and Wanda Andreoni. Thiols and disulfides on the Au(111) surface: The head group-gold interaction. *Journal of the American Chemical Society*, 122(16):3839–3842, 2000.

[96] Lee M. Fischer, Maria Tenje, Arto R. Heiskanen, Noriyuki Masuda, Jaime Castillo, Anders Bentien, Jenny mneus, Mogens H. Jakobsen, and Anja Boisen. Gold cleaning methods for electrochemical detection applications. *Microelectronic Engineering*, 86(4):1282–1285, 2009.

[97] Takao Ishida, Satoshi Tsuneda, Naoki Nishida, Masahiko Hara, Hiroyuki Sasabe, and Wolfgang Knoll. Surface-conditioning effect of gold substrates on octadecanethiol self-assembled monolayer growth. *Langmuir*, 13(17):4638–4643, 1997.

[98] Tennyson Smith. The hydrophilic nature of a clean gold surface. *Journal of Colloid and Interface Science*, 75(1):51–55, 1980.

[99] Redouan Mahou and Christine Wandrey. Versatile route to synthesize heterobifunctional poly(ethylene glycol) of variable functionality for subsequent pegylation. *Polymers*, 4(1), 2012.

[100] Ali Faghihnejad and Hongbo Zeng. Interaction mechanism between hydrophobic and hydrophilic surfaces: Using polystyrene and mica as a model system. *Langmuir*, 29(40):12443–12451, 2013.

[101] F. Chen and U. Mohideen. Fiber optic interferometry for precision measurement of the voltage and frequency dependence of the displacement of piezoelectric tubes. *Review of Scientific Instruments*, 72(7):3100–3102, 2001.

[102] Ricardo Garca and Rubn Prez. Dynamic atomic force microscopy methods. *Surface Science Reports*, 47(6):197–301, 2002.

[103] Hsiang-Chih Chiu, Chia-Cheng Chang, R. Castillo-Garza, F. Chen, and U. Mohideen. Experimental procedures for precision measurements of the Casimir force with an atomic force microscope. *Journal of Physics A: Mathematical and Theoretical*, 41(16):164022, 2008.

[104] Brunero Cappella and Brunero Cappella. *Physical principles of force-distance curves by atomic force microscopy*, pages 3–66. Springer International Publishing, Cham, 2016.

[105] Matej Kandu and Roland R. Netz. From hydration repulsion to dry adhesion between asymmetric hydrophilic and hydrophobic surfaces. *Proceedings of the National Academy of Sciences*, 112(40):12338, 2015.

[106] Kenneth A. Rubinson and Susan Krueger. Poly(ethylene glycol)s 2000-8000 in water may be planar: A small-angle neutron scattering (SANS) structure study. *Polymer*, 50(20):4852–4858, 2009.

[107] Agns Anne, Christophe Demaille, and Jacques Moiroux. Terminal attachment of Polyethylene Glycol (PEG) chains to a gold electrode surface. cyclic voltammetry applied to the quantitative characterization of the flexibility of the attached peg chains and of their penetration by mobile PEG chains. *Macromolecules*, 35(14):5578–5586, 2002.

[108] Michael L. Alessi, Alexander I. Norman, Sasha E. Knowlton, Derek L. Ho, and Sandra C. Greer. Helical and coil conformations of poly(ethylene glycol) in isobutyric acid and water. *Macromolecules*, 38(22):9333–9340, 2005.

[109] Natalija Backmann, Natascha Kappeler, Thomas Braun, Franois Huber, Hans-Peter Lang, Christoph Gerber, and Roderick Y. H. Lim. Sensing surface PEGylation with microcantilevers. *Beilstein Journal of Nanotechnology*, 1:3–13, 2010.

[110] Roderick Y. H. Lim, Ning-Ping Huang, Joachim Kser, Jie Deng, K. H. Aaron Lau, Kyrill Schwarz-Herion, Birthe Fahrenkrog, and Ueli Aebi. Flexible phenylalanine-glycine nucleoporins as entropic barriers to nucleocytoplasmic transport. *Proceedings of the National Academy of Sciences*, 103(25):9512, 2006.